To the graduate council:

I am submitting herewith a dissertation written by Robert Stephen Mahurin entitled "Parity violation in polarized cold neutron capture." I have examined the final electronic copy of this dissertation for form and content and recommend that it be accepted in partial fulfillment of the requirements for the degree of Doctor of Philosophy, with a major in Physics.

Geoffrey L. Greene, Major Professor

We have read this dissertation and
recommend its acceptance:

Robert N. Compton

Yuri Kamyshkov

Witold Nazarewicz

Acceptance for the Council:

Carolyn R. Hodges
Vice Provost and Dean of the Graduate School

Original signatures are on file with official student records.

Parity violation in polarized cold neutron capture

A dissertation presented for
the Doctor of Philosophy degree
University of Tennessee, Knoxville

Robert Stephen Mahurin
May 2009

Copyright ©2009 by Rob Mahurin.
All rights reserved.

for Ellen

Acknowledgements

I am deeply grateful to my advisor, Geoff Greene, for his support during my time as a graduate student. It has been a privilege and a pleasure to have so much knowledge, insight, style, and wit from a colleague and friend. Without his patient encouragement this effort would have long ago been abandoned.

The NPDGamma collaboration holds the distinction of being the largest organization I have belonged to that does not include any jerks. I am especially grateful for many pleasantly educational hours spent with Seppo Penttilä, David Bowman, Scott Wilburn, Mike Snow, Greg Mitchell, and Michael Gericke; with Gil Peralta; with Mischa Dabagian, Chad Gillis, Chris Crawford, Libertad Barron, and Monisha Sharma; and with Jonny Dadras.

My many trips between Knoxville and Los Alamos were made much pleasanter by the easy competence of the UT Physics Department staff, especially Judy Hutchins. I owe a great debt to my late friend Viola McTeigue, who rented me not only a room, but a family.

Finally I thank my family: my parents, who have provided constant support and encouragement; my wife Ellen, who tolerates my long absences while I am elsewhere doing physics, even across the dinner table; and my children Hannah and Will, who tolerate no such nonsense.

Abstract

The longitudinal asymmetry in photons emitted during radiative neutron-proton capture depends cleanly on the neutral current contribution to the weak nucleon-nucleon interaction. The NPDGamma experiment is an effort to measure this asymmetry with precision ten parts per billion, which is 10% of its range of predicted values. In 2006 the NPDGamma collaboration acquired its first production dataset at the Los Alamos Neutron Science Center. A pulsed beam of polarized slow neutrons is incident on a 16 L parahydrogen target; capture photons are observed in current mode in a cylindrical array of CsI scintillators. In this initial experiment, roughly 730 hours running with 50–55% neutron polarization, we set a new upper limit of 210 parts per billion for the size of the NPDGamma asymmetry, a modest improvement over the existing limit. In the next stage of the experiment this limit will be greatly reduced with the increased neutron flux at the Spallation Neutron Source.

Contents

Acknowledgements **iv**

Abstract **v**

Contents **vi**

List of Figures **viii**

Introduction **1**

1 The hadronic weak interaction **4**
1.1 The meson-exchange framework 7
1.2 Charged and neutral currents in the two-nucleon system 8
1.3 The modern experimental situation 10
1.4 Modern theoretical approaches 12

2 The $\vec{n} + p \rightarrow d + \gamma$ experiment **14**
2.1 Neutron production on FP12 at LANSCE 15
2.1.1 Beam transport 15
2.1.2 Shielding and collimation 19
2.1.3 Neutron beam monitors 19
2.2 Neutron spin transport 20
2.2.1 Magnetic field 20
2.2.2 Polarized ^{3}He spin filter 20
2.2.3 Radiofrequency spin flipper 21
2.3 Liquid parahydrogen target 22
2.3.1 The liquid hydrogen cryogenic systems 24
2.3.2 Operation 27
2.4 Current-mode CsI detectors 30
2.5 Systematic effects 30
2.5.1 False asymmetries 30
2.5.2 Backgrounds and background asymmetries 33

3 Analysis methods **35**
3.1 Components of the data stream 35
3.2 Computation of raw asymmetries 38
3.2.1 Systematic effects with negligible pedestals 38
3.2.2 Pedestal dilution 40
3.2.3 Relations among the different asymmetries 41
3.2.4 Signal reconstruction and integer arithmetic 43
3.3 Consistency checking 44
3.3.1 Truncation errors are negligible 44
3.3.2 Computed asymmetries are normally distributed 44
3.4 Weighting and averaging 49
3.4.1 Polarization and geometry weighting 49
3.4.2 Error weighting and counting statistics 50

4 $\vec{n} + p \rightarrow d + \gamma$ at the Spallation Neutron Source **52**
4.1 An analytic chopper 54
4.1.1 Frame overlap for various chopper pairs 57
4.1.2 Frame overlap for various opening angles 59
4.2 McStas simulation 61
4.2.1 Choppers 63
4.2.2 ^{3}He spin filter 67
4.2.3 Spin flipper cavity 67
4.2.4 Liquid hydrogen target 68
4.3 Chopper and spin flipper optimization 68
4.3.1 Statistics of the asymmetry 68
4.3.2 Optimization procedure and results 69
4.4 Recommendations 72

Conclusion **75**

Bibliography **76**

Vita **84**

List of Figures

1 The $\vec{\mathrm{n}} + \mathrm{p} \to \mathrm{d} + \gamma$ apparatus at LANSCE 2

1.1 Transitions in n-p capture 9

2.1 Spectrum at the end of FP12. 16
2.2 Two-pinhole system for viewing the moderator. 18
2.3 Cross sections for neutrons on liquid hydrogen at 19 K. 23
2.4 The $\vec{\mathrm{n}} + \mathrm{p} \to \mathrm{d} + \gamma$ hydrogen target system. 26
2.5 Refrigerators and temperature sensors in the LH_2 cryostat 27
2.6 Temperatures and pressures in the target during August 2006 fill 28
2.7 Oscillations in the hydrogen target 29
2.8 Cooler oscillations 29
2.9 Stable target operation 29
2.10 Mott-Schwinger scattering 32

3.1 The $\vec{\mathrm{n}} + \mathrm{p} \to \mathrm{d} + \gamma$ data acquisition system 36
3.2 Sum and difference amplifiers 36
3.3 Data summary from run 52 900 45
3.4 Arithmetic asymmetries for run 52 900 46
3.5 Asymmetry histogram for one pair, one time bin 46
3.6 Histograms of roundoff errors in run 52 900 47
3.7 Insensitivity of fits to histogram binning 48
3.8 Geometry factors 50

4.1 Chopper edge position and exposed fraction of a guide 55
4.2 A chopper at a distance x from the moderator 56
4.3 Neutron transmission by the guide and its choppers 58
4.4 Chopper phasing permitting clean spectrum measurement 59
4.5 Chopper phasing permitting beam-on pedestal data 59
4.6 Number of spin flips for wraparound neutrons. 60
4.7 Correlation between position and slope in the horizontal (x) direction of neutrons at the source exit window. 63
4.8 Distribution of $d = vt$ at the moderator exit window 64
4.9 SNS neutron spectrum as transmitted by guide, choppers, ^{3}He . . 65
4.10 Correlations between co- and counter-rotating choppers 66

4.11 Histograms of the figure of merit 70
4.12 Chopped neutron spectrum and polarization, vs. wavelength . . 71
4.13 Chopped neutron spectrum, wrapped to time of observation . . . 71

Introduction

The neutron participates in all four of the gravitational, electromagnetic, weak, and strong interactions. As a result, experiments with neutrons offer unique opportunities to precisely measure the fundamental structure of our world [Nico and Snow, 2005]. For example, while weak interactions among leptons have been characterized extremely well [as summarized e.g. by the PDG], the hadronic weak interaction is complicated by two levels of many-body interaction. Internally, hadrons are composite objects where quantum chromodynamics and electromagnetism contribute far more to the dynamics than does the weak interaction. Externally, hadrons are mostly bound up in nuclei, which exhibit the same complications on a different scale. As a long-lived, electrically neutral hadron available in large quantities, the neutron is an obvious candidate for experiments where a small violation of parity or some other symmetry provides evidence of the weak interaction above a background of longer-range forces.

In large systems, nuclear structure effects can conspire to produce asymmetries as large as 10% in some electronic transitions [Yuan et al., 1991]. However, such massively collective behavior is not easily interpretable in terms of a microscopic interaction. Efforts to determine the hadronic weak couplings from large systems for which microscopic interpretations have been found [Bini et al., 1988; Wood et al., 1997] have produced inconsistent results. This failure has motivated a program of weak interaction experiments in few-nucleon systems: p-p, p-α, n-p, n-α. For such small systems the parity-violating observables can be reliably calculated in terms of low-energy hadronic weak couplings, which are in turn accessible from lattice QCD or effective field theory [Desplanques, 2005, and references therein]. However, the lack of many-body enhancement means the parity-violating asymmetries have the "natural" scale $\sim 10^{-7}$, making the measurements quite challenging.

The $\vec{\mathrm{n}} + \mathrm{p} \to \mathrm{d} + \gamma$ experiment aims to measure the correlation A_γ between neutron spin and photon direction in the capture of polarized cold neutrons on parahydrogen. Figure 1 shows the configuration of the experiment as it took data through 2006 at the Los Alamos Neutron Science Center (LANSCE). Neutrons are produced in short pulses at 20 Hz when a 100 µA beam of 800 MeV protons strikes a tungsten spallation target. The neutrons scatter from a partially coupled cold hydrogen moderator and travel 20 m down a straight, $m = 3.5$ supermirror guide with area $9.5 \times 9.5\,\mathrm{cm}^2$. Part of the guide may be replaced by a steel shutter, permitting access to the downstream part of the experiment

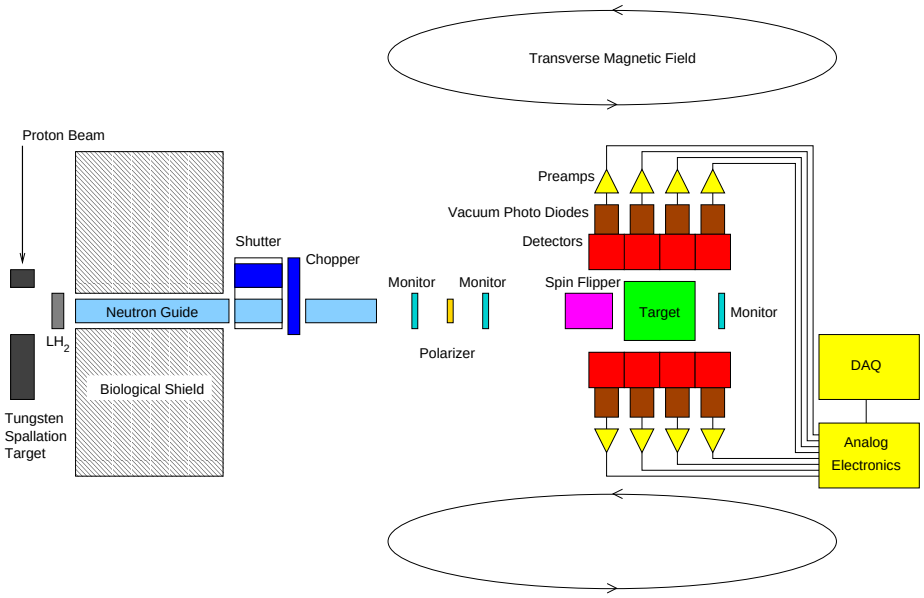


Figure 1: The $\vec{\mathrm{n}} + \mathrm{p} \rightarrow \mathrm{d} + \gamma$ apparatus at LANSCE.

even with the proton beam on. A chopper stops slow neutrons that would otherwise reach the experiment during a subsequent pulse, providing a unique relationship between time of flight and neutron energy. At the end of the guide, a thin ^{3}He ion chamber measures the neutron flux as a function of time of flight. Following the ion chamber, the neutrons then pass through a large area (10 cm diameter) nuclear spin polarized ^{3}He cell, which polarizes the neutrons; a second thin ion chamber; and a radio-frequency spin flipper, which reverses the spin of the neutrons every other pulse in the pattern $\uparrow\downarrow\downarrow\uparrow\downarrow\uparrow\uparrow\downarrow$. Immediately downstream of the spin flipper is a 16 L volume of liquid hydrogen at 17 K, containing $< 0.03\%$ orthohydrogen. Roughly 60% of the beam captures in the hydrogen, each capture emitting a single 2.2 MeV γ ray. Neutrons which neither capture nor scatter in the target stop in a final, thicker, ion chamber, or in a ^{6}Li beam stop. Enclosing the target are four rings of twelve $15 \times 15 \times 15\,\mathrm{cm}^3$ CsI scintillators, which convert 95% of the γ energy (within a solid angle of $\sim 3\pi$) into visible light. Vacuum photodiodes convert the scintillation light to a photocurrent. To enable subtraction of similar signals at high precision over a large dynamic range, the photocurrents for each ring are converted to a sum and twelve difference signals prior to being digitized. From the end of the neutron guide to the final detector, the experiment is in a uniform 10 G magnetic field.

The parity-violating asymmetry in the photocurrents from a single detector would appear as a difference in the count rates for flipped $\downarrow$ and unflipped $\uparrow$ pulses. If photons reaching a particular detector make an angle θ with the

direction of the neutron spin, and follow the anticipated angular distribution

$$\frac{d\Gamma}{d\Omega} \propto 1 + P_{\mathrm{n}} A_\gamma \cos\theta, \tag{1}$$

then reversing the sign of the neutron polarization P_{n} is equivalent to reversing the sign of the asymmetry A_γ. The symmetry of the detector array means that each scintillator has a "parity-conjugate" partner with similar angular acceptance but opposite "unflipped" spin direction. From the sums and differences of photocurrents from $\uparrow$ and $\downarrow$ pulses in a pair of detectors, one can extract not only the parity-violating asymmetry A_γ but also the rich set of diagnostic information discussed in chapter 3. The experiment has been designed so that systematic effects contribute false asymmetries at less than a few $\times 10^{-9}$, permitting a statistics-limited measurement of A_γ to 10% of its predicted value [Gericke et al., 2005; Snow et al., 2000].

This dissertation describes in detail the $\vec{\mathrm{n}} + \mathrm{p} \rightarrow \mathrm{d} + \gamma$ experiment. After a review of the hadronic weak interaction, the design and performance of the components of the apparatus will each be discussed. Comparisons among the various possible analyses will be made to justify the results presented from the 2006 hydrogen data obtained at Los Alamos. As we shall see, the statistical sensitivity obtained in this work was not sufficient to reach a desired sensitivity of $\sim 10^{-8}$. We propose to repeat the experiment at the Spallation Neutron Source (SNS) to achieve this design precision; the final chapter details some of the changes required to adapt the apparatus to the new facility.

Chapter 1

The hadronic weak interaction

Parity is the symmetry operation under which the coordinates used to label location in space change sign:

$$\hat{P}f(x,y,z) = f(-x,-y,-z) \qquad \text{for any function } f. \tag{1.1}$$

With an extra rotation, a parity transformation is equivalent to using a "left-hand rule" rather than a "right-hand rule" to decide the direction of the third axis. Since two successive parity transformations $\hat{P}^2$ must return the original function $f(+x,+y,+z)$, eigenfunctions of $\hat{P}$ may have only the eigenvalues ± 1. "Polar vectors" pointing to a location from the origin change sign under parity; even functions of polar vectors, like a "scalar" length $\vec{r}^{\,2} = x^2 + y^2 + z^2$ or an "axial" vector $\vec{r} \times \vec{p}$, do not. Parity is one of the discrete symmetries of the Lorentz group, along with time reversal $t \to -t$ and complex conjugation or "charge reversal" $i \to -i$.

The theories of electromagnetism and gravitation predict no phenomena in which an experiment could distinguish between left- or right-handed coordinates. Purcell and Ramsey first noted in 1950 that parity conservation in interactions among nuclei and elementary particles was an untested experimental question, constrained most strongly by a rather weak upper limit $3 \times 10^{-5}\ e \cdot \text{fm}$ on the neutron's electric dipole moment (EDM). Lee and Yang [1956] later argued that experimental evidence constrained parity nonconservation in strong and electromagnetic transitions much more strongly than in weak decays, and suggested several experiments where parity violation in weak decays would manifest itself as a geometrical effect.

The results of these first experiments, in the β decay of ^{60}Co [Wu et al., 1957] and in the sequence $\pi \to \mu \to e$ [Friedman and Telegdi, 1957; Garwin et al., 1957], made it quickly apparent that weak decays break parity maximally, coupling only to "left-handed" particles. Almost immediately Tanner [1957] published a strong upper limit on the parity-forbidden transition $^{20}\text{Ne}^*(1^+) \to$

$\alpha + {}^{16}\mathrm{O}$(g.s.), estimating an odd-parity contribution to the ground states of ${}^{4}\mathrm{He}, {}^{16}\mathrm{O}$ smaller than 2×10^{-4}. The Lee-Yang limits on parity violation in strong and electromagnetic interactions were weakened somewhat by the observation of Landau [1957] that an EDM breaks invariance not only under parity, but under simultaneous conjugation of parity and charge — an approximate symmetry of weak decays as well. This led to a large number of searches for hadronic parity mixing, classified by Wilkinson [1958a,b,c] into searches for

(i) violations of selection rules, as in Tanner [1957]

(ii) polarization from unpolarized sources

(iii) odd powers of $\cos\theta$ in the angular distribution of decay products.

In a fairly short time, a body of null results demonstrated that hadronic parity violation occurs at or below the "natural" scale $G_F m_\pi^2 \left(\frac{c}{\hbar^3}\right) \sim 10^{-7}$ of strong-weak interference. This interaction mixing presented an opportunity to use hadronic parity violation as a tool for exploring the current-current model of the weak interaction [Blin-Stoyle, 1960a; Michel, 1964].

However, the small size of the predicted parity-violating effects, combined with a lack of the precise knowledge of other contributions to the interaction required to interpret results, proved challenging obstacles. For instance, the first purported observation of hadronic parity nonconservation [Abov et al., 1964], an asymmetry $A_\gamma = -(3.7 \pm 0.9) \times 10^{-4}$ in the distribution of photons from polarized neutron capture on ${}^{113}\mathrm{Cd}$, was not reproduced by other groups.[1] On the other hand, the first definitive observation by Lobashov et al. [1967], a circular polarization $P_\gamma = -(6 \pm 1) \times 10^{-6}$ in a transition of ${}^{181}\mathrm{Ta}$ following the β decay from ${}^{181}\mathrm{Hf}$, was some thirty times smaller than an earlier reported observation by Boehm and Kankeleit [1965] in the same system. These obstacles continue to challenge experiments in the field today.

The tantalum experiment of Lobashov et al. warrants some special discussion as the first to use integral photon counting. Photons from a 500 Ci ($= 10^{13}$ decay/s) source reached a photodiode by scattering from magnetized iron plates. The magnetization direction was reversed at 0.5 Hz. The photocurrent was sent to a resonance amplifier tuned to the same frequency, whose output in turn was used to drive a precision torsion pendulum. Interestingly, the frequency stability of the pendulum was some ten times better than the frequency stability of the electronics available at the time.

The 1970s saw a great deal of activity in parity violation searches in atoms and nuclei; one review [Commins and Bucksbaum, 1983, page 366] lists fifteen results in a dozen or so systems. The evidence for neutral currents in leptonic and semileptonic scattering events in the ν_μ beam at CERN [Hasert et al., 1973a,b, 1974] lent support to the unified electroweak theory of Weinberg [1967]

[1] Two subsequent publications on $\vec{\mathrm{n}} + {}^{113}\mathrm{Cd}$ reported $A_\gamma = -(60 \pm 180) \times 10^{-6}$ [Warming, 1969, who refers to several other null measurements] and $A_\gamma = -(3.2 \pm 4.5) \times 10^{-6}$ [Mitchell et al., 2004].

and Salam and Ward [1964]. However Lobashov et al. [1972] reported a tantalizingly large polarization $P_\gamma = -(1.30 \pm 0.45) \times 10^{-6}$ in the photons from thermal neutron capture in water, suggesting that perhaps a different set of rules applied in the hadronic sector. Furthermore the first searches [Close, 1976] for parity nonconservation in atomic transitions, due to electron-nucleus neutral currents, seemed at variance with the observed parity violation in neutrino beam neutral currents [Benvenuti et al., 1976]. For a time, these experimental inconsistencies even cast doubt on the validity of a flavor-independent weak interaction. This murkiness was the context for the first search [Cavaignac et al., 1977] for parity violation in the angular distribution of photons in $\vec{\mathrm{n}} + \mathrm{p} \rightarrow \mathrm{d} + \gamma$, the subject of this dissertation. The direct observation of the weak vector bosons at CERN, a convincing refutation of the neutron-proton P_γ experiment [Knyazkov et al., 1984], and advances in atomic parity violation theory and experiment [see e.g. Commins and Bucksbaum, 1983, chapter 9] did not settle the issue for several more years.

Since then, a long run of well-known experimental successes involving the leptonic and semileptonic weak interactions has provided overwhelming support for the electroweak standard model. Fermions are apparently divided into six flavor doublets, the leptons $\binom{\nu_e}{e}, \binom{\nu_\mu}{\mu}, \binom{\nu_\tau}{\tau}$ and quarks $\binom{u}{d}, \binom{c}{s}, \binom{t}{b}$, whose members may transform into each other by interaction with the (left-handed) charged weak current. Those particles with electric charge (that is, all but the ν) may exchange photons, which conserve parity and have infinite range; all particles, with any helicity, may exchange the parity-mixing Z. The weak couplings appear to be "universal," in the sense that they are independent of flavor.

At the same time, advances in computational speed and storage capacity have permitted a very productive tactical shift in the understanding of strong interactions. The basic features of quantum chromodynamics (QCD), that quarks carry an additional "color" charge and that physical hadronic states contain quarks and antiquarks in color singlets, were also known by the early 1980s. But the $SU(3)$ structure of the color force means that the gauge bosons mediating the force also carry color charge, while their small mass[2] gives them very long range. Quark-quark interactions therefore succumb to perturbative approximations only at very short distances; the dynamics of low-energy strongly interacting systems, like the nucleon, are dominated by the self-interacting gluon field. Historically this situation meant that fundamental approaches could effectively treat heavy-quark and high-energy strong processes, but that low-energy nucleon-nucleon interactions required approximate approaches like meson exchanges or mean field theories. Increased computational complexity steadily closes the gap between these two classes of approach.

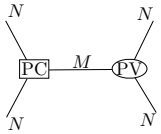
The primary motivation for the class of hadronic weak interaction experiments underway today is reversed, in a sense, from the original experiments above: the known charged weak coupling between quarks permits exploration

[2] Theoretical treatments of QCD use massless gluons. The Particle Data Group [Yao et al., 2006, hereafter the PDG] notes that a gluon mass of a few MeV "may not be precluded." Compare the length scales discussed in section 1.4.

of the short-range structure of QCD. But on the other hand, hadronic parity violation is the only accessible laboratory for observing strangeness-conserving quark-quark neutral currents.

1.1 The meson-exchange framework

Theoretical and experimental discussions of the strangeness-conserving hadronic weak interaction have, until recently, used the meson-exchange language developed by Desplanques, Donoghue, and Holstein [1980, hereafter DDH]. In essence, the DDH method describes the two-nucleon weak interaction by the weak nucleon-meson couplings. In a low-energy process where nucleon-meson exchanges adequately describe the strong interaction, parity nonconservation can then be described by an exchange



(1.2)

with one parity-violating vertex. A theorem by Barton [1961] shows that exchange of neutral, spinless mesons cannot violate P in the limit where CP symmetry is conserved.[3] Of the mesons too light to decay to strange particles, Barton's constraint leaves only the charged $\pi^{\pm}$, the charged and neutral ρ, and the neutral ω.

In few-nucleon systems where electric charge can be neglected, the strong interaction is invariant under "isotopic rotations" exchanging protons and neutrons. Eigenstates of the strong interaction therefore have "isospin" quantum numbers T, T_0 in addition to the usual angular momenta due to spin S, orbital motion L, and their vector sum J. In a nuclear state with quantum numbers J^P, T, the parity $P = (-1)^L$ and the Pauli symmetry requirement $(-1)^{L+S+T} = -1$ restrict the L and S wavefunctions which may contribute. Mixtures with indefinite parity but definite angular momentum can therefore be classified by whether they also mix isospin. The five S-P mixtures in the two-nucleon system are, in the notation ${}^{2S+1}L_J{}^T$,

$$\begin{aligned} &\left\langle {}^3S_1{}^0 \,\middle|\, H_W^1 \,\middle|\, {}^3P_1{}^1 \right\rangle, \\ &\left\langle {}^3S_1{}^0 \,\middle|\, H_W^0 \,\middle|\, {}^1P_1{}^0 \right\rangle, \\ &\left\langle {}^1S_0{}^1 \,\middle|\, H_W^{0,1,2} \,\middle|\, {}^3P_0{}^1 \right\rangle. \end{aligned} \tag{1.3}$$

The DDH potential relates the amplitude of $H_W^{\Delta T}$ to the the weak meson couplings $h_M^{\Delta T}$: $h_\pi^1, h_\rho^{0,1,2}, h_\omega^{0,1}$. While the meson-coupling notation appears in

[3] It is not immediately clear to this author how strongly the known CP nonconservation affects Barton's argument. In strangeness-conserving nucleon-nucleon interactions, contributions to CP breaking from the kaon sector cannot contribute at first order. If CP violation is nonnegligible at a nucleus-π^0 or nucleon-η vertex, these mesons could contribute to the isospin-conserving hadronic weak interaction.

the literature as early as Michel [1964], DDH was the first work to treat the isoscalar and isovector couplings on an equal footing and the first to relate the strangeness-conserving weak interaction to the hyperon decays in a quantitative way.

1.2 Charged and neutral currents in the two-nucleon system

The segregation of strangeness-conserving hadronic weak interactions by isospin was recognized early on [Danilov, 1965] as a way to distinguish charged and neutral weak currents. A $W^{\pm}$ vertex couples a u quark to the mixture $d\cos\theta_C + s\sin\theta_C$, which changes the isospin projection[4] by $\Delta T_0 = 1/2$ or 1; two such vertices, without the introduction of strangeness, may change the isospin by $\Delta T = 0, 1, 2$. However the $\Delta S = 0$, $\Delta T = 1$ channel is suppressed by the smallness of Cabibbo mixing, with $\sin^2\theta_C \approx 0.04$. Parity mixing in this channel, then, is dominated by the neutral current. In the radiative capture of low-energy neutrons by hydrogen, the $\Delta T = 0, 1$ channels further separate into distinct observables P_γ and A_γ. This section outlines the physics underlying this separation.

The two-nucleon system has a single bound state with $J^P, T = 1^+, 0$. This state has the approximate form

$$|\mathrm{d}\rangle = \sqrt{0.96}\left|{}^3S_1{}^0\right\rangle + \sqrt{0.04}\left|{}^3D_1{}^0\right\rangle + \epsilon^1\left|{}^3P_1{}^1\right\rangle + \epsilon^0\left|{}^1P_1{}^0\right\rangle \qquad (1.4)$$

where the D-wave is responsible for the deutron's quadrupole moment. The coefficients $\epsilon^{\Delta T}$ vanish in the absence of a parity-mixing interaction in the corresponding isospin channel. We follow Gari and Schlitter [1975] and Byrne [1994] in labelling transitions by the J of the radiating state. The dominant mode of capture is the magnetic dipole transition $\left\langle {}^3S_1{}^0 \middle| m(0) \middle| {}^1S_0{}^{1u}\right\rangle$ from the unbound 0^+ state. About 10% of the capture comes from the transition $\left\langle \mathrm{d} \middle| m(1) \middle| {}^3S_1{}^{0u}\right\rangle$; the magnetic dipole operator does not change the fact that the bound and excited S wavefunctions are orthogonal. Parity mixing in the capture radiation comes from interference with the electric dipole transitions $\epsilon^0\left\langle {}^1P_1{}^0 \middle| e(0) \middle| {}^1S_0{}^{1u}\right\rangle$ and $\epsilon^1\left\langle {}^3P_1{}^1 \middle| e(1) \middle| {}^3S_1{}^{0u}\right\rangle$, as well as conjugate transitions from any unbound P waves to the ground state.[5] The "singlet-triplet" transitions $\left\langle {}^1P \middle| \mathrm{E1} \middle| {}^3S\right\rangle$ are hindered since the orthogonal spin wavefunctions do not see the electric dipole operator. This leaves the four electric dipole transitions shown in figure 1.1 to interfere, with the unbound state's J equal to the isospin change ΔT of the parity-mixed part of the ground state.

The parity-violating observables possible in photon transitions of different multipolarities were first compiled by Blin-Stoyle [1960b]. For photon emission

[4] In this treatment we switch cavalierly between the strong isospin doublet (u, d) and the weak isospin doublet $(\mathrm{u}_L, \mathrm{d}_L\cos\theta_C + \mathrm{s}_L\sin\theta_C)$.

[5] The unbound P-waves also give rise to the parity-allowed analyzing power. Parity mixing in the unbound state carries the same quantum numbers as parity mixing in the ground state.

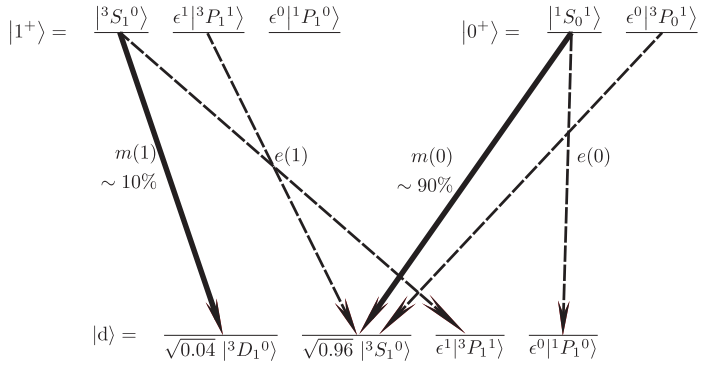


Figure 1.1: Transitions in n-p capture. Transitions are labeled by the angular momentum J of the unbound state; those omitted are hindered as described in the text. In the surviving cases, the parity-mixing coefficient $\epsilon^{\Delta T}$ permits an electric dipole transition from the unbound state with $J = \Delta T$.

from an unpolarized nucleus, Blin-Stoyle gives a circular polarization

$$P_\gamma = 2\,\frac{\sum_L m_L^* e_L}{\sum_L (|m_L|^2 + |e_L|^2)} \tag{1.5}$$

due to interference between magnetic and electric multipoles of order L. In unpolarized capture the unbound 0^+ and 1^+ states are not coherent and their cross terms do not interfere, giving

$$P_\gamma(\vec{\mathrm{n}} + \mathrm{p} \to \mathrm{d} + \gamma) = 2\frac{m(0)e(0) + m(1)e(1)}{|m(0)|^2 + |m(1)|^2} \approx 2\frac{e(0)}{m(0)}. \tag{1.6}$$

This electric dipole amplitude is proportional to the isoscalar ($\Delta T = 0$) weak mixing.

For thermal neutrons with polarization P_n incident on an unpolarized nucleus with spin J_i, Blin-Stoyle gives an angular distribution

$$W(\theta) \propto 1 + A_\gamma \cos\theta \tag{1.7}$$

for the photons emitted in a transition $J \to J'$ with interference between electric and magnetic multipoles of the same order L. The asymmetry has the form

$$A_\gamma = 2P_\mathrm{n}\frac{J_i(J_i+1) - J(J+1) - \frac{3}{4}}{\sqrt{3J(J+1)}} \cdot F_1(LLJ'J) \cdot \frac{m_L^* e_L}{|m_L|^2 + |e_L|^2} \tag{1.8}$$

where F is a coupling coefficient tabulated by Alder et al. [1957]. For capture onto hydrogen from the $J = 0$ compound state, this expression vanishes. For the $J = 1$ photons, coupling to the $\Delta T = 1$ weak amplitude,

$$A_\gamma^{(J=1)} = +P_\mathrm{n}\frac{m(1)^* e(1)}{|m(1)|^2 + |e(1)|^2}. \tag{1.9}$$

Against an incoherent, spherical background of $m(0)$ photons with the same energy, the observable asymmetry becomes $A_\gamma \approx m(1)e(1)/m(0)^2$.

This expression for the $\vec{\mathrm{n}} + \mathrm{p} \rightarrow \mathrm{d} + \gamma$ asymmetry is smaller than the standard expression in the literature by a factor $m(1)/m(0) \simeq 0.1$. We account for the discrepancy by noting that the treatment of Blin-Stoyle [1960b] took place before the introduction of integral counting by Lobashov et al. [1967], and assumes implicitly that the initial and final J can be determined from the photon energy. We have argued above that the dominant transition in $\vec{\mathrm{n}} + \mathrm{p} \rightarrow \mathrm{d} + \gamma$ is the $m(0)$ transition from the unbound 0^+ state. In order for the neutrons to be polarized there must be some coherence between the unbound 0^+ and 1^+ states. If the neutron and proton spin wavefunctions are

$$|\mathrm{n}\rangle = |\uparrow\rangle \quad \text{and } |\mathrm{p}\rangle = \frac{e^{i\phi}\,|\uparrow\rangle + |\downarrow\rangle}{\sqrt{2}}, \tag{1.10}$$

then their product $|S, m_S\rangle$ is

$$|\mathrm{np}\rangle_{\mathrm{spin}} = e^{i\phi}\frac{|1,1\rangle}{\sqrt{2}} + \frac{|1,0\rangle - |0,0\rangle}{2}. \tag{1.11}$$

The coherent combination of the 0^+ and 1^+ unbound states allows $m(0)e(1) + m(1)e(0)$ interference; evaluating the coefficient requires some manipulation of angular momentum couplings. This has been done by several authors; Byrne [1994] quotes the Gari and Schlitter [1975] expression

$$A_\gamma = -\sqrt{2}\frac{m(0)e(1) + m(1)e(0)}{|m(0)|^2} \approx -\sqrt{2}\frac{e(1)}{m(0)} \tag{1.12}$$

while a pedagogically accessible treatment appears in Gericke [2004]. This electric dipole transition is proportional to the isovector ($\Delta T = 1$) weak mixing. Our expression (1.9) for the interference between the two m substates from the $J = 1$ transition apparently contributes a correction at the same level as the isoscalar $e(0)$ amplitude.

1.3 The modern experimental situation

Of the experiments discussed above, most involve reactions in nuclei either large ($A \gtrsim 10$), highly excited, or both. In first-order perturbation theory, the opposite-parity contribution to an unperturbed state $|\psi^+\rangle$,

$$\left|\widetilde{\psi}^+\right\rangle = \left|\psi^+\right\rangle + \sum_i \left|\psi_i^-\right\rangle \frac{\left\langle \psi_i^- \left| H_W \right| \psi^+ \right\rangle}{E_i - E_+}, \tag{1.13}$$

is enhanced if the mixing states are nearby in energy. With no other information, this enhancement is most likely in systems with many closely spaced levels. The DDH calculations of the weak couplings prompted a search for systems where the weak matrix elements could either be expressed in a few-(quasi)particle basis or related to another nuclear transition. The strongest constraints in the late 1990s came from

- A set of null measurements $|P_\gamma| \lesssim 5 \times 10^{-4}$ of circular polarization in photons emitted from the $J^P, T = 0^-, 0$ level of ^{18}F at 1080 MeV. The energy of this level is only 39 keV above a $0^+, 1$ level with a lifetime shorter by 10^4. This transition has theoretical appeal because the M1 and E1 matrix elements can be measured independently, and the weak mixing is related by an isospin rotation to the (charged current) positron decay of ^{18}Ne$(0^+, 1)$ to the ^{18}F$(0^-, 0)$ level [Adelberger et al., 1983; Page et al., 1987]. The null ^{18}F measurements exclude the DDH "best value" for the pion coupling constant at about 4–5σ [Bini et al., 1985, 1988].

- A nonzero asymmetry $A_\gamma = -(6.8 \pm 2.1) \times 10^{-5}$ in the photons from the 110 keV $1/2^-$ level of ^{19}F, interpreted as parity-violating mixing between that level and the $1/2^+$ ground state [Elsener et al., 1984, 1987]. This mixing is also related by an isospin rotation to a positron decay branching, in ^{19}Ne [Adelberger et al., 1983], and probes a mixture of the $\Delta T = 0, 1$ couplings.

- Two null circular polarization measurements $|P_\gamma| \lesssim 10^{-3}$ indicating an upper limit on mixing between the $1/2^\pm$ levels in ^{21}Ne at 2.789 MeV [Earle et al., 1983; Snover et al., 1978]. Those two levels are separated by only 5.3 keV and have a 10^4 difference in lifetime. This is one of only a few favorable transitions in an odd-N, even-Z nucleus, and the asymmetry has a different isospin structure than in odd-Z nuclei. However the slope of the ^{21}Ne constraint in the isoscalar-isovector plane is not terribly well-established [Bowman, private communication].

- A set of parity-violating analyzing power measurements with polarized medium-energy proton beams $\vec{\mathrm{p}}$ on p, ^{4}He, d at various energies. As elastic proton-proton scattering cannot involve single $\pi^\pm$ exchange, the energy dependence of parity violation in that system allows one to isolate the relative contributions of the shorter-range coefficients.

Two reviews ten years apart [Adelberger and Haxton, 1985; Haeberli and Holstein, 1995] interpreted these data as evidence, with some murkiness, for a weak pion-nucleon coupling small relative to the DDH value.

In 1997 Wood et al. published evidence for nuclear spin dependence in the parity-violating electric dipole transition between the $6S$ and $7S$ electronic states of ^{133}Cs. Only about 15% of this spin dependence was expected from the relationship between electron-nucleus Z exchange and the hyperfine interaction; the remainder was interpreted as evidence for an "anapole moment" aligned with the cesium nuclear spin ($J^P = 7/2^+$). An anapole moment is a P-odd, CP-even electromagnetic moment carried e.g. by a toroidal electric current and the associated (localized) magnetic field.[6] While the theoretical possibility of a nuclear anapole moment and its possible contribution to atomic parity violation had been known for a long time, the effect seen by Wood et al. [1997]

[6] A crystal with bulk anapole moment, in "ferrotoroidic domains" independent of its ferromagnetic domains, has recently been reported [Aken et al., 2007; Rabe, 2007].

was larger than predicted by existing calculations with the anapole moment due to the unpaired proton [Haxton, 1997, and references therein]. The discrepancy appeared using the DDH "best values," increased using the experimentally suggested small h_π^1, and remained in a much larger calculation using a shell model with some 200 000 basis states [Haxton, Liu, and Ramsey-Musolf, 2001]. Furthermore those calculations predicted comparable anapole moments in ^{133}Cs and ^{205}Tl. An existing measurement of parity-violating optical activity in the $6P_{1/2} \rightarrow 6P_{3/2}$ transition of ^{205}Tl ($J^P = {}^1/_2{}^+$) reported an anapole moment $\kappa_a = -0.22 \pm 0.30$, consistent with zero but not with the predicted $\kappa_a \sim +0.40$ [Vetter et al., 1995].[7]

This confusion has prompted a new generation of high-precision searches for parity violation in few-nucleon systems, where the problems of nuclear structure are more tractable. Several of these experiments involve cold neutrons. This dissertation describes an upper limit on the longitudinal photon asymmetry A_γ in $\vec{\mathrm{n}} + \mathrm{p} \rightarrow \mathrm{d} + \gamma$, and argues that the apparatus used can probe the weak couplings in the DDH reasonable range at the SNS. A proposal has been submitted to use the same spectrometer at SNS with a deuterium target. A new measurement of the parity-violating spin rotation of polarized neutrons in ^{4}He has recently taken data at NIST [see e.g. Bass et al., 2005]. And a proposal has been put forward to measure parity mixing in the spin-dependent capture of polarized neutrons by helium-3. Berdoz et al. at TRIUMF have measured [2003] parity-violating analyzing power in $\vec{\mathrm{p}}\,\mathrm{p}$ scattering at 221 MeV, where the $\Delta T = 0$ amplitudes cancel and only the $\Delta T = 2$ weak interaction contributes. These systems, in combination with the existing few-nucleon data, seem to be adequate to constrain the two-nucleon couplings, even in the new approaches described below.

1.4 Modern theoretical approaches

The apparent failure of the meson-exchange model of hadronic weak interactions has prompted theoretical activity as well. An interaction mediated by the exchange of a virtual boson with mass m has the Yukawa potential

$$V \propto \hbar c \frac{e^{-mr \cdot c/\hbar}}{r} \tag{1.14}$$

which vanishes at separations $r \gtrsim \hbar/mc$. In the nucleus the π generates an attractive potential within a distance $r \sim 1.2\,\mathrm{fm}$, while the ρ and ω produce a hard repulsion within a "core" $r \lesssim 0.2\,\mathrm{fm}$. Both of these distances are much longer than the effective length $\sim 0.002\,\mathrm{fm}$ over which nucleons may interact by W and Z exchanges. This separation of length scales formed part of the motivation for the DDH approach, where the weak interaction is buried within a nucleon-meson vertex.

[7] We note that ^{205}Tl differs from the doubly-magic nucleus ^{208}Pb by only three quasiparticles, while ^{133}Cs is much farther from the 50- and 82-nucleon closed shells.

However, the nucleon is not a pointlike object but a relativistic composite of quarks, virtual quark-antiquark pairs, and a self-interacting gluon field. Weak boson exchanges among the (real and virtual) quarks probe short-range correlations within this structure. For processes described by pion exchange the approximation of a single parity-violating vertex may remain sensible. But two nucleons close enough to exchange ρ or ω mesons overlap each other significantly, and the assumption that direct NN weak exchanges are suppressed — or, that NN weak interactions must carry the quantum numbers of ρ or ω exchange — becomes questionable.

Recent years have seen increased use of effective field theory (EFT) in treatments of few-nucleon interactions. In EFT, long-range processes (typically those with momentum transfer $\hbar Q$ smaller than the pion mass) are treated with meson exchanges, while short-range processes are treated as contact interactions with the symmetries required by the quantum numbers involved. This strategy reduces the dependence of a calculation on ad hoc assumptions in the microscopic model of the interaction. Zhu et al. [2005] show that in "pionless" EFT, where pion exchanges are also buried in contact interactions, the use of realtivistically invariant nuclear wavefunctions doubles the number of independent low-energy parity violating mixtures from five to ten. In the nonrelativistic limit, phase relationships constrain these constants again to five independent parameters, as in the DDH case (1.3). But in interactions with center-of-mass energy above $\sim 50\,\mathrm{MeV}$, the pion must be treated explicitly and excluded from the contact terms. This "pionful" EFT has three additional parity-violating parameters, since the dynamical pion may also contribute to second-order processes. While quantitative connections between these new approaches and observable parity-violating effects are still being established [see e.g. Liu, 2007], analysis is again more straightforward in the few-nucleon sector.

This chapter has provided a rather broad phenomenological overview of the hadronic weak interaction, without going too deeply into theoretical details. Several more comprehensive discussions have appeared elsewhere. Desplanques and Holstein have recently produced several brief but cogent summaries of the field [see e.g. Desplanques, 2005; Holstein, 2007, 2004], while Ramsey-Musolf and Page [2006] offer a more comprehensive review.

Chapter 2

The $\vec{\mathrm{n}} + \mathrm{p} \rightarrow \mathrm{d} + \gamma$ experiment

The $\vec{\mathrm{n}} + \mathrm{p} \rightarrow \mathrm{d} + \gamma$ experiment aims to measure the correlation A_γ between neutron spin and photon direction in the capture of polarized cold neutrons on parahydrogen. This chapter describes the experiment as it operated on Flight Path 12 (FP12) at the Manuel Lujan neutron scattering facility located at the Los Alamos Neutron Science Center (LANSCE) through the end of 2006.

At LANSCE, neutrons are produced in short pulses at 20 Hz when a $\sim 100\,\mu\mathrm{A}$ beam of 800 MeV protons strikes a tungsten spallation target. The neutrons are slowed down by elastic scattering with beryllium and steel "reflectors." Ultimately the neutrons scatter from a partially coupled cold hydrogen moderator and travel 20 m down a straight, $m = 3.5$ supermirror guide with area $9.5 \times 9.5\,\mathrm{cm}^2$. A chopper stops slow neutrons that would otherwise reach the experiment during a subsequent pulse, providing a unique relationship between time of flight and neutron energy. At the end of the guide, a thin ^{3}He ion chamber measures the neutron flux as a function of time of flight. The neutrons then pass through a large area (10 cm diameter) nuclear spin polarized ^{3}He cell, which polarizes the neutrons; a second thin ion chamber; and a radio-frequency spin flipper, which reverses the spin of the neutrons on a pulse-by-pulse basis in the pattern $\uparrow\downarrow\downarrow\uparrow\downarrow\uparrow\uparrow\downarrow$. Immediately downstream of the spin flipper is a 16 L volume of liquid hydrogen at 17 K, containing $< 0.03\%$ orthohydrogen. Roughly 60% of the beam captures in the hydrogen, each capture emitting a single 2.2 MeV γ ray. Neutrons which neither capture nor scatter in the target stop in a final, thicker, ion chamber, or in a ^{6}Li beam stop. Enclosing the target are four rings of twelve $15 \times 15 \times 15\,\mathrm{cm}^3$ CsI scintillators, which convert 95% of the γ energy within a solid angle of $\sim 3\pi$ into visible light. Vacuum photodiodes convert the scintillation light to a photocurrent. To enable subtraction of similar signals at high precision over a large dynamic range, the photocurrents for each ring are converted to a sum and twelve difference signals prior to being digitized. From the end of the neutron guide to the final detector, the experiment is in a uniform 10 G magnetic field. This chapter describes this sequence of events in detail.

2.1 Neutron production on FP12 at LANSCE

The LANSCE linear accelerator began operation in 1973 as the Los Alamos Meson Physics Facility (LAMPF), and began operation as a neutron source in the late 1990s after the construction of the proton storage ring and the Lujan target facility.

A $\sim 100\,\mu$A current of negative hydrogen ions is produced by passing protons through a volume of cesium vapor at the energy of an electron capture resonance. This ion source sits at a potential $-750\,$kV relative to the rest of the accelerator, providing the first stage of acceleration as the ions enter the 200 MHz drift tube linac. Up to about 200 MeV kinetic energy, the proton velocity varies enough that the spacing between the accelerating electrodes must increase as the protons speed up. Acceleration beyond this energy occurs in resonant microwave cavities driven at 800 MHz, where localized electric fields may transfer energy to the beam much more efficiently than in the drift tube section. In this region the acceleration condition is met by adjusting the phase of the oscillating field in each cavity. At the end of the linac each H^- ion has kinetic energy 800 MeV.

From the linac, the beam may be steered to several different facilities. The Lujan beam is sent through a very thin carbon foil to strip both electrons from the hydrogen ions. The charge reversal allows the proton pulses to accumulate in a storage ring. Every 50 ms the storage ring is emptied, and a proton bunch $\sim 250\,$ns in duration strikes the Lujan spallation target.

The LANSCE tungsten metal spallation target is of sufficient thickness to stop the proton beam. The protons are energetic enough that many different nuclear processes occur in the target. These include copious production of free π, K, and other exotica with masses below the beam energy; evaporation of protons and neutrons; proton-induced fission into various, mostly neutron-rich isotopes; and γ cascades from short- and long-lived intermediate nuclear states. The only long-lived neutral components of this mess are neutrons, photons, and neutrinos; these dominate the radiation field far from the target and after the prompt production event.

Each incident proton liberates on average a few dozen spallation neutrons. Neutron energies range from near zero up to the incident proton energy. Prompt spallation neutrons have energies anywhere from a few MeV to hundreds of MeV. Cold neutrons are produced by interaction with a moderating material — in the case of FP12, a volume of liquid hydrogen. The neutrons that thermalize in the moderator emerge over a period of $\sim 100\,\mu$s. This time is long compared to their production time during the 250 ns proton pulse, but short compared with the flight time down the beamline to the experiment.

2.1.1 Beam transport

The neutrons leaving the moderator have the approximately thermal spectrum shown in Figure 2.1, with the most intensity near 3 meV. The beam then passes down 20 m of guide to the experiment.

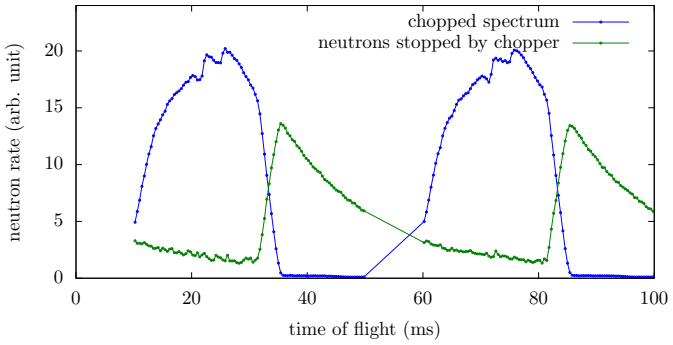


Figure 2.1: Spectrum at the end of Flight Path 12. Spallation pulses strike the proton target at $0, 50, 100, \cdots$ ms. Data taking is suspended during the first 10 ms of each pulse, when fast neutrons and gammas are present. The chopper removes the slow neutrons (green) that wrap around to the subsequent pulse. Neutrons in the intensity peak at 25 ms have wavelength 5 Å.

Because the moderator cools the neutrons via a large number of elastic scatterings, neutrons leave the moderator face traveling in every direction. Neutrons, unlike charged particles, cannot be easily accelerated or steered with electric or magnetic fields.[8] The neutron flux from an isotropic distribution falls off like the square of the distance from the source. However, if the flight path from the neutron source to the experiment is simply enclosed, the intensity falls off less steeply than r^2: some neutrons that would otherwise escape scatter from the enclosure and reach the experiment anyway. (Apocryphally, the first neutron flight tube was a copper pipe salvaged from the trash pile by Fermi, which tripled his experiment's count rate.) Modern cold neutron flight paths are walled with "supermirror guides," which have good reflectivity for all neutrons emitted from the moderator into a particular solid angle.

The optical performance of a neutron guide can be understood using the Born approximation. For scattering from a single nucleus at the origin, we may write the neutron wavefunction in the zero-potential region at large r as a sum of incident and scattered waves:

$$|\mathrm{n}\rangle = e^{i\vec{k}\cdot\vec{r}} + \frac{e^{ikr}}{r} \sum_{\ell} \frac{e^{2i\delta_\ell(k)} - 1}{2ik} (2\ell + 1)\ P_\ell(\cos\theta) \tag{2.1}$$

The neutron has momentum $\vec{p} = \hbar\vec{k}$, and wavelength $\lambda = 2\pi/k \simeq$ few Å, while the nuclear potential is nonzero over a length scale of a few fm $\simeq 10^{-5}$ Å. The phase shifts δ_ℓ come from fitting the outgoing waves to the wavefunction inside

[8] More correctly, the neutron's magnetic moment $\mu = 56\,\mathrm{neV/T}$ means that, for meV neutrons in laboratory fields, the neutron's magnetic energy is much smaller than its kinetic energy. However, see e.g. Golub, Richardson, and Lamoreaux [1991] for a discussion of "ultracold" neutrons with ~ 100 neV kinetic energies.

the nucleus. Within the nucleus the ℓth radial wavefunction varies like $(kr)^\ell$, so generally only the $\ell = 0$ term contributes. We may therefore consider only the s-wave scattering

$$|\mathrm{n}\rangle = e^{i\vec{k}\cdot\vec{r}} - a\frac{e^{ikr}}{r}. \tag{2.2}$$

where a is the "scattering length" of the nucleus.

Within the femtometer-wide, MeV-deep potential well near a nucleus, the neutron has fm-scale wavelengths rather than Å-scale wavelengths. We may solve for the long-distance radial wavefunction $u(r \to \infty) = ae^{ikr}$ with the condition that it vanish at the origin, with an effective square-well potential. Inside the nucleus the neutron wavefunction may have a few complete cycles; just outside the nucleus, k is so small that $u(r)$ is effectively linear. Far from the nucleus, then, the outgoing wavefunction is (apart from a phase shift) the same as that from an impenetrable sphere of radius a.

If the positions of the scatterers are random, or are at least uncorrelated with the neutron wavevector $\vec{k}$, we may treat the collective material as a uniform pseudopotential $V \propto \rho a$. For most materials, V is repulsive.

For scattering from a sufficiently smooth plane in vacuum, we may therefore treat the neutron using one-dimensional quantum mechanics for scattering from a potential step V. The relevant wavevector is the component $k_\perp$ perpendicular to the surface. The neutron will be completely reflected for energies $E_\perp = (\hbar k_\perp)^2/2m < V$. For most materials, $V \lesssim 100\,\mathrm{neV}$. For a 25 meV neutron, we find the maximum angle for total reflection

$$\theta_c = \frac{k_\perp}{k} = \sqrt{\frac{V}{E}} \sim 2 \times 10^{-3}\,\mathrm{radian}. \tag{2.3}$$

Neutrons grazing the mirror more shallowly than this are not quite totally reflected: the neutron wavefunction does penetrate some distance into the mirror, where the neutron may capture. However, a natural nickel mirror, with scattering length $b_C = 10.3(1)\,\mathrm{fm}$ and thermal absorption cross section $\sigma = 4.49(16)\,\mathrm{b}$ [NDB], has reflectivity $\gtrsim 0.98$ up the the critical angle $\theta_c = 1.7\,\mathrm{mrad/Å}$.

The supermirror, first implemented by Mezei [1976][9] as a polarizing device but now more commonly used for spin-independent transport, takes advantage of the fact that neutrons with $k_\perp$ just above the threshold for reflection all have the *same* $k_\perp$, corresponding to a length scale with period $\sim 1\,\mathrm{nm}$. Structures this size can be built by sputtering layers of materials with different neutron optical potentials on a surface. Neutrons with very small $k_\perp$ have effective wavelengths longer than the multilayer spacing and do not scatter cohereently from this structure; these still reflect from the substrate beneath. Neutrons with $1/k_\perp$ near the multilayer spacing, on the other hand, have a large probability to Bragg reflect from the multilayer. This extends the critical angle for nonzero reflection from θ_c to some larger angle $m\theta_c$. If the layer spacing varies above the substrate, neutrons with many different $k_\perp$ may find a region where the

[9] See also Turchin [1997] for an earlier description of neutron reflection from multilayered materials.

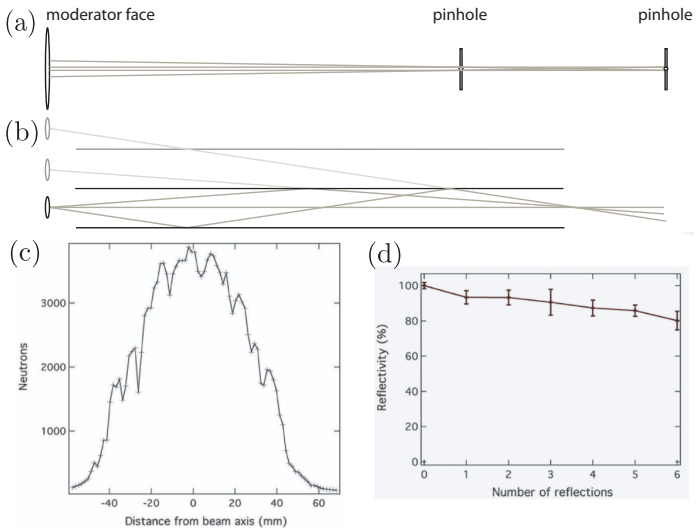


Figure 2.2: Two-pinhole system for viewing the moderator. (a) Solid angle viewing the moderator through two pinholes. (b) Moving the downstream pinhole chooses a reflection of the moderator. (c) Angular structure of the beam measured in a pinhole scan; (d) corresponding reflectivity. [(c) and (d) from Seo et al., 2005]

Bragg condition is approximately satisfied. Commercially available mirrors have $m = 3.5$–4, and $m = 6$ mirrors have been produced in small quantities. The ultimate limit on m comes from the degree to which adjacent layers diffuse into each other and lose definition. The number of layers needed overall — and thus, to first approximation, the cost to produce a given area of mirror — scales approximately like m^4.

The performance of the FP12 guide was measured during beamline commissioning following construction of the shielding cave in 2004, using the scheme illustrated in Figure 2.2. To measure the brightness of the moderator absolutely, the beam was collimated through two 0.5 mm diameter "pinholes" in gadolinium sheets, separated by about 2 m after the end of the guide. Immediately downstream of the second pinhole a high-efficiency ^{6}Li-loaded scintillator counted the surviving neutrons. The solid angle $d\Omega$ subtended by a small area dA from a distance r is $d\Omega = dA/r^2$. From the location of the second pinhole, the moderator face subtends a solid angle $(10 \times 10\,\mathrm{cm}^2)/(20\,\mathrm{m})^2 \approx 10^{-4}\,\mathrm{sr}$, while the upstream pinhole subtends a solid angle $\pi(0.5\,\mathrm{mm})^2/(2\,\mathrm{m})^2 \approx 10^{-7}\,\mathrm{sr}$. Every neutron entering the counter, then, came from a small spot on the moderator and followed a particular trajectory through the guide and the two pinholes. With the pinholes aligned along the beam axis, this permitted a direct observation of the moderator face. Movement of the second pinhole in the plane normal to the beam direction moved the spot on the moderator face. Eventually the spot moved from a direct view of the moderator to a view of the moderator as

reflected in the wall of the guide, providing a direct measurement of the guide's reflectivity. Figure 2.2 shows the angular distributions for 3 meV neutrons, and the extracted reflectivity curve for the FP12 guide.

2.1.2 Shielding and collimation

The spallation target and the upstream sections of the guide sit inside heavy radiation shielding. A shutter, which replaces ~ 1 m of guide with a steel beam stop, may be closed to allow access to the experimental cave while the accelerator is running. A tunnel of ~ 1 foot thick stacked reinforced concrete houses the downstream portion of the guide. The inside of the tunnel is lined with borated polyethylene, to moderate and capture fast neutrons that leak from the guide.

The experiment cave has two layers of soft iron, which act as a magnetic flux return for the experiment and magnetic shielding from the outside. The ~ 1 foot space between these layers is also filled with borated polyethylene.

Downstream of the guide, the beam is defined by a set of collimators. In the 2004 run these collimators were fabricated from sheets of borated polyethylene. However, the 480 keV photons from $^{10}\mathrm{B}(\mathrm{n},\alpha)^{7}\mathrm{Li}^{*}$ produced a large background in the detector. In 2005 and 2006, I fabricated new colliators from an epoxy loaded with lithium carbonate, enriched to 95% ^{6}Li, which captures neutrons predominantly by the photonless process $^{6}\mathrm{Li}(\mathrm{n},\alpha)^{3}\mathrm{H}$.

Because the $\sim 100\,\mu$s time for the neutrons to leave the moderator is short compared to the ~ 10 ms time for them to reach the experiment, all neutrons reaching a detector at a particular time must have the same velocity. However the spallation pulses repeat at 20 Hz, and slower neutrons produced in the moderator may reach a detector at the same time as faster neutrons from a previous pulse. A "frame-overlap" chopper, a slotted disc of absorber sitting in the upstream section of the guide and rotating in phase with the spallation pulses, acts as a velocity selector to prevent this contamination. Flight Path 12 used a single chopper, whose effects can be seen in Figure 2.1; chapter 4 discusses the more complicated system of choppers required for the beamline at the SNS.

2.1.3 Neutron beam monitors

The neutron beam intensity in the experiment is monitored continuously by a set of ^{3}He ion chambers. Each ion chamber is an aluminum enclosure containing a mixture of ^{3}He and ^{4}He, with a small partial pressure of nitrogen as a quench gas. The total detector pressure is ~ 1 bar, allowing thin entrance and exit windows. The helium content was stable over the operation of the experiment. Inside two high voltage planes produce an electric field ~ 3 kV/cm over part of the gas volume. Some neutrons passing through the monitor undergo the reaction $^{3}\mathrm{He}(\mathrm{n},\mathrm{p})^{3}\mathrm{H}$, liberating 750 keV kinetic energy. The proton and triton deposit this energy in the gas by ionization. The ions drift in the electric field. The high voltage planes collect the charge, a preamp converts it to a voltage, and it goes into the data acquisition system (DAQ) as described in section 3.1.

2.2 Neutron spin transport

Parity violation in $\vec{\mathrm{n}} + \mathrm{p} \to \mathrm{d} + \gamma$ appears as a correlation between spin and momentum — in this experiment, between the neutron spin $\vec{\sigma}_\mathrm{n}$ and the photon momentum $\vec{k}_\gamma$. To observe the asymmetry cleanly, the neutrons must be polarized and their spins must reverse without changing any other feature of the apparatus.

Parity-conserving scattering may produce polarized beams from unpolarized sources and samples in some geometries; nonzero polarization has been reported in the $\sim 100\,\mathrm{MeV}$ neutrons leaving the Weapons Neutron Research (WNR) spallation target at LANSCE [Boddy et al., 2005]. However, the interaction between neutrons and the liquid hydrogen of the moderator is dominated by spin-incoherent scattering. Assuming that a fast neutron loses roughly half its energy in each collision in the moderator, slowing from MeV to meV requires ~ 30 scatters. Any polarization of the neutron field incident on the moderator would be strongly diluted before the neutrons entered the guide; we may safely assume the neutron beam is completely unpolarized upstream of the ^{3}He spin filter.

2.2.1 Magnetic field

To define a quantization direction for the ^{3}He and neutron spins, the experiment sits within a $\sim 2 \times 3 \times 4\,\mathrm{m}^3$ set of coils, generating a uniform 10 G magnetic field over the neutron beam. As discussed in section 2.5.1, the uniformity requirement set by the allowable Stern-Gerlach steering of the beam is $\partial|B|/\partial z \lesssim 5\,\mathrm{mG/cm}$, while the alignment of the magnetic field with the vertical must be better than $\sim 20\,\mathrm{mrad}$. The installation, characterization, and shimming of the holding field are detailed in Lauss [2004].

2.2.2 Polarized ^{3}He spin filter

Downstream of the guide the neutron beam passes through a volume of polarized ^{3}He. The interaction between ^{3}He and low-energy neutrons is dominated by a narrow [$\Gamma = 500\,\mathrm{keV}$, ENSDF] unbound resonance in ^{4}He with spin and parity 0^+, which decays to $\mathrm{p} + {}^3\mathrm{H}$. The low-lying spin-one states of ^{4}He are further from the threshold energy and a factor of ten wider. If an unpolarized neutron interacts with polarized ^{3}He, then, only the half of the beam polarized in the opposite direction may capture. We may write the transmission T of a neutron beam with polarization P_n^0 through a length ℓ of ^{3}He with number density n and polarization P_3 as

$$\begin{aligned} T &= \frac{1 + P_\mathrm{n}^0}{2} e^{-n\ell\sigma(1-P_3)} + \frac{1 - P_\mathrm{n}^0}{2} e^{-n\ell\sigma(1+P_3)} \\ &= e^{-n\ell\sigma} \left(\cosh n\ell\sigma P_3 + P_\mathrm{n}^0 \sinh n\ell\sigma P_3 \right). \end{aligned} \tag{2.4}$$

Here $\sigma = \sigma_0 \lambda/\lambda_0$ is the $^3\mathrm{He}(\mathrm{n},\mathrm{p})^3\mathrm{H}$ cross section, which has the value $\sigma_0 = 5.333(7)\,\mathrm{kb}$ for neutrons with wavelength $\lambda_0 = 1.8\,\text{Å}$. Similarly, the polarization

P_n of the neutron beam exiting the cell is

$$P_\mathrm{n} = \frac{\sinh n\ell\sigma P_3 + P_\mathrm{n}^0 \cosh n\ell\sigma P_3}{\cosh n\ell\sigma P_3 + P_\mathrm{n}^0 \sinh n\ell\sigma P_3} = \frac{\tanh n\ell\sigma P_3 + P_\mathrm{n}^0}{1 + P_\mathrm{n}^0 \tanh n\ell\sigma P_3}, \tag{2.5}$$

which reduces to $\tanh n\ell\sigma P_3$ in the absence of any initial polarization.[10]

We polarize the ^{3}He by spin-exchange optical pumping [see e.g. Coulter et al., 1990]. In addition to ^{3}He, the spin filter cell contains some nitrogen gas and a droplet of rubidium metal. Rubidium vapor from this droplet fills the cell at a density determined by the temperature. Relatively broad-band laser light from a diode array drives a transition from the Rb ground state; because the light is circularly polarized, transitions where the "hyperfine" quantum number m_F changes by, say, $+1$ are preferred over $\Delta m_F = -1$. No such preference is exhibited by the transition back to the ground state. After many such transitions only the extreme m_F substates are populated: the ground-state rubidium has a net electron polarization.[11] Collisions between the Rb and ^{3}He have a small but finite probability of transferring this polarization to the ^{3}He nucleus. Since scattering by the ^{3}He atoms with the cell walls or other gas molecules is mostly an electronic process, the nuclear spin is pretty well-insulated. This insulation makes the time constant for Rb $\to$ ^{3}He spin transfer long, on the order of tens of hours. However the time constant for the ^{3}He to depolarize after pumping ends is quite long as well.

Spin-exchange cells are devices with a lot of individuality. Ordinary glass often contains boron, which has a large neutron capture cross section. In addition many common glasses allow helium to diffuse through. Cells transparent to neutrons but opaque to helium must be blown from GE180 glass, which is a difficult material to work with. Each cell is therefore a slightly different size and shape, and contains a slightly different gas mixture and amount of rubidium. The polarizer cells were mounted in a forced-air oven held between 150–180°C, and were continuously polarized with $\sim 70\,\mathrm{W}$ laser power. Irradiation effects gave the cells a finite lifetime on the beam [Sharma et al., 2008], and so several different cells were used over the lifetime of the experiment.

2.2.3 Radiofrequency spin flipper

Because a neutron's total (squared) spin $\hat{S}^2 = \hbar^2 S(S+1) = 3\hbar^2/4$ cannot entirely come from its projection $\hat{S}_z^2 = (\hbar/2)^2$ on any axis, a full treatment of the neutron spin dynamics can't ignore spin components in the plane normal to the quantization axis. This can be done using a formal quantum-mechanical approach. But because the expectation values of the neutron's spin projections follow the same dynamics as a classical magnetic moment, it is sufficient and productive to imagine a classical "spin" precessing about the magnetic field

[10] If you send an unpolarized beam through two cells a, b with opacities $x_a \equiv n_a \ell_a \sigma P_a$ and $x_b \equiv n_b \ell_b \sigma P_b$, the final polarization is $\tanh(x_a + x_b)$, sensibly enough.

[11] Note that one could produce a net Rb nuclear polarization by using a narrower laser to deplete one of the "fine" F levels of the ground state; we do not.

direction at the Larmor frequency 3 kHz/G. If an additional field normal to the quantization axis oscillates at the Larmor frequency, a frame of reference exists where the precessing neutron spin sees only the oscillating field and precesses around that instead. If the neutron's interaction time in the oscillating field is half this precession time, the neutron spin will rotate to the opposite orientation in the holding field.

Our spin flipper is a ~ 30 cm solenoid whose axis lies parallel to the beam axis. The solenoid is enclosed in an aluminum can with beam windows thick enough to confine the rf[12] field. If the spin flipper has length $\delta \approx 30$ cm and sits a distance $L \approx 20$ m from the moderator, a neutron with velocity v will reach the spin flipper at a time of flight $t = L/v$ and dwell inside for a time $t\delta/L$. In order to completely flip neutrons at all times of flight, the amplitude of the rf field must vary as $1/t$. This was accomplished by storing a $1/t$ waveform in a programmable function generator and using that waveform as the envelope of a 30 kHz sine wave. This signal was restarted with each proton trigger, with a logic signal in the DAQ determining whether the signal went to the spin flipper itself or to an impedance-matched resistive load.

2.3 Liquid parahydrogen target

Hydrogen tends to depolarize neutrons: the cross section for spin-flip scattering is much larger than the cross section for spin-coherent scattering or capture. This hierarchy holds whether the hydrogen is bound up in a material like CH_2 or H_2O or is in the atomic H or molecular H_2 states. However, an unusual property of cold molecular hydrogen produces the cross section structure shown in figure 2.3, and makes it possible for neutrons to capture without first becoming depolarized.

At room temperature and below, the thermal energy of molecular hydrogen is partitioned among the translation degrees of freedom and the rotational states, which have energies $E_L = 15\,\mathrm{meV}\frac{L(L+1)}{2}$. The wavefunction for a rotor with angular quantum number L has parity $(-1)^L$. The total wavefunction for the two hydrogen nuclei must change sign under exchange, to obey Pauli symmetry. Therefore the two proton spins must be antisymmetric ($S = 0$, parahydrogen) for the even L states and symmetric ($S = 1$, orthohydrogen) for odd L. The small spin-orbit interaction between the two protons[13] gives an isolated orthohydrogen molecule with $L = 1$, $S = 1$ a surprisingly long lifetime. In liquid hydrogen the predominant mechanism for spontaneous ortho $\to$ para conversion is ortho-ortho scattering. However the rate for this process depends on the square of the ortho concentration; small concentrations of orthohydrogen are therefore quite stable. The partitioning of the even and odd rotational bands

[12] Traditionally, nuclear magnetic resonance is carried out at relatively high frequencies, and the oscillating field is referred to as "rf." We will conform to this even though our field oscillates at audio rather than radio frequencies.

[13] The interaction is the same as in the hyperfine transition of atomic hydrogen responsible for the astrophysical radio signal at 21 cm, but weaker because $\mu_\mathrm{e} \gg \mu_\mathrm{p}$.

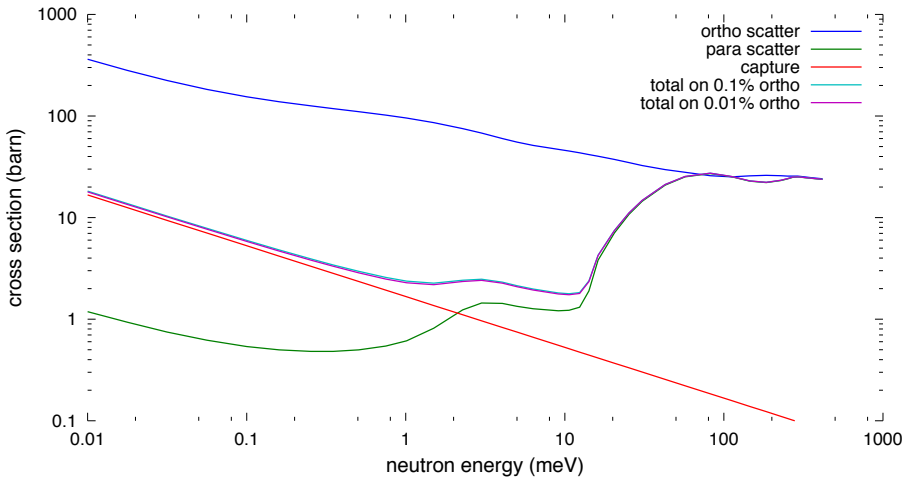


Figure 2.3: Cross sections for neutrons on liquid hydrogen at 19 K, extracted from the MCNP data libraries `sab2002` and `endf66a`. The para scattering cross section falls dramatically as the center-of-mass energy falls below the 15 meV required for para → ortho upscattering. The cross section curves for 0.1% and 0.01% orthohydrogen fraction cannot be distinguished at this scale. These cross sections agree only qualitatively with those given by the NDB for thermal neutrons: $\sigma_{\mathrm{inc}} = 80.26(6)$ b, $\sigma_{\mathrm{coh}} = 1.7568(10)$ b, and $\sigma_{\mathrm{abs}} = 0.3326(7)$ b.

causes hydrogen at low temperatures to behave like a mixture of two different fluids with slightly different heat capacities.[14]

At room temperature, both ortho- and parahydrogen have significant populations with several different L, and the predominant effect determining the 75–25 ortho-para equilibrium ratio for "normal" hydrogen is the fact that there are three triplet spin orientations and one singlet. At 20 K, the equilibrium concentration of ortho is $3 \cdot 3 \cdot \exp \frac{-15\,\mathrm{meV}}{kT} \approx 10^{-3}$.

A neutron interacting with an $L = 0$ parahydrogen molecule therefore has a different set of allowed final states than a neutron interacting with an isolated H or an excited H_2. Because the overall nuclear spin is conserved, the neutron spin may flip only if the H_2 spin changes from singlet to triplet. But Pauli symmetry forbids this transition without the 15 meV required for the transition $L = 0 \to 1$. For neutrons below this energy spin-flip scattering is forbidden, and coherent scattering and capture are roughly equally probable. The cross sections for the three processes are shown in figure 2.3.

We have already seen that the neutron beam on FP12 has the most intensity around 3 meV. In liquid hydrogen, with mass density $\rho = 70\,\mathrm{kg/m^3}$, neutrons with this energy have a mean free path of $(n\sigma)^{-1} \simeq 12\,\mathrm{cm}$. Production of a parahydrogen volume $\sim (30\,\mathrm{cm})^3$, however, presents several technical challenges. Coherent s-wave scattering will fill the entire volume of the target with a diffuse neutron gas, with a spectrum slightly cooler than the spectrum of the direct beam. Those scattered neutrons will produce capture γs on any material they see, including whatever cryostat contains the hydrogen. This limits the type and thickness of materials that can be used to build the cryostat, and suggests that any refrigerators should also sit far from the main volume. The long time required for normal hydrogen to spontaneously convert to para suggests that the target should contain some magnetic catalyst, which should sit outside the main volume for the same reasons. On the other hand, hydrogen is liquid only over a narrow temperature range (13–20 K at 1 atm), and conducts heat poorly; weak thermal coupling to such a system presents a risk of localized freezing, boiling, or both. Furthermore $\sim$ 16 L of liquid hydrogen, if permitted to vaporize, would be in rough stoichiometric equilibrium with the volume of oxygen in the experimental cave and present a serious safety concern. This combination of design constraints led to the relatively complex target system discussed below.

2.3.1 The liquid hydrogen cryogenic systems

Because of the safety concerns associated with this quantity of liquid hydrogen, the cryostat incorporates "triple containment." The target vessel was a jointless welded aluminum cylinder. The aluminum vessel has a small neutron interaction cross section and good thermal conductivity, helping to keep the temperature uniform within the bulk of the target. However aluminum's thermal conduc-

[14] In fact the original line of evidence went exactly in the opposite way from its presentation here. When liquid hydrogen was first produced in the 1920s, heat capacity measurements revealed the division into ortho and para. The demonstration that the H_2 $L = 0$ state is a spin singlet was taken as evidence that protons obey Fermi-Dirac statistics. See Farkas [1935].

tivity makes it unacceptable for the infrastructure connecting the vessel to the room-temperature world; these pieces were fabricated from stainless steel. Connections between the aluminum vessel and the stainless steel plumbing were made using metal-to-metal impact welds. This preference for welds permitted construction of a cryostat with only two cold conflat flanges, both on narrow sections of pipe, far from the main volume, and between like species of metal.

The vacuum chamber containing the target vessel was machined from two large single ingots of aluminum: a rectangular ingot for the vertical section of the cryostat and a cylindrical section for the sleeve surrounding the main target volume. Again this reduces the number of joints required. Furthermore every welded joint, and each of the O-ring seals on the upstream and downstream windows, contains a channel through which helium gas flows. This "triple containment" — hydrogen, vacuum, helium, air — permits exquisitely sensitive leak detection in the target. A residual gas analyzer (RGA) on the target vacuum monitors the partial pressures of hydrogen, helium, and more mundane atmospheric gases, providing some diagnostic information about the location of any small leaks.

Hydrogen enters the target via the gas handling system (GHS) shown in figure 2.4. Gas cylinders of commercially pure hydrogen were stored on outside the experiment hall on a roofed, unenclosed concrete pad. Each cylinder may be separately isolated from the shielded line leading indoors. The indoor components of the system were enclosed in a cabinet with a chimney leading outside to the roof. In the cabinet the hydrogen passed through a second regulator, PR105, and a flow meter. (The palladium diffusion purifier, PRFR, present in the figure was excluded from the final design; this change eliminated the need for any high-pressure sections of the GHS during normal operation. Also the nitrogen-cooled ortho-para converter (OPC) was replaced by a helium-cooled OPC inside the main cryostat as discussed below.) After the flow meter the hydrogen passed through an activated charcoal filter submerged in liquid nitrogen; the cool, dry hydrogen then left the enclosure and entered the cryostat. This straightforward system acquired the complexity suggested by figure 2.4 because each component was designed to be isolated by valves from its neighbors. Each isolatable section then had its own pressure gauge (mechanical, electrical, or both), its own connection to the GHS vacuum, and its own connection via a relief valve to the cryostat's chimney.[15]

Hydrogen entered the cryostat via the 2 inch stainless steel "vent tube," also connected to the relief system, visible in figure 2.5. During the second and third 2006 fills the hydrogen entered the cryostat via an ortho-para converter, cooled by liquid helium and heated to prevent hydrogen from freezing inside. Hydrogen vapor then fills the vent line, target vessel, and the "fill line" leading to the two cryocoolers. Hydrogen which condenses on the upper cold head, at the thermometer T3, could only flow vertically to the OPC sitting on the lower cold head, at T2.

[15] The GHS and cryostat had separate chimneys so that, during a target boiloff, high pressure hydrogen would not diffuse back into the GHS cabinet.

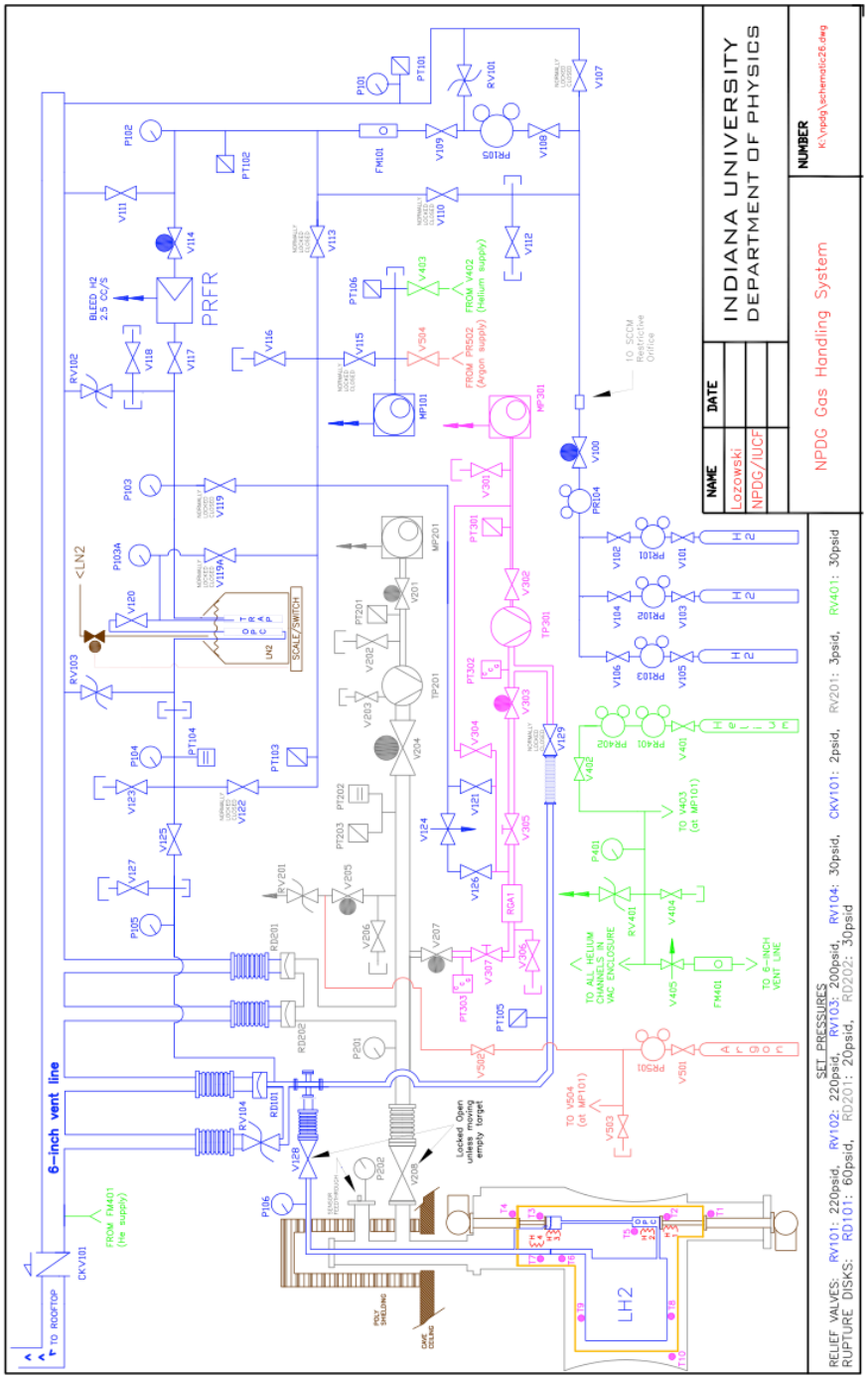
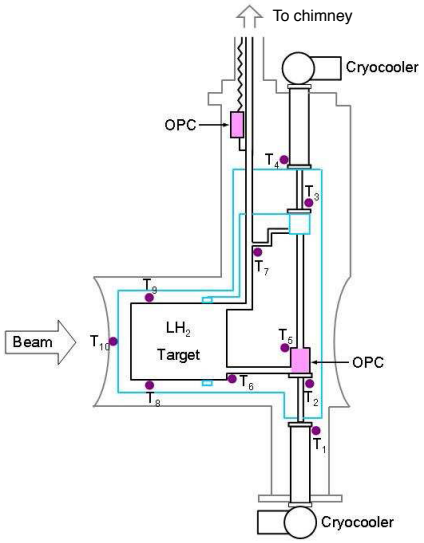


Figure 2.4: The $\vec{n} + p \rightarrow d + \gamma$ hydrogen target system. Differences between this 2004 diagram and the system installed in 2006 are discussed in the text; however, later diagrams do not show the entire apparatus on one page.



Grey, outside of vacuum chamber; blue, copper heat shield and copper braid connecting upper refrigerator to target vessel; pink, chambers containing ortho-para catalyst; solid black lines indicate plumbing. Thermometers T1 and T4 monitor the two 80 K cryocooler warm heads, T2 and T3 the two 4 K cold heads. Thermometer T6 monitors the inlet from the fill line to the main vessel; T8 and T9 the upstream end, bottom and top; T7 the vent line near the outlet to the upper cryocooler. The upstream thermometer T10 was outside the heat shield (which, during data collection, was operated with no upstream window). The thermometer T5 wound up less useful for monitoring the lower cryocooler and ortho-para converter than T2. Not shown: heaters on the two cold heads, and on the vent line near T7. Not to scale.

Figure 2.5: Refrigerators and temperature sensors in the LH_2 cryostat

2.3.2 Operation

During and after the transfer of hydrogen to the target, the only data available were the temperatures from the thermometers shown in figure 2.5 and the pressure in the vent line. To diagnose the internal state of the target from this information, it proved useful to follow the state in the P-T plane, as in figure 2.6 and following. The solid line shows the H_2 liquid-vapor equilibrium. Hydrogen at temperatures and pressures to the left of the line will tend to condense, while to the right it boils; the heat and pressure changes due to either of these spontaneous processes will tend to push the system back towards equilibrium. To see the usefulness of this approach, we show some behaviors of the target during the second fill, beginning 15 August 2006.

Figure 2.6 shows the temperatures and pressures in the target during the initial introduction of hydrogen. Initially the target is cold and evacuated, and the gas handling system (including the target volume) has been flushed with helium. Hydrogen enters the system through the upper ortho-para converter, cooled by circulating liquid helium. As the pressure in the target rises, only the two refrigerators remain cold enough for hydrogen to condense. When liquid reaches the end of the stainless steel fill line at the upstream bottom end of the target, the temperature at T6 rapidly jumps to the liquid-vapor equilibrium line; as the flowing liquid reaches the upstream end of the target, the temperature at T8 begins to parallel the equilibrium line as well. As vessel fills, however, the flow of cold liquid from T6 to T8 slows and T8 becomes better connected by

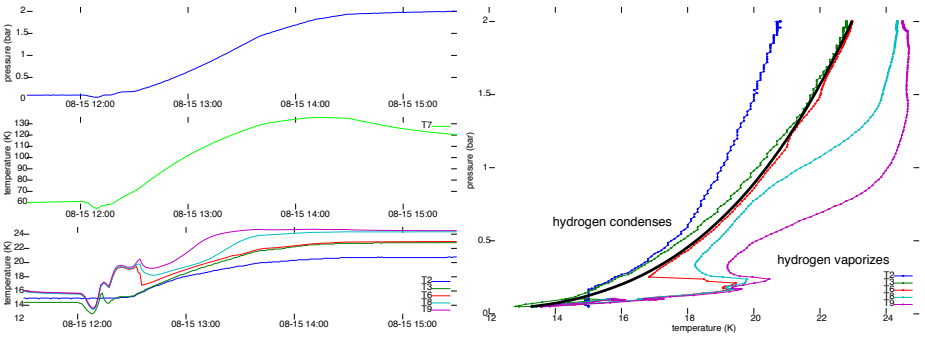


Figure 2.6: Temperatures and pressures in the target during August 2006 fill. Left: pressure (top) and temperatures (bottom) in the target for four hours on 15 August, labeled as in figure 2.5. Right: same data (except T7, which does not fall below 60 K) in the P-T plane. Points at 60 s intervals; solid line indicates liquid-vapor equilibrium. Features interpreted in text.

heat conduction through the aluminum to T9, warming again.

The target remained in this state — hydrogen flowing in, liquefying in both refrigerators, flowing into the vessel, and boiling off there — for two days. At this point the temperature at T7 fell to the liquid-vapor equilibrium, indicating that liquid had filled the main vessel and moved into the elbow of the vent tube. The fill continued from this point for most of another day: liquid hydrogen has a fairly large density variation with temperature, and as the target vessel cooled and its contents contracted the liquid level would occasionally fall below the elbow again.

Following the conclusion of the fill and isolation of the target from the gas handling system, the vent line heater was set to maintain T7 at a constant temperature, while the heaters on the two cryocooler cold heads were set at 16 K to prevent freezing. This set of parameters permitted two metastable sets of flows, both of which appear in figure 2.7: a steady flow, and a set of coupled temperature and pressure oscillations with a period of five or ten minutes.

The design of the hydrogen target had anticipated steady-state operation at 17 K and a pressure greater than about 1 bar. The operating temperature was chosen to set the orthohydrogen fraction; the design pressure was high enough that the target bulk would be very far from evaporation. However, when operated at the design temperature and pressure the target continued to oscillate. The set of oscillations shown in figure 2.8 suggests a target that is completely full, with fluid flowing in spurts. The temperature at T7, in the vent line, is well into the liquid side of the phase diagram. As the vent line is heated its temperature and pressure rise together, with an "elbow" when a phase change begins in the liquid there. Eventually the pressure rises enough to push fluid through the fill line to the refrigerators, which see a burst of heat; cool liquid flows up into the vent line and cools T7 again; very cold liquid from the lower refrigerator modestly changes the temperature T6 at the inlet to the

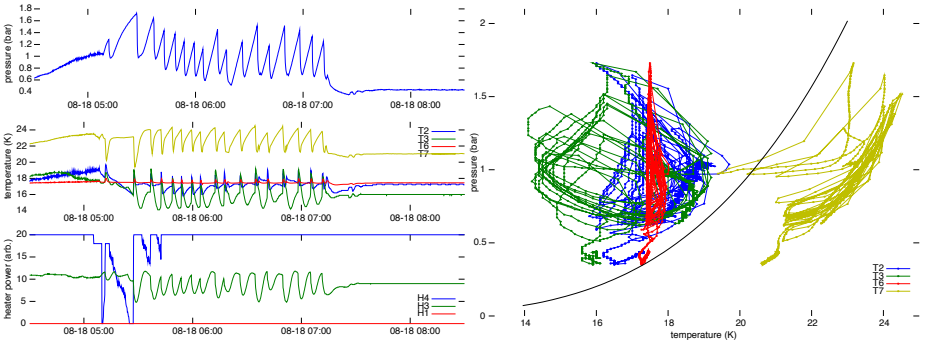


Figure 2.7: Oscillations in the hydrogen target. Left, top to bottom: pressure, temperatures, and heater power over four hours on 18 August. Heater H4 sits near T7 in the vent line; H3 near T3 on the upper cryocooler; H1 near T2 on the lower cryocooler. Right: same data in the *P-T* plane. Points at 12 s intervals. Cycles in T7, where heat enters the system, go counterclockwise; cycles in T3, where heat leaves the system, go clockwise. Fast part of cycle is ~ 30 s of fluid movement. Note ortho-para conversion heat on T2 after each flow. The oscillations end with T6 near the equilibrium curve, suggesting a surface within the target vessel.

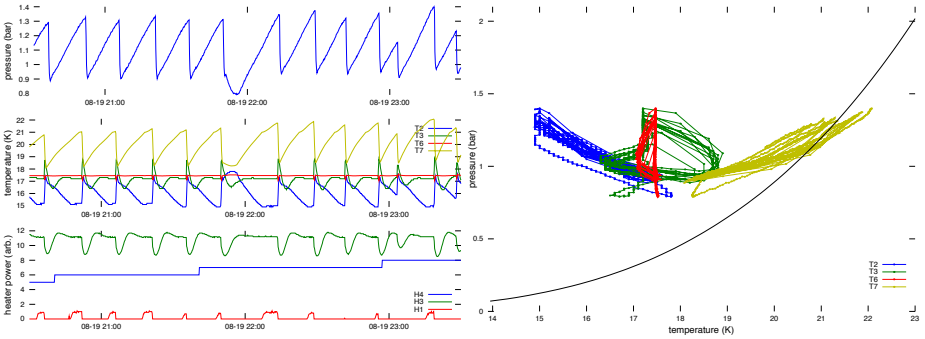


Figure 2.8: Cooler oscillations. Like figure 2.7, but 18 h later. Note relative lack of ortho-para conversion heating at T2, compensated by the heater H1, except during the "burp" near 22:00. Also note elbow in oscillations of T7, suggesting the part of the vent line is warmer than, but in thermal contact with, liquid.

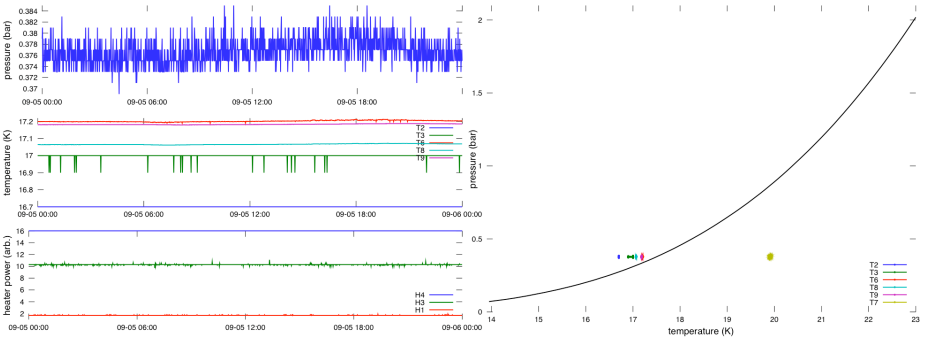


Figure 2.9: Stable target operation, 5 September 2006.

target bulk. For the pressure in the target to remain stable, as in figure 2.9, the vent line pressure had to be much lower than designed, only barely above the vapor pressure in the target bulk.

To measure the ortho-para ratio in the full target, the transmission of the neutron beam was compared to the transmission through the empty target. With the volume and density of the liquid hydrogen known, the transmission at each neutron wavelength gave a separate estimate of the orthohydrogen concentration. With hydrogen circulating over our ortho-para conversion catalyst, the delay from the start of a fill to the beginning of production data was about ten days. The process of extracting the ortho-para ratio from neutron transmission is described in Barron-Palos et al. [2007].

2.4 Current-mode CsI detectors

The photon detectors were an array of CsI(Tl) crystal scintillators, arranged as shown into four rings of twelve. Gamma rays in the crystal lose energy primarily by Compton scattering, which creates defects in the electronic lattice; relaxation of the lattice back to its ground state produces visible photons to which the crystal is largely transparent. [This process, "scintillation," is the subject of a rich literature to which we do no justice here. See e.g. Knoll, 2000] This scintillation light is collected by a vacuum photodiode, with the resulting photocurrent sent via a low-noise room-temperature preamplifier to the DAQ. A set of digitally adjustable analog amplifiers permitted gain matching within each ring, prior to digitizing the signals using the sum-and-difference scheme discussed in chapter 3. Details of the construction and operation of the detectors are provided by Gericke et al. [2005].

2.5 Systematic effects

The ultimate goal of the $\vec{\mathrm{n}} + \mathrm{p} \to \mathrm{d} + \gamma$ experiment is a measurement of the asymmetry A_γ with uncertainty $\sim 10^{-8}$, about 20% of the expected size from the DDH "best value." If the dominant contribution to the uncertainty comes from shot noise, Poisson statistics requires the detection of at least 10^{16} photons. The LANSCE run of the experiment took 750 h data in several million 400 ms spin sequences; an uncertainty $\sim 10^{-4}$ in each sequence, corresponding to $\sim 10^8$ photons, gave the total final uncertainty $\sim 2 \times 10^{-7}$. Doing this averaging believably requires a careful catalogue of systematic effects, quantified by tests showing they contribute below the goal uncertainty.

2.5.1 False asymmetries

The most obvious concern is an instrumental artifact coupling the response of the detector to the neutron spin state. For instance, the leakage rf field from the spin flipper might change the response of the γ detectors between unflipped and flipped pulses. Such an effect would be indistinguishable from a

spin-correlated effect. A magnetic field oscillating at 30 kHz has a very small skin depth in metal, however; concerns about leakage set a minimum thickness for the aluminum windows on the spin flipper, to 2 mm. Care was taken to build detectors insensitive to dc and rf magnetic fields, as well.

The use of conjugate pairs of detectors and spin reversals to determine the asymmetry removes the first-order sensitivities to the location and amplitude of the beam. (In the notation of chapter 3, these fluctuations affect the "gain" and "beam" asymmetries A_{gain} and A_{beam}.) Furthermore use of the eight-step spin sequence $\uparrow\downarrow\downarrow\uparrow\downarrow\uparrow\uparrow\downarrow$ decouples A_{beam} from the first and second derivatives of the beam intensity. Note, however, that the first-order cancellation of the sensitivity to beam position occurs only if the beam position is independent of the neutron spin. Spin-correlated beam steering must be dealt with very carefully.

With our apparatus the spins and momenta of the proton and deuteron are inaccessible, as is the photon helicity. Any correlation in the reaction must therefore appear in the coordinate system defined by $\vec{\sigma}_{\mathrm{n}}, \vec{k}_{\mathrm{n}}, \vec{k}_{\gamma}$. The neutron spin $\vec{\sigma}_{\mathrm{n}}$ is quantized along the magnetic field $\vec{B}$, which is approximately vertical; the neutron wavevector $\vec{k}_{\mathrm{n}}$ is defined by the acceptance and alignment of the guide and is approximately horizontal.[16] We define a right-handed coordinate system with $\vec{y}, \vec{z}, \vec{x}$ (up, downstream, left) in the direction of $\vec{\sigma}_{\mathrm{n}}, \vec{k}_{\mathrm{n}}, (\vec{\sigma}_{\mathrm{n}} \times \vec{k}_{\mathrm{n}})$, respectively. If we decompose the photon distribution into a monopole and three orthogonal dipoles, we may construct up-down, forward-backward, and left-right correlations with the photon wavevector $\vec{k}_{\gamma}$,

$$\frac{d\Gamma}{d\Omega} \propto 1 + A_{\mathrm{UD}}\ \vec{\sigma}_{\mathrm{n}} \cdot \vec{k}_{\gamma} + A_{\mathrm{FB}}\ \vec{k}_{\mathrm{n}} \cdot \vec{k}_{\gamma} + A_{\mathrm{LR}}\ (\vec{\sigma}_{\mathrm{n}} \times \vec{k}_{\mathrm{n}}) \cdot \vec{k}_{\gamma}. \tag{2.6}$$

If some scattering process changes the neutron distribution in space, the scattered momentum $\vec{k}'_{\mathrm{n}}$ offers an extra degree of freedom. The capture distribution will shift by some small displacement $\vec{\delta} \propto \vec{k}'_{\mathrm{n}}$, and more energy will be deposited in the detectors on that side. This gives us the "solid angle" or "steering" asymmetries

$$\left(\frac{d\Gamma}{d\Omega}\right)_{\mathrm{s}} \propto 1 + A'_{\mathrm{UD}}\ \vec{\sigma}_{\mathrm{n}} \cdot \vec{\delta} + A'_{\mathrm{FB}}\ \vec{k}_{\mathrm{n}} \cdot \vec{\delta} + A'_{\mathrm{LR}}\ (\vec{\sigma}_{\mathrm{n}} \times \vec{k}_{\mathrm{n}}) \cdot \vec{\delta}. \tag{2.7}$$

The A' have the same behavior under parity conjugation as the A, but opposite under time reversal.

The front-back solid angle asymmetry A'_{FB} is quite large because there are more neutrons in the upstream end of the target. The momentum correlation A_{FB}, due to the velocity $v \approx 10^{-6}c$ between the capture rest frame and the detector, is also large by our standards.[17] However, neither of these couples to

[16] Note that the neutrons fall: the vertical component of their velocity changes at the rate $g \approx 10^{-5}\,\mathrm{m/ms^2}$. For a cold neutron traveling 20 m in 20 ms, the change in angle with the horizontal is small, but not negligible, compared with the critical angle for reflection from the guide.

[17] This relativistic effect doesn't produce an asymmetry in the forward-backward count rate, but changes the energy deposited by forward and backward photons in each detector.

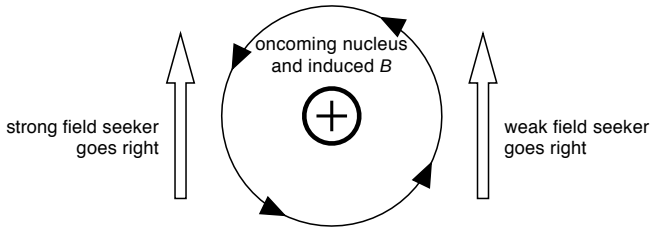


Figure 2.10: Mott-Schwinger scattering

the neutron spin; they therefore do not contribute an asymmetry over a spin sequence. To the extent that the detector rings are not normal to $\vec{k}_{\mathrm{n}}$, the A_{FB} contribute to the spin-independent difference A_{gain} between the efficiencies of a pair of detectors.

A very serious systematic concern is the possibility of Stern-Gerlach steering, where the neutrons feel a force $F = -\nabla(\vec{\mu}\cdot\vec{B})$. The neutron's magnetic moment $\vec{\mu}$ is quantized along the direction of $\vec{B}$. In a magnetic field where the change $(\vec{v}\cdot\nabla)\vec{B}$ in the neutron's local magnetic field is slow relative to the Larmor precession frequency $\omega_L = \gamma_{\mathrm{n}} B$ [the "adiabatic condition," see e.g. Byrne, 1994], the direction of $\vec{\mu}$ follows $\vec{B}$ without depolarization. Stern-Gerlach steering then becomes

$$F = -\nabla(\vec{\mu}\cdot\vec{B}) = \pm|\mu|\nabla|B|. \tag{2.8}$$

and segregates the neutrons into "strong-field seekers" and "weak-field seekers." The neutron's magnetic moment is proportional to its spin, so any gradient in the field would produce a spin-correlated steering contributing to the solid angle asymmetries A'. If the center of the beam shifts vertically by some distance $\delta \ll r$, where $r \approx 0.5\,\mathrm{m}$ is the radius of a detector ring, the solid angle asymmetry is

$$A'_{\mathrm{UD}} = \frac{(r-\delta)^{-2} - (r+\delta)^{-2}}{(r-\delta)^{-2} + (r+\delta)^{-2}} \approx \frac{2\delta}{r}. \tag{2.9}$$

A steering of a few nanometers is enough to entirely swamp our parity-violating signal. Neutrons travel from the spin flipper to the target in $\sim 1\,\mathrm{ms}$; the vertical field gradient over this region must be smaller than $\sim 5\,\mathrm{mG/cm}$.

The left-right solid angle asymmetry A'_{LR} has an electromagnetic and a nuclear contribution. The electromagnetic effect was first suggested by Schwinger [1946, 1948], as an extension to nuclear systems of the method of Mott [1929, 1932] for producing and analyzing polarized electron beams. In the rest frame of the incident neutron, the (screened) charge of the oncoming proton produces a magnetic field. A neutron with $\vec{\mu}$ pointing up, in the field of figure 2.10, is a strong field seeker on the left side and a weak field seeker on the right. Either scenario produces a spin-dependent, parity-allowed momentum transfer sending the neutron off to the right.[18] The nuclear spin-orbit coupling also contributes

[18] An early Mott scattering experiment [Cox et al., 1928] reported a pesky systematic error that went away when, among other changes, the electron source was switched from a β^-

a left-right scatter that couples to A'_{LR}, due to parity-allowed S-P wave mixing. Both of these effects are small for low-energy neutrons.

Cavaignac et al. [1977] searched for a left-right asymmetry in their $\vec{\mathrm{n}} + \mathrm{p} \to \mathrm{d}+\gamma$ experiment and found an upper limit $A_{\mathrm{LR}}+A'_{\mathrm{LR}} = 3\times10^{-7}$; they note that the time-odd operator $(\vec{\sigma}\times\vec{k}_n)\cdot\vec{k}_\gamma$ cannot contribute to a CP-even Hamiltonian. Csótó et al. [1997] find that this term generates a left-right asymmetry $\sim 10^{-8}$ in several nuclear models, but do not address the question of CP conservation directly. The question of left-right asymmetries has recently received a more complete treatment [Gericke, Bowman, and Johnson, 2008].

Apart from the parity-violating false asymmetries deferred until the next section, we have exhausted the freedoms of (2.6) and (2.7). Those anisotropies in the density distribution of captures that do not vary with spin cannot contribute to the parity violation signal.[19] Our cylindrical detector is sensitive to left-right and up-down asymmmetries separately, but can distinguish them only to the extent that the alignment between the detector and the magnetic field is known.

2.5.2 Backgrounds and background asymmetries

Neutrons may produce signals in the photon detectors in several different ways. Thus far we have mostly discussed photons from $\vec{\mathrm{n}}+\mathrm{p} \to \mathrm{d}+\gamma$. However, nearly all neutron captures are accompanied by a cascade of photons — the exceptions being captures on the light nuclei ^{3}He and ^{6}Li, which fragment into isotopes of H and He without bound excitations. Many neutron capture products are unstable against β decay; these "activated" materials will emit electrons and photons for some time after exposure to neutrons. Neutrons scatter from every window and air gap along the beamline, filling the experiment cave with a diffuse neutron gas. Every material in the cave, but especially those along the beam, may thus make short- and long-lived contributions to the photon signal. "Prompt" backgrounds, with lifetimes comparable to our time resolution 0.4 ms, cannot be distinguished from the $\vec{\mathrm{n}} + \mathrm{p} \to \mathrm{d}+\gamma$ signal. Some information about these can be obtained from target-empty runs, but scattering in the target changes the background capture distribution. "Delayed" backgrounds with time constants much longer than the 400 ms duration of a spin sequence will produce a constant background over any sequence. The intermediate cases require further examination.

Photon backgrounds may affect our asymmetry signal in two ways:

1. Spin-independent backgrounds add statistical noise to the photon signal and increase the denominator of the asymmetry. Both effects reduce our sensitivity.

---

emitter to a thermal source. The significance of the effect was not realized until much later [Grodzins, 1959]. Franklin [2001] calls the affair the "nondiscovery of parity nonconservation" and analyzes the Cox et al. experiment in some detail.

[19] "Breathing modes," where symmetric spin-correlated effects change the effective capture cross section or solid angle without favoring one detector over another, enter the same way as a "beam asymmetry" A_{beam} in chapter 3.

2. A parity-violating asymmetry in the background cannot be distinguished from an asymmetry in $\vec{\mathrm{n}} + \mathrm{p} \to \mathrm{d} + \gamma$.

Parity-violating background asymmetries are particularly insidious. In general they are understood too poorly to be predicted, and measurement would require an effort comparable to the $\vec{\mathrm{n}} + \mathrm{p} \to \mathrm{d} + \gamma$ measurement itself. For example, chlorine has capture cross section 33.5 b and a parity violating asymmetry -20 ppm, both a thousand times larger than the same parameters for hydrogen; contamination of the target volume with one part per million chlorine, then, would be enough to mask the hydrogen asymmetry. Components of the beamline downstream of the spin flipper must therefore be chosen quite carefully. Direct measurements of these prompt asymmetries occupied the experiment in 2004 and 2005 and are discussed in the dissertations of Gericke [2004] and Dabaghyan [2007].

In addition to prompt asymmetries like chlorine's, delayed backgrounds may contribute asymmetries as well. Polarized neutron capture creates a population of polarized nuclei, which may have directional asymmetries in their subsequent β and γ decays. However the pulse-by-pulse spin reversal $\uparrow\downarrow\downarrow\uparrow\downarrow\uparrow\uparrow\downarrow$ dilutes this effect as well. If neutrons with average polarization $\langle P_\mathrm{n}\rangle$ capture on an unpolarized target and form a population of nuclei with spin J, the maximum possible polarization for this population is $\langle P_\mathrm{n}\rangle/2J$. If the time constant for the spin to relax to the magnetization of the surrounding lattice is T_1, and the radioactive decay time is τ, the fraction of these nuclei that decay before relaxing is $T_1/(\tau + T_1)$. Radiation from the population produced n pulses ago contributes with weight $e^{-n\Delta t/\tau}$, where $\Delta t = 50$ ms is the pulse interval. The polarization of these subgroups must be weighted by the average ratio ϵ_n of the current spin state to the spin state of their formation,

$$\begin{array}{rcccccccc} n: & 1 & 2 & 3 & 4 & 5 & 6 & 7 & 8 \\ \epsilon_n: & -\frac{1}{2} & 0 & -\frac{1}{2} & -1 & \frac{1}{2} & 0 & \frac{1}{2} & 1 \end{array} \tag{2.10}$$

(That is, the previous pulse has a different spin three times out of four, the spin four pulses back is always reversed, and so on.) The effect of this weighting, neglecting beam fluctuations, is that the delayed background at early in a pulse comes from nuclei with a polarization slightly reversed from the neutron polarization,

$$P_\mathrm{nuc} \lesssim \frac{-\langle P_\mathrm{n}\rangle}{2J}\ \frac{T_1 \Delta t}{\tau^2}, \tag{2.11}$$

but the equilibrium polarization of the long-lived background is restored at the end of the neutron pulse. The largest polarizable contribution to our delayed background comes from activated aluminum in the cryostat. Natural aluminum at 20 K has a spin-lattice relaxation time $T_1 = 80$ ms [Redfield, 1956]. If we assume this T_1 for a lone ^{28}Al nucleus in a lattice of ^{27}Al, we find an upper limit $P_\mathrm{nuc} \approx 4 \times 10^{-8}$ for the polarization of ^{28}Al at the time of β decay. This is smaller than the goal uncertainty if the parity-violating photon asymmetry in the decay to ^{28}Si is smaller than 10%.

Chapter 3

Analysis methods

The hydrogen parity-violation data have been analyzed as described by Gericke [2004] and Dabaghyan [2007]. This analysis [Gericke et al., 2009] obtained null results for the up-down and left-right asymmetries,

$$\begin{aligned} A_{\mathrm{UD}} &= (-1.1 \pm 2.1_{\mathrm{stat.}} \pm 0.2_{\mathrm{syst.}}) \times 10^{-7}, \\ A_{\mathrm{LR}} &= (-1.9 \pm 2.0_{\mathrm{stat.}} \pm 0.2_{\mathrm{syst.}}) \times 10^{-7}. \end{aligned} \tag{3.1}$$

This precision is comparable to the null result $A_{\mathrm{UD}} = (0.6 \pm 2.1) \times 10^{-7}$ reported by Cavaignac, Vignon, and Wilson [1977].

This chapter outlines a complementary analysis, and considers the relative merits of several different asymmetry computation algorithms. We describe in some detail the processing of the photon detector signals by the data acquisition system, their reconstruction for analysis, and the ways that different systematic effects manifest in the data. Each construction for the physics asymmetry is sensitive to systematic errors in a different way. By computing multiple estimators for the physics asymmetry and comparing their expected and actual relationships to each other, we can develop a robust set of diagnostic tools sensitive to many different computational and systematic errors.

3.1 Components of the data stream

The structure of the $\vec{\mathrm{n}} + \mathrm{p} \rightarrow \mathrm{d} + \gamma$ data stream follows in a straightforward way from the construction of the data acquisition system (DAQ), shown in Figure 3.1 and described in more detail below.

As it approaches the spallation target, the proton pulse passes through an inductive coil which measures the charge delivered. VME1 receives a prompt trigger T_0 at the time of this pulse. The Lujan facility also uses the proton signal to drive an amplitude-to-frequency converter at a rate 500 Hz/µA. A scaler on VME1 counts these pulses for 45 ms, providing an approximate record of the beam current. VME1 also duplicates the T_0 trigger and sends it into the cave to VME2 and VME3.

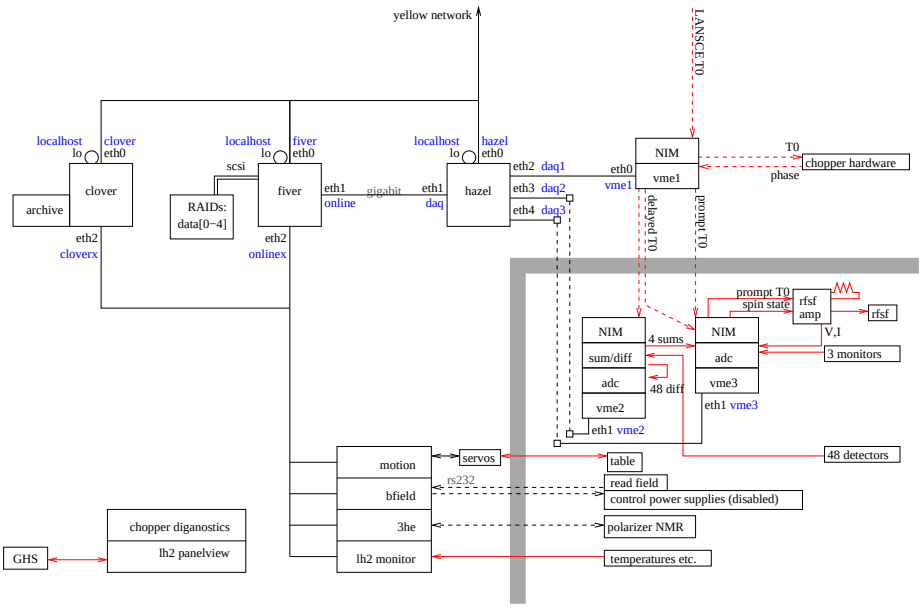


Figure 3.1: The $\vec{\mathrm{n}} + \mathrm{p} \rightarrow \mathrm{d} + \gamma$ data acquisition system. Commodity computers clover, fiver, hazel sat outside the cave. Computers delivered with various subsystems (detector table motion, B field, etc.) communicated over private ethernet, both for administrative reasons and, for the VME machines, to improve throughput. During parity-violation measurements only optical fiber connections (dashed lines) passed through the cave wall. See text for the interaction of the VMEs with neutron and photon detectors. At the end of a run data were copied both to the RAID on fiver, for immediate analysis, and to the removable archive on clover for secondary backup.

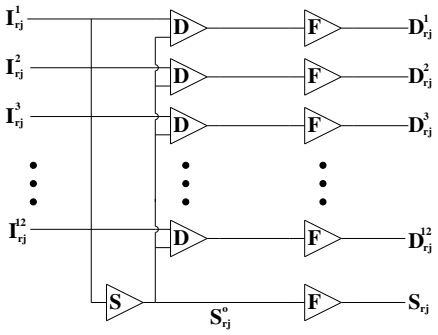


Figure 3.2: Sum and difference amplifiers [from Gericke, 2004]. Here I^d_{rj} is the preamplified photocurrent from ring r, detector d, at time j; S, summing amplifier with gain 1/12; D, difference amplifiers with gain 10; F, Bessel filters with gain 3. The sum and difference signals S_{rj} and D^d_{rj} are digitized as described in the text.

Crates 2 and 3 contain 12 bit ADCs, sampled at 50 kHz and 62.5 kHz respectively. Prior to digitization, the detector photocurrents pass through the analog sum-and-difference amplifiers shown in figure 3.2. The ADCs in VME2 connect to the forty-eight difference signals from the detector array. Those in VME3 measure the sum signals, the neutron beam monitor currents, and the voltage and current sent to the spin flipper. VME3 also contains the spin sequence generator, which produces logic pulses determining whether current from the spin flipper's power supply passes through the spin flipper or through its dummy load.

We have seen that, to flip neutron spin efficiently in a 10 G holding field, the field inside the spin flipper must oscillate at ~ 30 kHz. To avoid Nyquist aliasing, the DAQ must store the spin flipper's current and voltage signals at full 62.5 kHz resolution. However, the distribution in neutron emission times from the moderator limits the possible time-of-flight resolution for the neutron beam to $\sim 100\,\mu$s. With no cause to store the neutron signals at full resolution, we compress our 40 ms data window into one hundred time bins by summing consecutive analog-to-digital converter (ADC) readings. Each sum of twenty (VME2) or twenty-five (VME3) 12 bit ADC readings fits comfortably in a 32 bit integer.

We note that the analog sum and difference amplifiers and the difference ADCs sit in crate 2, isolated from the spin sequence production and measurement in crate 3.

During data taking, VME1 releases its T_0 trigger from the facility to a 10 ms delay generator, which sends the delayed trigger in turn to VME2 and VME3. When triggered, the two cave crates record ADC data as described above for 40 ms. During the 10 ms window before the next pulse arrives, the data transfers from the ADC's memory to the VME's disk. The system saves each data block with a header containing

- the "flag" value 0xabcd0123 (useful for debugging the output)
- the clock time
- the pulse number
- whether the ADC readout took place entirely between T_0 triggers
- whether exactly one previous pulse successfully went to the disk
- some status bits
- another flag.

An $\vec{\mathrm{n}} + \mathrm{p} \rightarrow \mathrm{d} + \gamma$ data file contains simply a sequence of these headers and their corresponding blocks of (integer) ADC data.

3.2 Computation of raw asymmetries

We assume the detector signals are linear; that is, the ith detector has a spin-independent gain G_i such that for a polarized neutron current $N_0^{\uparrow\downarrow}$, the photocurrent is

$$\begin{aligned} N_i^{\uparrow} &= G_i N_0^{\uparrow}(1 + A_i^{\gamma}) + P_i \\ N_i^{\downarrow} &= G_i N_0^{\downarrow}(1 - A_i^{\gamma}) + P_i. \end{aligned} \tag{3.2}$$

The pedestal P_i is the current recorded in the absence of any neutron signal, including biases in the detector electronics and backgrounds from photon emitters with lifetimes long relative to the 50 ms pulse interval. Here A_i^{γ} is the combination of left-right and up-down asymmetries permitted by the angle between the neutron spin direction and the photon momentum accepted by the detector, and the gain G_i includes effects of geometrical acceptance and detection efficiency. Both G_i and A_i^{γ} depend on the detector position relative to the capture distribution within the target. Here we consider what information we can extract from measurements $N_i^{\uparrow\downarrow}$ and corresponding measurements $N_j^{\uparrow\downarrow}$ on a parity-conjugate detector.

3.2.1 Systematic effects with negligible pedestals

First we consider the signal-dominated regime, where we may neglect the pedestal $P_i \ll N_i$. In addition to the physics asymmetry A^{γ}, we might like to learn about the beam asymmetry,

$$A_{\text{beam}} = \frac{N_0^{\uparrow} - N_0^{\downarrow}}{N_0^{\uparrow} + N_0^{\downarrow}} = \frac{\Delta N}{\Sigma N}, \tag{3.3}$$

and the gain asymmetry,

$$A_{\text{gain}} = \frac{G_i - G_j}{G_i + G_j} = \frac{\Delta G}{\Sigma G}. \tag{3.4}$$

Define the sums and differences between signals in a detector pair,

$$\begin{aligned} N_+^{\uparrow\downarrow} &= N_i^{\uparrow\downarrow} + N_j^{\uparrow\downarrow} = N_0^{\uparrow\downarrow}\left(\Sigma G \pm A^{\gamma}\Delta G\right) \\ N_-^{\uparrow\downarrow} &= N_i^{\uparrow\downarrow} - N_j^{\uparrow\downarrow} = N_0^{\uparrow\downarrow}\left(\Delta G \pm A^{\gamma}\Sigma G\right). \end{aligned} \tag{3.5}$$

If we define the arithmetic asymmetry for a spin state,

$$A_{\text{arith}}^{\uparrow\downarrow} = \frac{N_-^{\uparrow\downarrow}}{N_+^{\uparrow\downarrow}} = \frac{A_{\text{gain}} \pm A^{\gamma}}{1 \pm A_{\text{gain}}A^{\gamma}}, \tag{3.6}$$

we can approximately access the gain and physics asymmetries via

$$\begin{aligned} A_{\text{arith}}^{+} &= \frac{A_{\text{arith}}^{\uparrow} + A_{\text{arith}}^{\downarrow}}{2} = A_{\text{gain}}\frac{1 - (A^{\gamma})^2}{1 - (A_{\text{gain}}A^{\gamma})^2} \\ A_{\text{arith}}^{-} &= \frac{A_{\text{arith}}^{\uparrow} - A_{\text{arith}}^{\downarrow}}{2} = \quad A^{\gamma}\frac{1 - (A_{\text{gain}})^2}{1 - (A_{\text{gain}}A^{\gamma})^2}. \end{aligned} \tag{3.7}$$

Previous analyses [Dabaghyan, 2007; Gericke et al., 2005, 2006; Gericke, 2004] on this experiment have used the "sum and difference" asymmetry,

$$A_{\mathrm{sd}} = \frac{N_-^{\uparrow} - N_-^{\downarrow}}{N_+^{\uparrow} + N_+^{\downarrow}} = \frac{A^{\gamma} + A_{\mathrm{beam}} A_{\mathrm{gain}}}{1 + A^{\gamma} A_{\mathrm{beam}} A_{\mathrm{gain}}}, \tag{3.8}$$

though this construction requires stricter cuts on A_{beam}. We can estimate the beam asymmetry from the construction

$$A^{+} = \frac{N_+^{\uparrow} - N_+^{\downarrow}}{N_+^{\uparrow} + N_+^{\downarrow}} = \frac{A_{\mathrm{beam}} + A_{\mathrm{gain}} A^{\gamma}}{1 + A^{\gamma} A_{\mathrm{beam}} A_{\mathrm{gain}}}, \tag{3.9}$$

or, for that matter, using an unpaired detector

$$\frac{N_i^{\uparrow} - N_i^{\downarrow}}{N_i^{\uparrow} + N_i^{\downarrow}} = \frac{A_{\mathrm{beam}} + A_i^{\gamma}}{1 + A_i^{\gamma} A_{\mathrm{beam}}}. \tag{3.10}$$

However, we can also construct the "geometric asymmetry." If we define

$$\alpha^{\uparrow} = \frac{N_i^{\uparrow}}{N_j^{\uparrow}} = \frac{G_i}{G_j} \frac{1 + A^{\gamma}}{1 - A^{\gamma}}, \qquad \alpha_i = \frac{N_i^{\uparrow}}{N_i^{\downarrow}} = \frac{N_0^{\uparrow}}{N_0^{\downarrow}} \frac{1 + A^{\gamma}}{1 - A^{\gamma}}, \tag{3.11}$$

$$\alpha = \frac{\alpha^{\uparrow}}{\alpha^{\downarrow}} = \frac{\alpha_i}{\alpha_j} = \left(\frac{1 + A^{\gamma}}{1 - A^{\gamma}} \right)^2, \tag{3.12}$$

then

$$A_{\mathrm{geom}} = \frac{\sqrt{\alpha} - 1}{\sqrt{\alpha} + 1} = A^{\gamma}. \tag{3.13}$$

The geometric asymmetry has the advantage that, in the limit of small pedestal signals P_i, the beam and gain asymmetries A_{beam} and A_{gain} cancel exactly. For completeness, note that

$$A_{\mathrm{geom}}^{\mathrm{spin}} = \frac{\sqrt{\alpha^{\uparrow}\alpha^{\downarrow}} - 1}{\sqrt{\alpha^{\uparrow}\alpha^{\downarrow}} + 1} = A_{\mathrm{gain}} \quad \text{and} \quad A_{\mathrm{geom}}^{\mathrm{det.}} = \frac{\sqrt{\alpha_i \alpha_j} - 1}{\sqrt{\alpha_i \alpha_j} + 1} = A_{\mathrm{beam}} \tag{3.14}$$

estimate the gain and beam asymmetries.

In the absence of pedestals, the four measurements $N_{ij}^{\uparrow\downarrow}$ have five degrees of freedom: two G_{ij}, two $N_0^{\uparrow\downarrow}$, and the physics asymmetry A^{γ}. However, if this model actually describes our signals, the gain asymmetry A_{gain} should not vary over nearby sequences, and all detector pairs should see the same beam asymmetry A_{beam}. We can therefore check the validity of our assumption by comparing different measurements of A_{gain}, A_{beam}, A^{γ} within our overdetermined system.

3.2.2 Pedestal dilution

Our definition (3.2) of the signal N_i does not distinguish between electronic pedestals and physical backgrounds. Doing so would require an enormous effort, connecting an elaborate neutron transport model of the apparatus to detailed historical information about the beam current and collimation. For instance, consider the background due to neutrons which diffuse into the CsI detectors. These neutrons may capture in the aluminum cladding the detector, capture cross section 0.231(3) barn; on iodine, 6.15(6) b; or on cesium, 29.0(1.5) b [NDB]. Each of these produces a cascade of prompt photons and settles into a β-unstable nucleus, with lifetimes 2.2 m, 25 m, and 2.1 y, respectively [NWC]. All of the β decays are accompanied by photons as well; furthermore, about 10% of the capture to cesium populates the 8^- isomer of ^{134}Cs with lifetime 2.9 h [ENSDF]. In current mode these photons cannot be distinguished from the primary signal. Over an 8×50 ms spin sequence, the prompt photons produce a signal proportional to the beam current N_0 with some repeatable neutron time-of-flight structure. The delayed photons produce a background sensitive to beam current fluctuations over the lifetime of the emitter. Because the process of closing the shutter typically took minute or two, comparable to the lifetime of the aluminum background, the background measured during our beam-off runs was not the same as the background during the chopper-closed part of each pulse.

Rather than devise an elaborate background subtraction scheme, then, we show here how the relations of the preceding section change with the inclusion of pedestals. Define the ratio $r \equiv N_0^\uparrow / N_0^\downarrow$ as a proxy for A_{beam}, and the pairwise "reduced pedestals"

$$\begin{aligned} \Sigma p &= \frac{\Sigma P}{N_0^\uparrow \Sigma G} \qquad & r\Sigma p &= \frac{\Sigma P}{N_0^\downarrow \Sigma G} = \frac{1 + A_{\text{beam}}}{1 - A_{\text{beam}}} \Sigma p \\ \Delta p &= \frac{\Delta P}{N_0^\uparrow \Sigma G} \qquad & r\Delta p &= \frac{\Delta P}{N_0^\downarrow \Sigma G} \end{aligned} \tag{3.15}$$

This is a slight abuse of notation, since the reduced pedestal for a single detector $p_i = \Sigma p + \Delta p$ depends on both G_i and G_j. These abbreviations make it easier to see that our estimator for the beam asymmetry becomes

$$A^+ = \frac{A_{\text{beam}} + A_{\text{gain}} A^\gamma}{1 + A^\gamma A_{\text{beam}} A_{\text{gain}} + (1 + A_{\text{beam}}) \Sigma p}. \tag{3.16}$$

A better route to the beam asymmetry might be a single detector

$$\frac{N_i^\uparrow - N_i^\downarrow}{N_i^\uparrow + N_i^\downarrow} = \frac{A_{\text{beam}} + A_i^\gamma}{1 + A_i^\gamma A_{\text{beam}} + 2P_i / G_i \Sigma N_0}. \tag{3.17}$$

In either case the sensitivity is reduced by the pedestal. The sum-and-difference asymmetry also has the nice property that the pedestals enter only as a scale factor,

$$A_{\text{sd}} = \frac{A^\gamma + A_{\text{beam}} A_{\text{gain}}}{1 + A^\gamma A_{\text{beam}} A_{\text{gain}} + (1 + A_{\text{beam}})\, \Sigma p}. \tag{3.18}$$

The arithmetic asymmetries have the denominator

$$\begin{aligned} N_+^\uparrow N_-^\uparrow (1 - A_{\rm beam}) \\ \propto (1 + (A^\gamma A_{\rm gain})^2)(1 - A_{\rm beam}) \\ + 2\,\Sigma p\,(1 + A^\gamma A_{\rm beam} A_{\rm gain} + (1 + A_{\rm beam})\Sigma p/2) \end{aligned} \quad (3.19)$$

and numerators

$$\begin{aligned} (N_-^\uparrow N_+^\downarrow + N_-^\downarrow N_+^\uparrow)(1 - A_{\rm beam}) \\ \propto A_{\rm gain}(1 - (A^\gamma)^2)(1 - A_{\rm beam}) + \Delta p(1 + A^\gamma A_{\rm beam} A_{\rm gain}) \\ + (1 + A_{\rm beam})\Delta p \Sigma p + \Sigma p (A^\gamma A_{\rm beam} + A_{\rm gain}), \end{aligned} \quad (3.20)$$

$$\begin{aligned} (N_-^\uparrow N_+^\downarrow - N_-^\downarrow N_+^\uparrow)(1 - A_{\rm beam}) \\ \propto A^\gamma (1 - (A_{\rm gain})^2)(1 - A_{\rm beam}) - \Delta p (A_{\rm beam} + A^\gamma A_{\rm gain}) \\ + \Sigma p (A_{\rm beam} A_{\rm gain} + A^\gamma). \end{aligned} \quad (3.21)$$

If all of the A, p are small enough to neglect below second order,

$$\begin{aligned} A^+_{\rm arith} &\approx (\Delta p + A_{\rm gain})(1 - \Sigma p) + \Delta p A_{\rm beam} \\ A^-_{\rm arith} &\approx A^\gamma \cdot (1 - \Sigma p) - \Delta p A_{\rm beam}. \end{aligned} \quad (3.22)$$

Here, too, the pedestal dilutes the sensitivity of the mathematical $A^\pm_{\rm arith}$ to their physical counterparts; also, simultaneous beam and pedestal asymmetries mix these two constructions. A similar expression holds for $A_{\rm geom}$ [Wilburn, 2007].

3.2.3 Relations among the different asymmetries

The preceding section presented three estimators $A^-_{\rm arith}$, $A_{\rm geom}$, $A_{\rm sd}$ for the physics asymmetry A^γ. Each estimator is computed by a different combination of the same four signals $N^{\uparrow\downarrow}_{AB}$ from parity-conjugate detectors A and B, and has a different set of sensitivities to gain asymmetries, beam asymmetries, and pedestals. Here we construct analytic expressions in the $N^{\uparrow\downarrow}_{AB}$ connecting the various estimators for A^γ, and consider the results as estimators for systematic effects.

First we evaluate the difference $A^-_{\rm arith} - A_{\rm geom}$. We rewrite

$$A^-_{\rm arith} - A_{\rm geom} = \frac{N_A^\uparrow N_B^\downarrow - N_A^\downarrow N_B^\uparrow}{N_+^\uparrow N_+^\downarrow} - \frac{\sqrt{N_A^\uparrow N_B^\downarrow} - \sqrt{N_A^\downarrow N_B^\uparrow}}{\sqrt{N_A^\uparrow N_B^\downarrow} + \sqrt{N_A^\downarrow N_B^\uparrow}}. \quad (3.23)$$

The numerator will contain the difference of the two terms

$$\left(N_A^{\uparrow}N_B^{\downarrow} - N_A^{\downarrow}N_B^{\uparrow}\right)\left(\sqrt{N_A^{\uparrow}N_B^{\downarrow}} + \sqrt{N_A^{\downarrow}N_B^{\uparrow}}\right)$$
$$= \sqrt{N_A^{\uparrow}N_B^{\downarrow}}\sqrt{N_A^{\downarrow}N_B^{\uparrow}}\left(\sqrt{N_A^{\uparrow}N_B^{\downarrow}} - \sqrt{N_A^{\downarrow}N_B^{\uparrow}}\right)$$
$$+ \left(N_A^{\uparrow}N_B^{\downarrow}\right)^{3/2} + \left(N_A^{\downarrow}N_B^{\uparrow}\right)^{3/2} \quad (3.24)$$

and

$$\left(\sqrt{N_A^{\uparrow}N_B^{\downarrow}} - \sqrt{N_A^{\downarrow}N_B^{\uparrow}}\right)\left(N_A^{\uparrow} + N_B^{\uparrow}\right)\left(N_A^{\downarrow} + N_B^{\downarrow}\right)$$
$$= \left(N_A^{\uparrow}N_A^{\downarrow} + N_B^{\uparrow}N_B^{\downarrow} - \sqrt{N_A^{\uparrow}N_B^{\downarrow}}\sqrt{N_A^{\downarrow}N_B^{\uparrow}}\right)\left(\sqrt{N_A^{\uparrow}N_B^{\downarrow}} - \sqrt{N_A^{\downarrow}N_B^{\uparrow}}\right)$$
$$+ \left(N_A^{\uparrow}N_B^{\downarrow}\right)^{3/2} + \left(N_A^{\downarrow}N_B^{\uparrow}\right)^{3/2}. \quad (3.25)$$

The terms to the 3/2 power cancel, so the overall difference becomes

$$A^{-}_{\text{arith}} - A_{\text{geom}} = \frac{-\left(\sqrt{N_A^{\uparrow}N_A^{\downarrow}} - \sqrt{N_B^{\uparrow}N_B^{\downarrow}}\right)^2}{N_+^{\uparrow}N_+^{\downarrow}}A_{\text{geom}}. \quad (3.26)$$

We see that A^{-}_{arith} and A_{geom} always have the same sign, but A^{-}_{arith} has a smaller magnitude for all $N_{AB}^{\uparrow\downarrow}$. Compare this to the ratio of (3.7) and (3.13),

$$\frac{A^{-}_{\text{arith}}}{A_{\text{geom}}} \approx 1 - A^2_{\text{gain}}. \quad (3.27)$$

Apparently, in the limit of small pedestals, the combination of $N_{AB}^{\uparrow\downarrow}$ in (3.26) estimates the gain asymmetry. The construction A^{+}_{arith} also estimates the gain asymmetry, but using again a different construction. The distinction is that (3.27) holds only when the pedestal signal is small, while (3.26) is exact.

Next we consider the relation between A^{-}_{arith} and A_{sd}. We have seen above that the construction

$$A^{+} = \frac{N_+^{\uparrow} - N_+^{\downarrow}}{N_+^{\uparrow} + N_+^{\downarrow}} = \frac{R-1}{R+1}, \text{ where the ratio } R \equiv \frac{N_+^{\uparrow}}{N_+^{\downarrow}}, \quad (3.28)$$

gives the beam asymmetry A_{beam} at first order. We may write the sum and difference asymmetry as

$$A_{\text{sd}} = \frac{A^{\uparrow}_{\text{arith}}N_+^{\uparrow} - A^{\downarrow}_{\text{arith}}N_+^{\downarrow}}{N_+^{\uparrow} + N_+^{\downarrow}}$$
$$= \frac{RA^{\uparrow}_{\text{arith}} - A^{\downarrow}_{\text{arith}}}{R+1} = \frac{(R-1)A^{+}_{\text{arith}} + (R+1)A^{-}_{\text{arith}}}{R+1}$$
$$= A^{-}_{\text{arith}} + A^{+}A^{+}_{\text{arith}} \quad (3.29)$$

Compare this exact expression to the small-pedestal approximations of section 3.2.1:

$$\begin{gathered} A^-_{\text{arith}} \approx A^\gamma \qquad A^+ \approx A_{\text{beam}} \qquad A^+_{\text{arith}} \approx A_{\text{gain}} \\ A_{\text{sd}} \approx A^\gamma + A_{\text{beam}} A_{\text{gain}}. \end{gathered} \tag{3.30}$$

3.2.4 Signal reconstruction and integer arithmetic

In addition to the possible connection with instrumental effects, the existence of multiple, algebraically equivalent expressions for each asymmetry in terms of the others offers some protection against numerical errors. It is unlikely, for instance, that programming mistakes would preserve the identities above. More interestingly, these permit estimates of the experiment's sensitivity to the quirks of arithmetic on finite computing hardware.

The IEEE standard for "double precision" floating-point arithmetic divides a 64 bit number into one sign bit, eleven bits for the exponent, and 52 bits for the mantissa. However it is well-known [see e.g. Press et al., 1992] that many straightforward algorithms are unstable against truncation errors: the difference between two double-precision numbers with their first n bits in common can have a precision no better than $52 - n$ bits. Since our problem here is the statistical extraction of an asymmetry $A_\gamma \sim 10^{-8}$ between like-sized numbers, near the single-precision limit, we must ask whether truncation bias could produce a false effect.

Here we are comparing signals stored as integer ADC readings. Integers up to 2^{53} have exact floating-point representations;[20] computations involving integers can therefore be done exactly, even if the data storage type is floating point. Calculations of A_{arith} and A_{sd} can be constructed to use integer subtraction. For A_{geom}, however, the difference involves a square root and has no integer representation. With this motivation we construct the signals and asymmetries as follows.

The ADC signal from detector i in ring r at time t is

$$N_{i,r}(t) = \frac{1}{3}\left(\frac{S_r(t)}{25} + \frac{D_{i,r}(t)}{20 \cdot 10}\right), \tag{3.31}$$

where S_r and $D_{i,r}$ are the ADC outputs from the sum and difference amplifiers, connected as shown in figure 3.2. The various gain factors — 3 from the Bessel filters, 25 and 20 from the multiple readings summed in each ADC, and 10 from the difference amplifier — can be absorbed into "ADC gains" $G_S = 1/75$ and $G_D = 1/600$. Our ADCs divide 10 volts into 2^{15} channels.

In (3.7) we write $A^\pm_{\text{arith}}$ as the means of $\pm A^{\uparrow\downarrow}_{\text{arith}}$. In both cases we can put a single integer subtraction in the numerator. Define

$$2\ \texttt{NNNN}^\pm = N^\uparrow_- N^\downarrow_+ \pm N^\downarrow_- N^\uparrow_+ \tag{3.32}$$

[20] That is, the floating point operation $2^{53} - 1$ results in an odd integer, but the result of the operation $2^{53} + 1$ is even after truncation.

with $N_{\pm}^{\uparrow\downarrow}$ as in (3.5). In terms of the four detector signals,

$$\begin{aligned} \texttt{NNNN}^{+} &= N_i^{\uparrow} N_i^{\downarrow} - N_j^{\uparrow} N_j^{\downarrow} \\ \texttt{NNNN}^{-} &= N_i^{\uparrow} N_j^{\downarrow} - N_j^{\uparrow} N_i^{\downarrow}. \end{aligned} \tag{3.33}$$

and $A_{\text{arith}}^{\pm} = \texttt{NNNN}^{\pm}/N_{+}^{\uparrow} N_{+}^{\downarrow}$. Because $G_S/G_D = 8$ is an integer, we may compute asymmetries using N/G_D and the above constructions without introducing numerical roundoff errors.

3.3 Consistency checking

We outline our program of internal consistency checking. For clarity we consider a single run, number 52 900, taken with a full, converted hydrogen target on 2008-12-08 in the afternoon. This was a standard 10 000 T_0 run, divided into 1250 sequences. For a dozen pulses early in the run, VME2 recorded garbage instead of valid headers and difference ADC signals in the range $\pm 10\,\text{V}$; the three sequences containing these pulses were excluded from further analysis. The mean proton current reported for pulses in this run was 94 µA, distributed with width $\sim 1\,\mu\text{A}$. These features are visible in the data summary shown in figure 3.3.

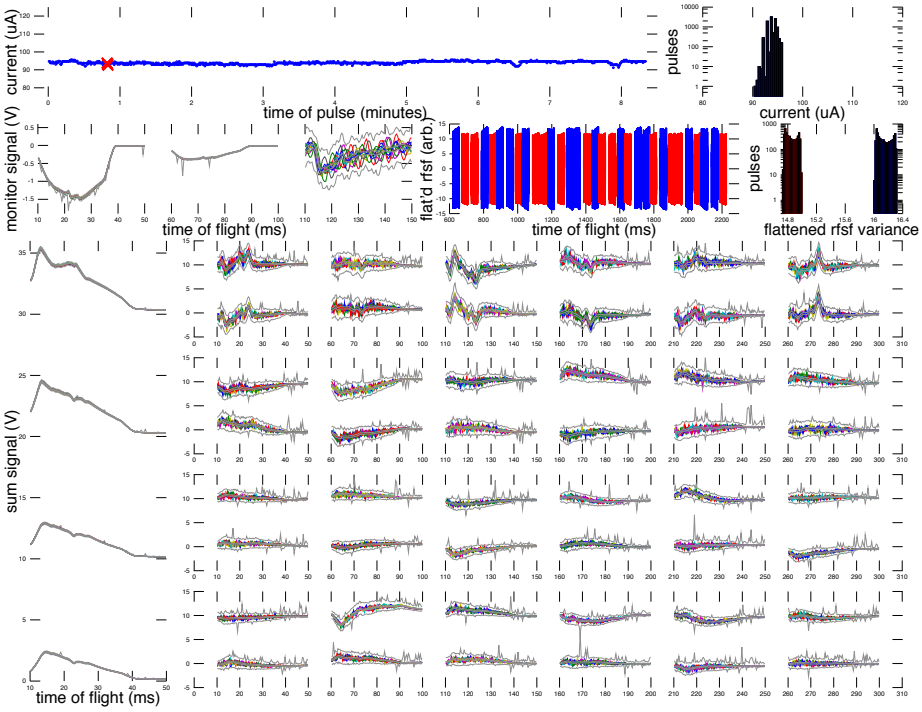
This typical run occupies $\sim 300\,\text{MB}$ on disk, of which $\sim 200\,\text{MB}$ is detector difference signals stored in 32 bit integers. In the construction of the detector signals $N^{\uparrow\downarrow}$, we limit the size of temporary variables to by using 32 bit integers to form spin state sums $S^{\uparrow\downarrow}$ and $D^{\uparrow\downarrow}$ from the sum and difference amplifier data. These sums are converted to 64 bit signals $N^{\uparrow\downarrow}$ by the truncation-free method discussed in section 3.2.4. Each $48 \times 100 \times 1250$ array of 64 bit $N^{\uparrow\downarrow}$ occupies $\sim 50\,\text{MB}$; each array of asymmetries, correction factors, etc. is half as large.

3.3.1 Truncation errors are negligible

In figure 3.4 we summarize the arithmetic asymmetries A_{arith} for this run. Note the difference in distribution between the intensity peak at $\sim 15\,\text{ms}$ time of flight and the chopper-closed period after $\sim 35\,\text{ms}$. Rather than presenting indistinguishable figures for the geometric and sum-and-difference asymmetries, figure 3.6 shows histograms of the roundoff error measured by calculating the A_{arith} directly or via the identities (3.26) and (3.29). The observation that these truncation errors effectively vanish lends strong support to the claim that we have calculated the various asymmetries in a consistent way. Other comparisons have shown that the analysis presented here and independently developed tools report identical values for reconstructed signals, suggesting insight drawn from this analysis is applicable elsewhere.

3.3.2 Computed asymmetries are normally distributed

We expect that the asymmetry $A_{i,t}^{\gamma}$ in the ith pair at time t is drawn from a normal distribution with mean $A_{i,t}$ and width $\sigma_{i,t}$, where $\sigma_{i,t}$ is dominated



First row: facility-reported beam current over the run, and its histogram. Rejected pulses are marked with a red ×.

Second row, left: monitor signals, upstream to downstream, from ten random pulses in the run, with extreme values and 33% quantiles at each time of flight in grey. Note ∼ 180 Hz microphoning clearly visible in third monitor.

Second row, middle: current in spin flipper ampilifier, flattened by multiplying by time of flight, first 32 pulses. Color indicates the desired spin state. Time jitter is an artifact of the VME software clock. Flipped and unflipped pulses have slightly different amplitudes, due to imprecise impedance matching between the spin flipper and the dummy load.

Second row, right: histogram of variances of the flattened spin flipper current signals, over the entire run. Lack of overlap between "up" (blue) and "down" (red) amplitudes suggests no spin flipper problems this run.

Bottom: sum and difference signals from the 4 × 12 detectors. Samples, extrema, and 33% quantiles as in monitor data. Ring data are presented from upstream (top) to downstream (bottom). Note sum signal size decreases downstream, and the intesity peak is delayed by ∼ 1.5 ms from the first to the fourth ring. Difference signals are arranged left to right, top to bottom, so that parity-conjugate pairs of signals are aligned vertically.

Figure 3.3: Data summary from run 52 900.

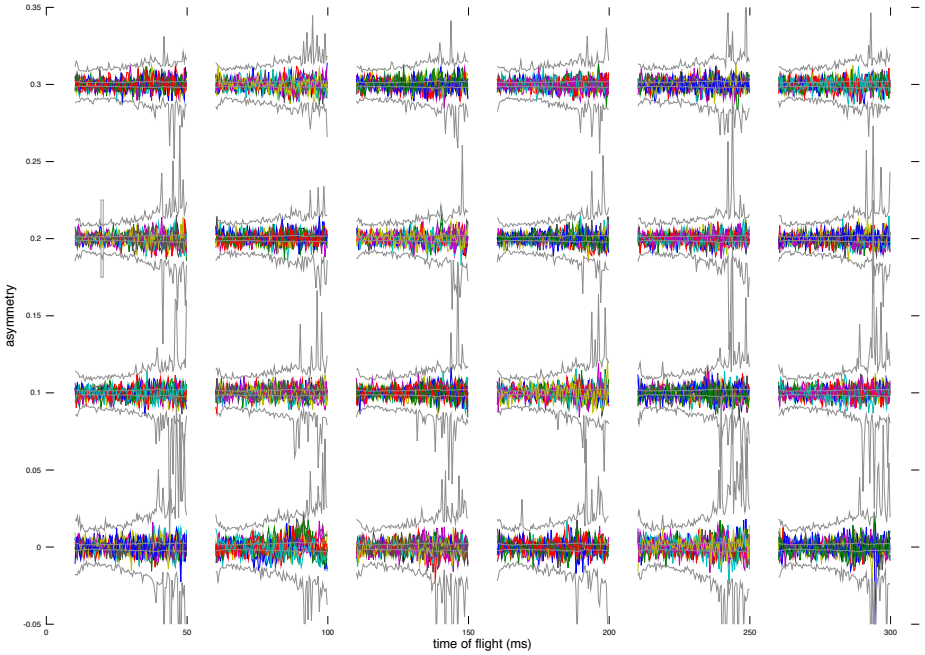
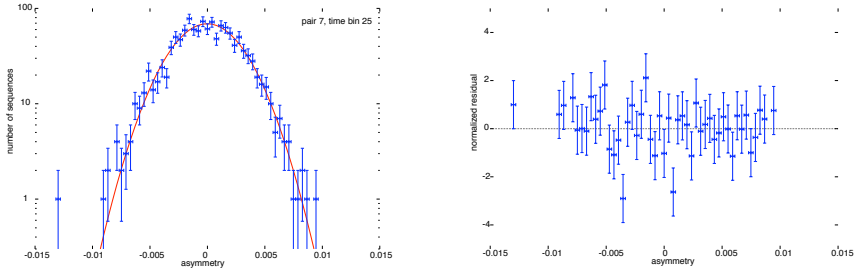
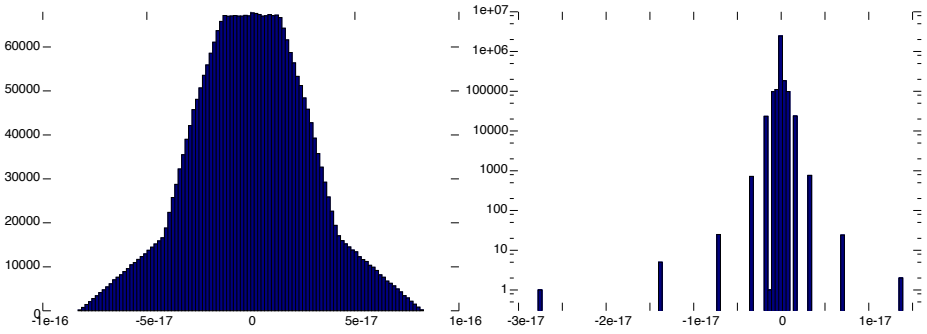


Figure 3.4: Arithmetic asymmetries for run 52 900. Colored curves are asymmetry vs. time of flight for the 4×6 detector pairs for ten random sequences; grey curves show extreme values and 33% quantiles for all 1247 sequences. Pairs are arranged in the same order as the difference signals in figure 3.3: the upstream ring is at top. Rows are offset by 0.1, though most asymmetries are on the 10^{-3} scale. Grey box: see figure 3.5.



(a) (b)

Figure 3.5: Asymmetry histogram for run 52 900, detector pair 7, 19.8 ms time bin, marked with a grey box on figure 3.4. (a) Horizontal error bars, bin width; vertical error bars, $\sqrt{N}$. Solid curve, best-fit gaussian with width $\sigma = 2.8 \times 10^{-3}$ and mean $\mu = -(2.3 \pm 8.0) \times 10^{-5}$; error on the mean is $\sigma/\sqrt{N_{\text{total}}}$. (b) Normalized residuals. Note that the 1 ± 1 "outlier" asymmetry at $A^{\gamma}_{i,t} = -0.013$ is not inconsistent with the $\ll 1$ expected in that bin. This fit overall has $\chi^2/\text{d.o.f.} = 44.0/44$.



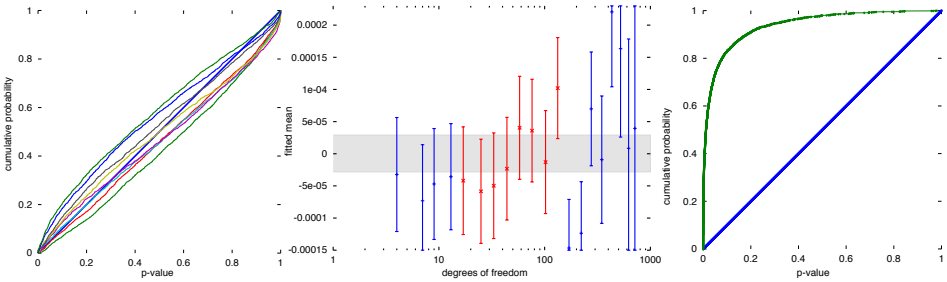
(a) (b)

Figure 3.6: Histograms of roundoff errors in run 52 900, estimating truncation error in (a) $A_{\rm geom}$, equation 3.26, (b) $A_{\rm sd}$, equation 3.29. Roughly 70% of the $A_{\rm sd}$ truncation errors are exactly zero. All are small relative to the double precision scale $2^{-52} = 2 \times 10^{-16}$. See text.

by shot noise and $A_{i,t}$ depends on the physics asymmetry, geometry, neutron polarization, etc. as outlined in chapter 3. To estimate these parameters from our data, we collect asymmetries into histograms and use an implementation of the Levenberg-Marquardt χ^2 minimization algorithm. Figure 3.5 shows a representative distribution of 1247 sequence asymmetries, for a single time bin in a single detector pair; this dataset is enclosed by a grey box in figure 3.4. This histogram has 47 nonempty bins and three fitted parameters, and the best-fit gaussian with mean $A^{\gamma}_{i,t} = (-2.3 \pm 8.0) \times 10^{-5}$ has $\chi^2 = 44.0$. The probability of drawing a smaller number from a χ^2 distribution with 44 degrees of freedom is $p = 0.53$.

If the asymmetries $A^{\gamma}_{i,t}$ differ from a normal distribution due only to sampling noise, and the χ^2 minimization behaves correctly, then the parameter p is a random variable drawn from a uniform distribution between zero and one. With 24×100 independent parameter estimates, our ensemble of p-values may be used to evaluate the performance of our fitting procedure. Figure 3.7a shows the cumulative distributions of p-values obtained for sets of fits with different histogram bin widths. Fits with narrower bins have an excess of "overconverged" fits with small χ^2 and p; fits with wide bins have an excess of "poor" fits with large χ^2 and p. The bin widths in the eight ensembles of fits in figure 3.7a vary by a factor of ten. All have mean p between 0.4 and 0.6 and in all eight the distribution of p is broadly uniform. From figure 3.7a we conclude the ensemble of asymmetries in figure 3.4 is consistent with an ensemble drawn from 24×100 normal distributions, independent of the choice of histogram used for the fit.

Figure 3.7b displays the mean asymmetry of the representative dataset from figure 3.5, as fitted from histograms with several different bin sizes. The eight binnings of figure 3.7a are shown in red; means fitted from wider and narrower binnings, for which the ensemble of p was less uniform, are in blue. Even far



(a) (b) (c)

Figure 3.7: Insensitivity of fits to histogram binning. (a) Cumulative distributions of p-values for asymmetry fits with histogram bin widths from 10^{-4} to 10^{-3}; solid diagonal, uniform distribution. (b) Means for pair 7, time bin 25, fitted with different bin widths. The dataset shown in figure 3.5 has 44 degrees of freedom. Fits included in (a) in red; their error-weighted average $(0.0\pm2.9)\times10^{-5}$, grey band. (c) Distribution of p-values for these error-weighted averages. See text.

from the range where the goodness-of-fit statistic follows a χ^2 distribution, the best fit for the mean asymmetry is consistent, within errors, with the value from the well-behaved ensemble of fits. With *very* narrow bins this method overestimates the width σ of the asymmetry distribution, and therefore the error on the mean $\sigma/\sqrt{N}$. Reduced sensitivity to σ probably comes in part from the decision to assign zero weight to empty bins; this weighting eliminates from the fit any information about the faraway edges of the histogram, but reduces the χ^2 distinction between clusters of similar values and outliers. If our data were more sparse, it might be appropriate to consider a different algorithm where empty bins also contribute. We do not pursue this possibility here.

Visual inspection of figure 3.7b suggests that, for our representative time bin, the mean asymmetry and its uncertainty are robust against histogram rebinning. To determine whether this robustness holds across all our data sets, we find for each one an error-weighted average of the central values reported in the eight well-behaved ensembles of fits. We may then compute the χ^2 deviation between the average and the results of the individual fits. The representative dataset in figure 3.7b has $\chi^2/\text{d.o.f.} = 3.39/8$, or $p = 0.092$. The distribution of p for the ensemble of well-behaved fits appears in figure 3.7c; roughly 80% of the fits have $p < 0.1$. This distribution is quite clearly inconsistent with uniform p, suggesting that the parameters from various fits are not independent of each other. We conclude that changing histogram binning does not change the mean asymmetry reported by a fit, for this eight-minute data set.

3.4 Weighting and averaging

We have now established several ways to disentangle the photon asymmetry A_i^γ seen between the ith and jth detectors from the various instrumental and background effects that interfere with it. In this section we relate these "raw" detector asymmetries to the physics asymmetry A_γ.

3.4.1 Polarization and geometry weighting

We have seen that the neutron polarization leaving P_n leaving the ^{3}He polarizer is not uniform but varies with wavelength,

$$P_\mathrm{n}(\lambda) = \tanh x\lambda. \tag{3.34}$$

As alluded in section 2.2.2, a thorough effort to estimate the parameter $x = n\ell\sigma_0 P_3/\lambda_0$ raised some subtle questions. The cells used in the 2006 data runs had thickness $n\ell \approx 1.3\times10^{20}\,\mathrm{atom\,cm^{-2}}$ and operated with polarization $P_3 =$ 50–55%.

The raw asymmetries A_i^γ contain parity-conserving (left-right) and parity-violating (up-down) contributions. We quantify this by defining "geometry factors" G_i so that

$$A_i^\gamma \equiv P_\mathrm{n}\left(A_\mathrm{UD}G_i^\mathrm{UD} + A_\mathrm{LR}G_i^\mathrm{LR}\right). \tag{3.35}$$

As in section 2.5, define a right-handed coordinate system $\vec{y},\vec{z},\vec{x}$ (up, downstream, left) in the directions of the neutron's average spin $\vec{\sigma}_\mathrm{n}$, momentum $\vec{k}_\mathrm{n}$, and their product $\vec{\sigma}_\mathrm{n}\times\vec{k}_\mathrm{n}$, respectively. Also define spherical coordinates r,θ,ϕ, where θ is the angle between a vector and $\vec{y}$ and ϕ is the angle of the projection onto the z-x plane. (This is permuted from the usual spherical coordinates, where $\vec{z}$ is "up.") A photon traveling from a neutron capture at some location $\vec{r}_c$ to a detector at $\vec{r}_d$ has momentum with some angles θ,ϕ. Reversing the neutron spin $\vec{\sigma}_\mathrm{n}$ changes $\vec{\sigma}_\mathrm{n}\times\vec{k}_\mathrm{n}$ but not $\vec{k}_\mathrm{n}$, and is equivalent to replacing θ,ϕ with

$$\begin{aligned}\theta' &= \pi - \theta\\ \phi' &= -\phi.\end{aligned} \tag{3.36}$$

Under this transformation the energy deposited in the detector,

$$\frac{d\Gamma}{d\Omega}d\Omega \propto 1 + A_\mathrm{UD}\cos\theta + A_\mathrm{FB}\sin\theta\cos\phi + A_\mathrm{LR}\sin\theta\sin\phi, \tag{3.37}$$

becomes

$$\frac{d\Gamma}{d\Omega'}d\Omega' \propto 1 - A_\mathrm{UD}\cos\theta + A_\mathrm{FB}\sin\theta\cos\phi - A_\mathrm{LR}\sin\theta\sin\phi. \tag{3.38}$$

By comparison with our definition (3.2) of the signals N_i, a pointlike source and detector therefore have the geometry factors

$$G_\mathrm{point}^\mathrm{UD} = \cos\theta \qquad \text{and} \qquad G_\mathrm{point}^\mathrm{LR} = \sin\theta\sin\phi. \tag{3.39}$$

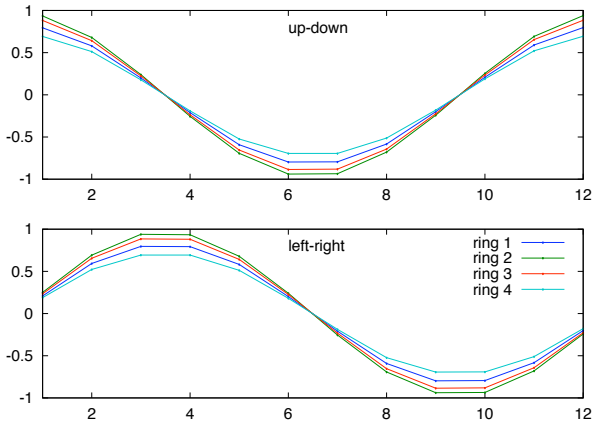


Figure 3.8: Geometry factors. Top, G^{UD}, bottom, G^{LR}, versus detector number, for each ring. Ring 1 is upstream. The variation 0.01–0.03 with time of flight, as the capture locus shifts with neutron energy, is not visible at this scale.

Computing the geometry factors for physical detectors requires integrating these expressions over the source and detector volumes.

The geometry factors used in this analysis were computed using a numerical transport model of the experiment. This model was constructed in two stages: an MCNP model to find the neutron capture flux in the target, and MCNP and GEANT4 photon transport models of using this neutron flux as a source density. We present results in Figure 3.8.

3.4.2 Error weighting and counting statistics

For each spin sequence, for each detector pair, each time bin provides a statistically independent measurement of A_i^γ with uncertainty σ_i. To extract A_{UD} and A_{LR}, construct individual estimators

$$\begin{aligned} A_i^{\mathrm{UD}} \pm \sigma_i^{\mathrm{UD}} &= \frac{A_i^\gamma \pm \sigma_i}{P_{\mathrm{n}} G_i^{\mathrm{UD}}} = \left(A_{\mathrm{UD}} + \frac{A_{\mathrm{LR}} G_i^{\mathrm{LR}}}{G_i^{\mathrm{UD}}} \right) \pm \frac{\sigma_i}{P_{\mathrm{n}} G_i^{\mathrm{UD}}}, \\ A_i^{\mathrm{LR}} \pm \sigma_i^{\mathrm{LR}} &= \frac{A_i^\gamma \pm \sigma_i}{P_{\mathrm{n}} G_i^{\mathrm{LR}}}, \end{aligned} \tag{3.40}$$

and add them according to the usual rule

$$A_{\mathrm{tot}} = \frac{\sum A_i/\sigma_i^2}{\sum 1/\sigma_i^2}, \qquad \sigma_{\mathrm{tot}}^2 = \frac{1}{\sum 1/\sigma_i^2}. \tag{3.41}$$

Our overall estimator $A_{\rm obs}^{\rm UD}$ for the physical asymmetry $A_{\rm UD}$ then has uncertainty

$$\sigma_{\rm obs}^{\rm UD} = 1 \Bigg/ P_{\rm n}\sqrt{\sum \left(\frac{G_i^{\rm UD}}{\sigma_i}\right)^2} \tag{3.42}$$

and central value

$$A_{\rm obs}^{\rm UD} = \left(A_{\rm UD} + \left(\sigma_{\rm obs}^{\rm UD}\right)^2 A_{\rm LR} \sum P_{\rm n}^2 \frac{G_i^{\rm UD} G_i^{\rm LR}}{\sigma_i^2}\right). \tag{3.43}$$

Similarly, the estimator $A_{\rm obs}^{\rm LR}$ for the physical asymmetry $A_{\rm LR}$ has the value

$$A_{\rm obs}^{\rm LR} = \left(A_{\rm LR} + \left(\sigma_{\rm obs}^{\rm LR}\right)^2 A_{\rm UD} \sum P_{\rm n}^2 \frac{G_i^{\rm UD} G_i^{\rm LR}}{\sigma_i^2}\right) \tag{3.44}$$

where $\sigma_{\rm obs}^{\rm LR}$ is analogous to (3.42). Even in the limit where the detector array is aligned with the vertical, and an unweighted sum $\sum G_i^{\rm UD} G_i^{\rm LR} \sim \sum \cos\theta_i \sin\theta_i$ vanishes, the up-down and left-right asymmetries will still mix if opposing pairs have different efficiencies.

Chapter 4

$\vec{\mathrm{n}} + \mathrm{p} \to \mathrm{d} + \gamma$ at the Spallation Neutron Source

The world's most intense pulsed neutron source is at present the Spallation Neutron Source (SNS) at Oak Ridge National Laboratory (ORNL). Recall that the LANSCE linear accelerator brings a $\sim 100\,\mu\mathrm{A}$ current of H^- ions to energy 800 MeV. In the SNS linac, which also begins with room-temperature drift-tube and coupled-cavity sections, the bulk of the energy is delivered to the beam in superconducting microwave cavities. Technical improvements to the ion source permit a much larger current, up to 1.4 mA. The accelerator as commissioned in 2007 gives these ions an energy 1 GeV; space exists along the linac to add additional superconducting cavities in a future upgrade. As at LANSCE, multiple H^- pulses leaving the linac are stripped and trapped in a storage ring. During full power operation the SNS storage ring will empty proton bunches onto the spallation target at 60 Hz.

The spallation target is designed to dissipate heat at up to two megawatts; this heat load precludes the use of solid metal. The SNS target system contains roughly a ton of liquid mercury, which circulates through the $\sim (15\,\mathrm{cm})^3$ "thimble" actually exposed to the beam with a period of about a minute. Neutrons leaving the spallation target may then interact with any of several room- and low-temperature moderators, and each moderator is viewed by several beamlines. The SNS accelerator, target, and moderator systems have been described extensively elsewhere.[21]

The $\vec{\mathrm{n}} + \mathrm{p} \to \mathrm{d} + \gamma$ experiment has been approved for installation on SNS beamline 13, the Fundamental Neutron Physics beamline (FnPB). The FnPB is a $10 \times 12\,\mathrm{cm}^2$, $m = 3.6$ supermirror guide ending 15 m from the face of a coupled liquid hydrogen moderator. A five-channel section of guide, curving with radius ~ 100 m over 5 m of the upstream portion of the beamline, eliminates any direct line of sight from the end of the beamline to the moderator. This

[21] For an extensive set of technical and nontechnical literature about the SNS, see `http://neutrons.ornl.gov`.

makes the moderator imaging discussed in section 2.1.1 impossible. However it also prevents unmoderated neutrons and photons produced during the spallation pulse from reaching the experiment without scattering (incoherently) from the guide. The use of a bent beamline to shield against hard radiation simplifies the shielding requirements for the experimental area: most of the radiation in the cave is slow neutrons and their capture photons.

Some parts of the $\vec{\mathrm{n}} + \mathrm{p} \to \mathrm{d} + \gamma$ apparatus will be slightly different after the move to the FnPB. Because the neutron energy spectrum and flight path length are not substantially different from at LANSCE, the neutron time of flight spectrum produced by each spallation pulse will not change substantially: the most intense neutron flux will reach the experiment $\sim 15\,\mathrm{ms}$ after the pulse in a peak roughly 15 ms wide. However the tripled repetition rate eliminates the long chopper-closed period used at LANSCE to estimate pedestals, and the period of fast neutrons used to transfer data. Part of the increased flux on the FnPB relative to LANSCE FP12 is due to the larger guide, $10 \times 12\,\mathrm{cm}^2$ compared to $9.5 \times 9.5\,\mathrm{cm}^2$. Accepting the larger beam requires the construction of new ion chambers. Also, due in part to the larger-area beam, and in part to neutron radiation effects in polarized Rb/^{3}He cells [Sharma et al., 2008], the SNS beam will pass through a supermirror polarizer rather than a polarized gas cell. Several operational improvements will be made to the liquid hydrogen cryogenics system, but the detector array will remain essentially unchanged. The remainder of this chapter describes the FnPB chopper system.[22]

The Fundamental Neutron Physics beamline (FnPB) at the Spallation Neutron Source (SNS) has spaces for up to four choppers, to permit extremely clean correlations between wavelength and time of flight. However, the first experiment to run at the SNS will be $\vec{\mathrm{n}} + \mathrm{p} \to \mathrm{d} + \gamma$, which doesn't need such high precision. Our task here is to find the optimal opening angles for two choppers, and to demonstrate those choppers are adequate for $\vec{\mathrm{n}} + \mathrm{p} \to \mathrm{d} + \gamma$.

To study the chopper performance, we employ a set of analytic manipulations of the predicted FnPB spectrum. The intuition provided by this analysis guides a Monte Carlo optimization of chopper location(s), opening angles, and opening times. The optimization is performed by choosing various cuts on a single Monte Carlo ensemble, rather than by comparing a large number of independent simulations; this technique is fairly fast and has permitted a very detailed examination of the behavior of the chopper system.

We show that putting choppers in the housings at 5.5 m and 7.5 m from the moderator offers a way to make a high-precision measurement of the neutron spectrum out to $\sim 25\,\text{Å}$, clean measurements of the opening and closing times of both choppers, and the opportunity to take beam-on pedestal data. Because these two choppers are in the multichannel section of the guide, their open and close times can be reduced by about 20% by counter-rotation. We find that the regions of frame overlap with these two choppers conspire with the

[22] The remainder of this chapter is largely unchanged from an unpublished November 2006 technical note by Rob Mahurin and Chris Crawford. Both authors contributed equally. This analysis took place before the proposal to use an supermirror polarizer on the FnPB, and so references here to the "polarizer" refer to a ^{3}He cell.

$\vec{\mathrm{n}} + \mathrm{p} \to \mathrm{d} + \gamma$ spin sequence $\uparrow\downarrow\downarrow\uparrow\downarrow\uparrow\uparrow\downarrow$ and the shape of the FnPB spectrum to suggest an obvious operating window whose figure of merit is relatively insensitive to the chopper opening angles (or, equivalently, to the precise location of the experiment). We recommend chopper opening angles of 132° at 5.5 m and 167° at 7.5 m.

4.1 An analytic chopper

We'll consider a chopper as a system with these parameters:

$$\begin{array}{rl} \text{a position} & x \\ \text{an open fraction} & w \\ \text{a frequency} & \nu = 60\,\mathrm{Hz} \\ \text{an opening time} & f_o \\ \text{a closing time} & f_c, \text{ and} \\ \text{“inner” and “outer” crossing times} & t_1, t_2. \end{array} \tag{4.1}$$

Physically a chopper is an aluminum disc with radius $r \approx 0.300\,\mathrm{m}$, coated everywhere with gadolinium paint except for a slice with “opening angle” $\theta = w \cdot 2\pi\,\mathrm{radian}$. The wheel rotates with the frequency ν of the accelerator. The chopper takes a finite amount of time to open, but its transmission is otherwise approximately a step function. As a function of the angle ϕ that the opening edge makes with the vertical $\phi_0 = 0$, as shown in Figure 4.1, the exposed area of a guide with height h and width d is as follows.

Let ϕ_1 and ϕ_2 be the angles at which the opening edge of the chopper window is at the lower and upper corner of the guide, respectively; that is,

$$\begin{aligned} \tan\phi_1 &= d/2r, \text{ and} \\ \tan\phi_2 &= \frac{d/2}{r-h}. \end{aligned}$$

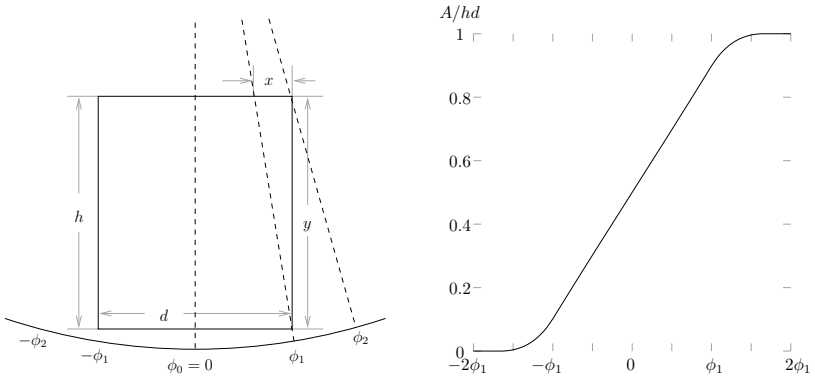
The first part of the guide to open is a triangular corner with width x and height $y \le h$, which is similar to the triangle above the guide with width $d/2 - x$ and height $r - h$. Solving for $\tan\phi$ gives an area

$$A_{\mathrm{tri}}(\phi) = \frac{xy}{2} = \frac{\tan|\phi|}{2}\left(\frac{d/2}{\tan|\phi|} - (r-h)\right)^2,$$

giving $A_{\mathrm{tri}}(\phi_2) = 0$, as desirable, and $A_{\mathrm{tri}}(\phi_1) = h^2 d/4r$. The area of a trapezoid between ϕ_0 and ϕ is

$$A_{\mathrm{trap}}(\phi) = h \cdot (r - h/2)\tan\phi,$$

which is nearly linear in ϕ. It will be convenient for talking about chopper phasings below to know that the transition from fully closed to fully open (or vice-versa) lasts for time $2t_2$, where $t_2 = \phi_2/2\pi\nu$. For any angle ϕ of the



(a) (b)

Figure 4.1: Chopper edge position and the exposed fraction of a guide with area $h \times d$. For convenience here we take r to be the distance from the bottom of the guide to the center of the wheel, rather than the radius of the wheel itself. The FnPB will have $h = 12\,\mathrm{cm}, d = 10\,\mathrm{cm}$, and $r = 29.5\,\mathrm{cm}$, corresponding to $\phi_2 = 15.9°$. (a) The geometry of the chopper sweeping across the guide. (b) The open area of the guide as a function of ϕ.

open/closed boundary, the open area of the guide is

$$A(\phi) = \begin{cases} 0, & \phi < -\phi_2 \\ A_{\mathrm{tri}}(\phi), & -\phi_2 < \phi < -\phi_1 \\ hd/2 + A_{\mathrm{trap}}(\phi), & -\phi_1 < \phi < \phi_1 \\ hd - A_{\mathrm{tri}}(\phi), & \phi_1 < \phi < \phi_2 \\ hd, & \phi_2 < \phi \end{cases} \tag{4.2}$$

We will also find it convenient to measure times in units of $\nu^{-1} \approx 17\,\mathrm{ms}$, and wavelengths in units of $\lambda_W = h/m_n L\nu = 3.67\,\text{Å}$. In these units,

$$\begin{aligned} t_1 &\approx 0.027\,, \\ t_2 &\approx 0.044\,. \end{aligned}$$

Figure 4.2 shows the usefulness of this unit choice. Neutrons are produced in pulses at times $t = 0, 1, 2, \ldots$. A chopper at x opens at time $f_o = 0$ and closes at $f_c = x/L$. Only neutrons with times of flight $0 \le \tau \le 1$ reach the experiment at L, apart from the "wraparound": neutrons so slow the chopper closes and opens again before they reach x. We will say that this chopper is tuned for window 0. If we wanted our experiment to see neutrons with times of flight $1 \le \tau \le 2$, we would instead open the chopper at $f_o = x/L$. In general a chopper can be tuned to the nth window (n need not be an integer) by opening at

$$f_o = n \cdot x/L. \tag{4.3}$$

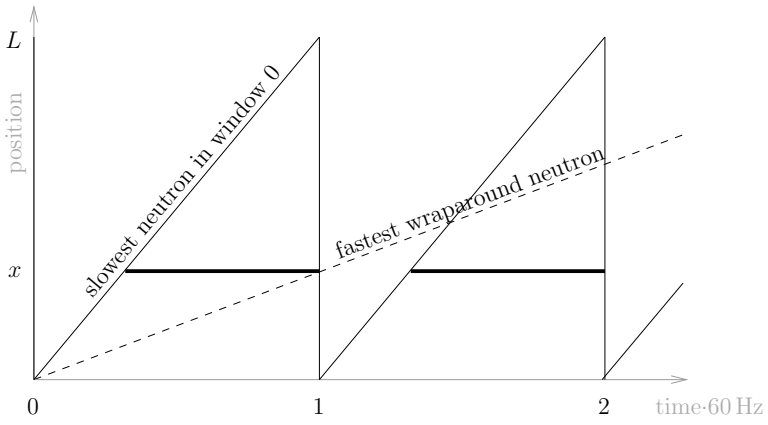


Figure 4.2: A chopper at a distance x from the moderator, with naïve open fraction $w = x/L$ and phased to allow window 0.

A chopper open for a fraction w of a pulse cannot open later than $f_o^{\max} = 1 - w$ without also letting through fast neutrons from a subsequent pulse. This corresponds to a maximum tunable window $n_{\max} = (1 - w) \cdot L/x = L/x - 1$ for a signle chopper with the naïve open fraction $w = x/L$. For example, a chopper 6 m along an 18 m flight path would optimally be open 1/3 of the time and could be tuned to accept neutrons from windows 0, 1, or 2. When tuned to the nth window, wraparound would first appear in window $3 + n$.

A neutron with time of flight τ to the experiment at L will reach a chopper at x at time $\tau x/L$. If we define $\tau_x \equiv \tau x/L - f_o$ modulo ν^{-1} to be the time between the chopper's most recent opening and the neutron's arrival at it, the chopper's transmission is

$$T(\tau) = \begin{cases} A(2\pi\nu \cdot \quad \tau_x \quad)/hd, & 0 \le \tau_x \le w - t_2 \\ A(2\pi\nu \cdot (w - \tau_x))/hd, & w - t_2 \le \tau_x \le 1 - t_2 \\ A(2\pi\nu \cdot (\tau_x - 1))/hd, & 1 - t_2 \le \tau_x \le 1 \end{cases} \tag{4.4}$$

Calling this expression a "transmission" makes the assumption that the neutron flux is distributed evenly across the guide. This assumption does not, in general, hold: gravity brings the neutrons towards the bottom of the guide, and in a curved section more neutrons travel along the outside than along the inside of the curve. These small corrections (only important during the 15% of the time that the chopper is opening or closing) will be estimated using a Monte Carlo simulation. The assumption, which also we will use below, that the total transmission of a system of choppers is the product of the transmission of each chopper requires that the points where a neutron passes through the various choppers are not correlated. Since we have two choppers within a multichannel bender, we can use the invalidity of this second assumption to our advantage.

4.1.1 Frame overlap for various chopper pairs

The FnPB will have chopper housings at 5.5 m, 7.5 m, 9.0 m, and 10.5 m from the moderator. The guide will extend to 15 m, and the $\vec{\mathrm{n}} + \mathrm{p} \to \mathrm{d} + \gamma$ hydrogen target will sit at $L \lesssim 18$ m. Making the assumptions of the previous section, the transmissions defined by equation (4.4) are plotted in Figure 4.3 for choppers at these four locations. Each of the four choppers is half open at the start of the desired window (in the figure, $n = 3$), and half closed at its end. The downstream choppers have better time resolution, but spend more of their time open. Also plotted are the six possible pairwise combinations of choppers. Note that at the beginning and end of each window, in this independent-probability model, the chopper pair transmission is $0.5^2 = 0.25$, rather than zero. If the location of the downstream chopper is x, its finite opening time widens the total transmission window by a time $t_2 L/x$ (albeit at low transmission) at its beginning and end. The pairwise combinations of choppers also admit frame-overlap neutrons with various times of flight. The transmitted time of flight spectrum is symmetric about $\tau = n + \frac{1}{2}$, and simply translates in time as the choppers are rephased for various n.

Examination of the time-of-flight spectrum in Figure 4.3 shows that the optimum run window from an intensity standpoint is somewhere around $n = 0.6$. In a fortunate coincidence, this is near the wavelength of 15 meV neutrons, which contribute only background to the $\vec{\mathrm{n}} + \mathrm{p} \to \mathrm{d} + \gamma$ signal. The experiment will therefore do most of its running at $n = 0.6$ or 0.7. The spectral purity that can be obtained therefore depends on the wraparound neutrons admitted to the experiment. For the product of choppers 1 and 3, at 5.5 m and 9.0 m, the first frame overlap is admitted with time of flight $\tau = n + 4$. The spectrum from a spin filter with $P_3 = 0.75$ (dark blue curve in Figure 4.3), the worst case from a wraparound contamination perspective, is roughly 500 times larger at its peak, near $\tau = 0.8$, than near $\tau = 4.8$. Furthermore, tuning the choppers to the window $n = 3$ as shown in the figure, or even to $n = 3.5$, provides a clean measurement of the neutron spectrum out to $\tau = 4.5$ or so. These observations seem to recommend the use of choppers 1 and 3.

In fact it turns out to be better to use choppers 1 and 2, at 5.5 m and 7.5 m, for three reasons.

Choppers 1 and 2 are both located in the multichannel bender in the upstream portion of the guide. The neutron channels help correlate the horizontal positions where a neutron hits the first and second choppers: no neutrons from the leftmost channel at 5.5 m have crossed to the rightmost channel at 7.5 m. This correlation means the window widening due to the finite chopper opening time can be reduced by having choppers 1 and 2 counterrotate; the effect is less pronounced between choppers 1 and 3. In section 4.2.1 we find that counterrotation reduces the open and close times for choppers 1 and 2 by about 20%.

Second, the simulation indicates that a slight figure-of-merit gain can be had by opening the choppers wider than x/L. With choppers 1 and 3, the extra width introduces a new frame-overlap window at $\tau = n + 3$; with choppers 1

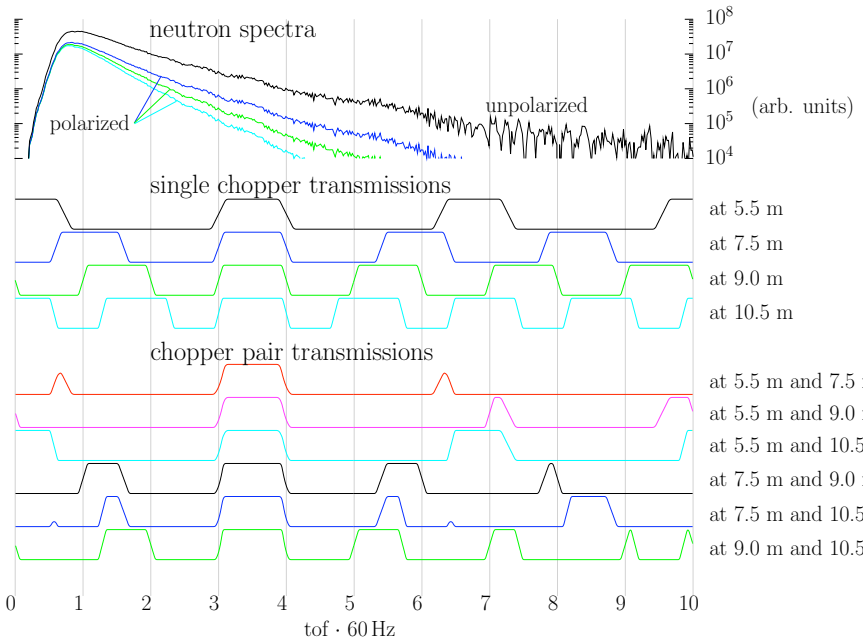


Figure 4.3: Neutron transmission by the guide and its choppers. Uppermost are neutron time of flight spectra at the experiment as calculated using McStas. Polarized spectra were obtained as described in section 4.2.2, with $P_3 = 0.75, 0.50, 0.25$. The single chopper transmissions defined in equation (4.4), each with range $[0, 1]$, are plotted for the four FnPB chopper housing positions. Pairwise chopper transmissions are simply products of the single transmissions. Choppers have the naïve opening widths for an 18 m guide and are tuned to open for window $n = 3$.

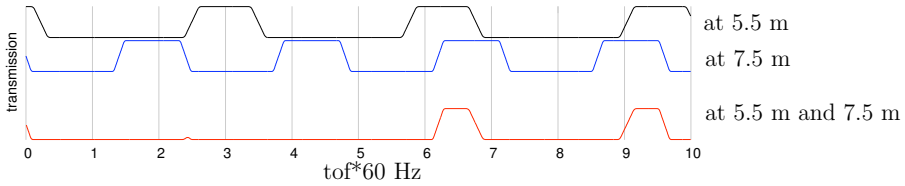


Figure 4.4: A phasing of choppers 1 and 2 ($n = 6.2$, chopper 1 offset by $-3t_2$) permitting a clean spectrum measurement out to 25 Å; compare to Figure 4.3. The contamination of a few percent from $\lambda = 2.2\lambda_W$ can be reduced slightly, but not quite eliminated. However it is present in only a small number of time bins.

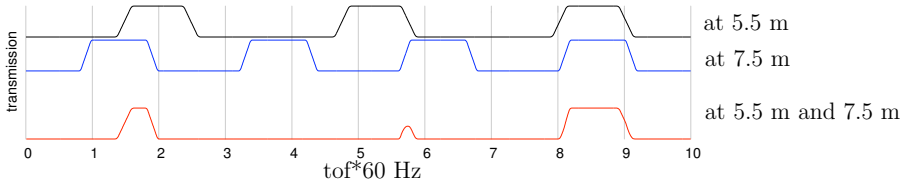


Figure 4.5: A phasing of choppers 1 and 2 ($n = 0.9$, chopper 1 offset by $+4t_2$) permitting the measurement of beam-on pedestal data. Note the differing time resolutions of the upstream and downstream choppers.

and 2, the window at $\tau = n + 3.2$ is widened a bit, but no new windows are introduced.

Most importantly, it is possible to make a precision measurement of the spectrum using choppers 1 and 2. Imagine, in Figure 4.3, opening the 5.5 m chopper at $n = 2.5$, leaving the 7.5 m chopper at $n = 3$ as shown. This dephasing eliminates the fast frame overlap (with $\tau = 0.6$ in the figure), permitting a measurement of the spectrum out to $\tau = 4.5$ or so. Such a measurement includes the frame overlap present during the normal run window with $n \approx 0.7$. By measuring the $\tau = 4.5$ contamination, a few percent of the polarized spectrum, to a few percent, the time of flight spectrum of the normal run window can be known quite well. Such a chopper phasing is shown in Figure 4.4, permitting a (nearly) clean measurement out to $7\lambda_W \approx 25$ Å. Figure 4.5, similarly, shows a chopper phasing that reverses this trick and permits the measurement of beam-on pedestal data, with no contamination in the first part of the data window ($1.0 < \tau < 1.5$) from neutrons faster than $8\lambda_W \approx 29$ Å.

4.1.2 Frame overlap for various opening angles

In addition to the multiple-window frame overlap discussed above, there will also be either frame overlap or dead time at the beginning and end of each

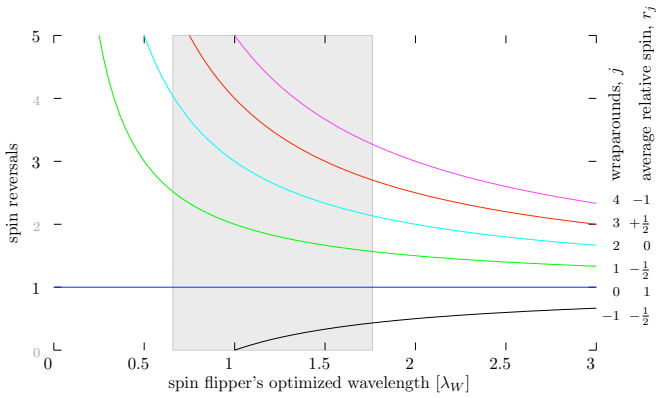


Figure 4.6: Number of spin flips for wraparound neutrons. If the spin flipper is tuned for a wavelength window beginning at $n\lambda_W$, neutrons which have wrapped around j times may simultaneously be present in the spin flipper. The frame-overlap neutrons' spins will rotate by $\theta^j_{\mathrm{SF}} = \pi \cdot (1 + \frac{j}{n+t})$. Shown bottom to top are these curves for $j = -1$, contamination by too-fast neutrons; $j = 0$, for which the spin flipper is correctly tuned; and $j = 1, 2, 3, 4$, long-wavelength overlap. If the spin flipper is tuned to $n = 1$, every wraparound pulse is either flipped (θ_{SF}/π odd) or unflipped (θ_{SF}/π even). The shaded area is the probable spin flipper operating window at $n = 0.65$; note that the spin flipper, as an upstream component, has a wavelength bandwidth larger than λ_W.

window, due to the choppers' finite open and close time. This overlap can be tuned by adjusting the chopper open fractions, or equivalently by moving the experiment to a different L. An optimal chopper open fraction tuning will maximize the (signed) integrated figure of merit $N\langle P\rangle^2$, where N is the number of neutrons and $\langle P\rangle$ their average polarization in the target at a particular instant, as discussed in section 4.3.

The only $\vec{\mathrm{n}} + \mathrm{p} \to \mathrm{d} + \gamma$ component sensitive to energy differences among long-wavelength neutrons is the spin flipper (SF). If the SF has a length δ (at LANSCE $\delta \approx 30\,\mathrm{cm}$), a neutron with time of flight $\tau = n/\nu$ will dwell in it for $t_{\mathrm{SF}} = \tau\delta/L$. In that time the neutron spin rotates by an angle $\theta_{\mathrm{SF}} = \omega_{\mathrm{SF}} t_{\mathrm{SF}}$. If the spin flipper is optimally tuned, its frequency is $\omega_{\mathrm{SF}} = \pi/t_{\mathrm{SF}} = \pi L\nu/n\delta$. In this case a singly wrapped around neutron, with time of flight $\tau^1 = (n+1)/\nu = (1 + n^{-1})\tau$, will rotate by

$$\theta^1_{\mathrm{SF}} = \pi \cdot (1 + n^{-1}). \tag{4.5}$$

We want to open our choppers somewhere beyond $\tau = 2/3\nu$, beyond which the SF transmits single-frame-overlapped neutrons unflipped. So we want our choppers to minimize frame overlap: the ideal chopper phasing should accept a wide, but sharply defined, band of wavelengths.

In practice, the spin flipper is continuously tuned to all wavelengths from

the beginning of its frame, $n\lambda_W$, to $(n + L/x_{\mathrm{SF}})\lambda_W$, where the position of the spin flipper along the guide is $x_{\mathrm{SF}} < L$. At some offset t (where $0 < t < L/x_{\mathrm{SF}}$) from the start of the window at n, a neutron which has wrapped around j times will rotate by angle

$$\theta^j_{\mathrm{SF}} = \pi \cdot \left(1 + \frac{j}{n+t}\right)$$

corresponding to a spin-flip efficiency

$$\epsilon^j = \cos\theta^j_{\mathrm{SF}} = -\cos\frac{j\pi}{n+t}. \tag{4.6}$$

Some values for θ^j_{SF} are plotted in Figure 4.6.

However, wraparound neutrons contribute their polarizations differently because the spin flipper is only on for the $\downarrow$ pulses in the spin sequence

$$\uparrow\downarrow\downarrow\uparrow\downarrow\uparrow\uparrow\downarrow\,.$$

The polarizations of these pulses, for a particular neutron wavelength, are therefore multiplied by

$$1\,\epsilon\,\epsilon\,1\,\epsilon\,1\,1\,\epsilon$$

where ϵ is the spin flipper efficiency. If the polarization P is fixed over the sequence, the average polarization is then

$$\langle P\rangle = P \cdot \frac{1-\epsilon}{2}.$$

The average relative spin r_j of the j^{th} neighbor in the spin sequence is

j:	0	1	2	3	4	5	6	7	8
r_j:	1	$-\frac{1}{2}$	0	$+\frac{1}{2}$	-1	$+\frac{1}{2}$	0	$-\frac{1}{2}$	1

These factors r_j weight the various $\langle P\rangle$s present in the system, as plotted on the pink curve in Figure 4.9.

The facts that the period of the spin flipper is different from the rest of the system, and that multiply-wrapped neutrons may contribute a positive average polarization signal, make it more difficult to estimate the effects of the spin flipper from this sort of analytic treatment. So we shift to the discussion of the simulation.

4.2 McStas simulation

The McStas simulation was based on the instrument file "Polychromatic.instr" (2005-02-14), with the following adaptations:

- The monochromator crystal was removed, as it will not be used with the NPDG experiment.

- The histogram detectors were replaced with a more general ntuple, as explained below.

- A bug which bypassed the component `shutter_guide_4` was fixed. In McStas 1.8, the only effect of the bug was to shorten the guide and increase transmission by 3%. However, in McStas 1.9.x, all neutrons were lost past this point due to stricter checks on the direction of propagation through the `Guide_gravity` component. Specifically, neutrons were lost when travelling through overlapping parts of adjacent guides because they had to travel backward from the end of the first to the beginning of the second. Even after the bug was fixed, this version lost some neutrons through the curved guides due to implementation as rectangles which intersected at the inner edge. Therefore, McStas 1.8 was used for the final simulation.

- A bug was also fixed in the McStas contributed component definition `He3_cell.comp`. The transmission was multiplied by a factor of one half to account for the initial density of states of an unpolarized beam; however, the initial spin state on the neutron was specified. In the end this component was abandoned in favor of dynamic polarization weights, described below.

A new component `Ntuple.comp` was implemented using the ROOT library for additional flexibility. Standard components along the instrument were extended via the `EXTEND %{ %}` functionality to save the neutron state parameters at the current point in the simulation to an array, which was appended a ROOT ntuple file when the neutron reached the `Ntuple` component at the end of the simulation. The standard McStas state parameters are: position (x,y,z), velocity (v_x,v_y,v_z), time t, and event weight p. In the ntuple, each variable was appended with a component subscript as in Table 4.1. The pathlength d and chopper phases f (cw) and g (ccw) were also booked for certain components as explained later. This feature provided two important capabilities:

- The ability to plot correlations between arbitrary neutron parameters at arbitrary components. An example is shown in Fig. 4.7.

- The ability to implement active components as ntuple cuts on the completed simulation saving time in the analysis. This enable detailed studies of counter-rotation of the choppers, and fine-grained optimizations.

One limitation of this scheme was that only neutrons which survived to the end of the guide were booked, so distributions in earlier components were biased by later outcomes. However, proper behavior would have required a major modification of McStas and was irrelevant to the current study. Because the precompiled instrument `C` code could not be compiled with `g++`, which was necessary for linking the ROOT library, the standard method of invocation `mcrun` would not work, and a straightforward `Makefile` was used instead. After running the simulation the output ntuple file `mcstas.root` was histogrammed

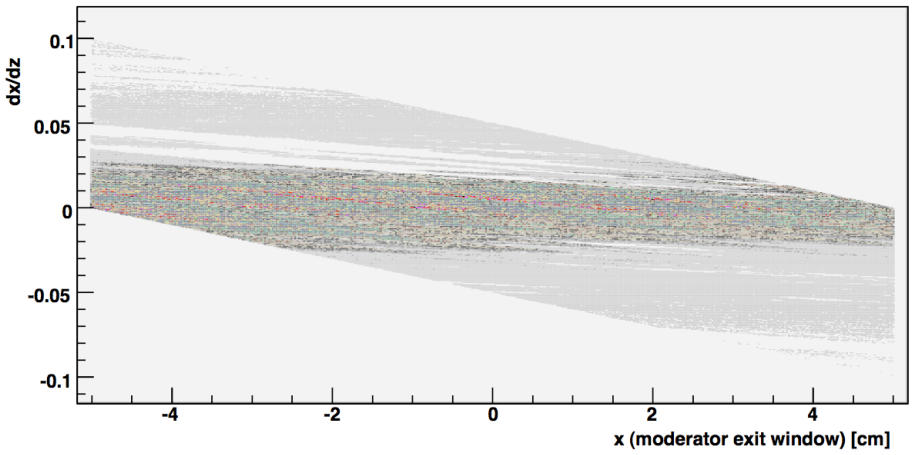


Figure 4.7: Correlation between position and slope in the horizontal (x) direction of neutrons at the source exit window. The 50 cm gap before the first guide is cleanly seen.

and analyzed with various ROOT scripts, or by simple `Draw()` commands in the interactive interpreter.

To verify the beam guide model, the simulation was used to examine the effective distance of each chopper, accounting for moderation times. Since McStas does not record the pathlength, the distance was determined from $t\sqrt{\boldsymbol{v}^2}$. It was found the effective distance of the moderator exit window averaged over the accepted wavelengths 23.7 cm, and that of subsequent components was determined by geometry (Table 4.1). The distance, dominated by the tail, was averaged over events in the nominal SNS time window starting at 15 meV neturons, but was consistent with the complete spectrum, as shown in Fig. 4.8.

Similar to the methods of the analytical investigation, only the neutron guides were included in the McStas simulation. The effect of variations in the active components (choppers, ^{3}He spin filter, RFSF cavity, and LH_2 target) were analyzed dyamically by weighting or placing cuts (weight of 1 or 0) on events after the simulation was complete. This could be implemented very efficiently within the ROOT environment. The cuts associated with each component are described in the subsections below. The transmission of each component is shown on the neutron spectrum in Fig. 4.9, as well as the resulting neutron polarization.

4.2.1 Choppers

The choppers were implemented by the chopper phase variables f_i and g_i defined for the chopper i rotating clockwise or counter-clockwise, respectively (looking downstream), as follows: At time $t = 0$, paint a dot P on the chopper at the center of the beam guide. The dot rotates with the chopper at angular velocity

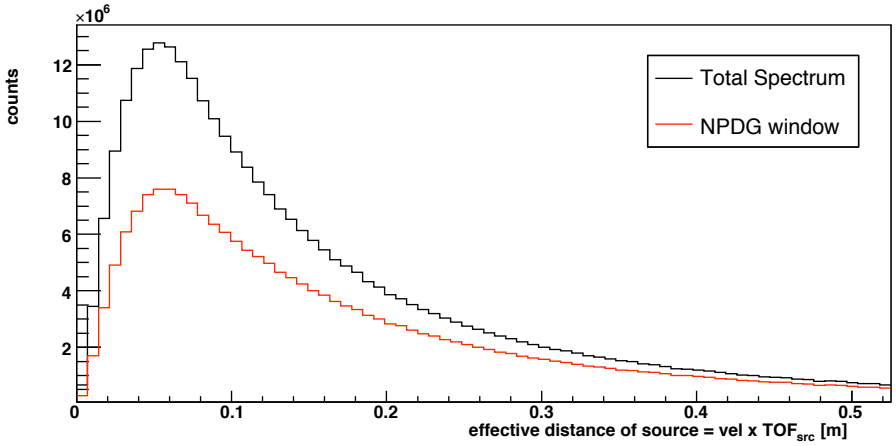


Figure 4.8: Distribution of $d = vt$ at the moderator exit window, for all neutrons, and the NPDG frame overlap window.

Table 4.1: Effective distance of active components in the neutron guide, used to calculate the naïve chopper phase for 15 meV neutrons, and the opening angle. The placement of NPDG components was based on the current setup an LANL. Alternative distances and phases based on the target placed at 18 m are also included.

		current setup			target at 18 m		
component		dist	phase	open	dist	phase	open
source exit	d_0	0.24 m					
chopper 1	d_1	5.73 m	73°	125°		73°	113°
chopper 2	d_2	7.69 m	98°	168°		98°	152°
chopper 3	d_3	9.18 m	117°	201°		117°	181°
chopper 4	d_4	10.68 m	136°	234°		136°	211°
end of guide	d_5	15.19 m					
RFSF cavity	d_{sf}	15.88 m	200°		17.70 m	226°	
LH2 target	d_{h2}	16.42 m			18.24 m		

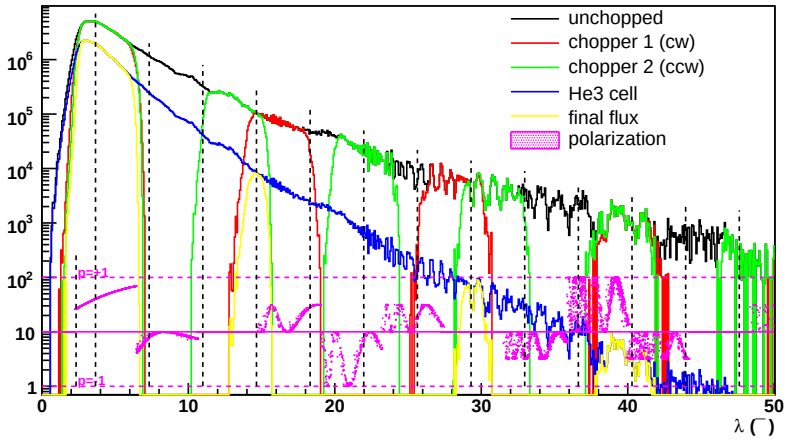


Figure 4.9: The SNS neutron spectrum at the end of the guide, and transmitted through Choppers 1 and 2, the ^{3}He cell. Also shown the final polarization in the LH_2 target. The vertical lines mark the frame overlap windows, and 15 meV neutrons.

$\omega = 360° \cdot 60\,\mathrm{Hz}$ until time t_i when the neutron crosses the chopper plane at the point Q. The chopper phase, defined as the positive angle between P and Q, depends on the rotation of the chopper ($\phi_P = \omega t_i$) and the crossing angle the neutron (ϕ_Q, defined positive clockwise of beam center) by $f_i = \phi_P - \phi_Q$ and $g_i = \phi_P + \phi_Q$, subject to $0° \le f_i, g_i < 360°$. With this definition of phase, the cut for a chopper of opening phase ϕ_i and opening angle η_i is simple:

$$\phi_i < (f_i \text{ or } g_i) < \phi_i + \eta_i \mod 360°. \tag{4.7}$$

To investigate the possibility of achieving better roll-off times by counter-rotating the choppers, the correlations in neutron crossing angles are plotted for each chopper pair in Fig. 4.10a. Some degree of correlation is seen between all pairs, although it is the strongest for adjacent closer choppers, especially choppers 1 and 2, which are separated by a guide with five horizontal channels. The opening and closing roll-off times were calculated by plotting the derivative of the chopper [pair] acceptance function and fitting the Gaussian width of each end, as shown in Fig. 4.10b. The opening and closing widths were plotted as a function of the phase between each chopper pair, normalized to the naïve phases in Fig. 4.10c. For co-rotating choppers in either direction, the width was either dominated by either by the first chopper (wider) or second (narrower) depending on which was the limiting factor. For counter-rotating choppers, there was a finely tuned phase where the width had a small minimum due to neutrons being cut off on both sides simultaneously. However, only a factor of 20% was gained due to the fact that the width still depended mainly on the narrower chopper. Again, the direction of each chopper was insignificant.

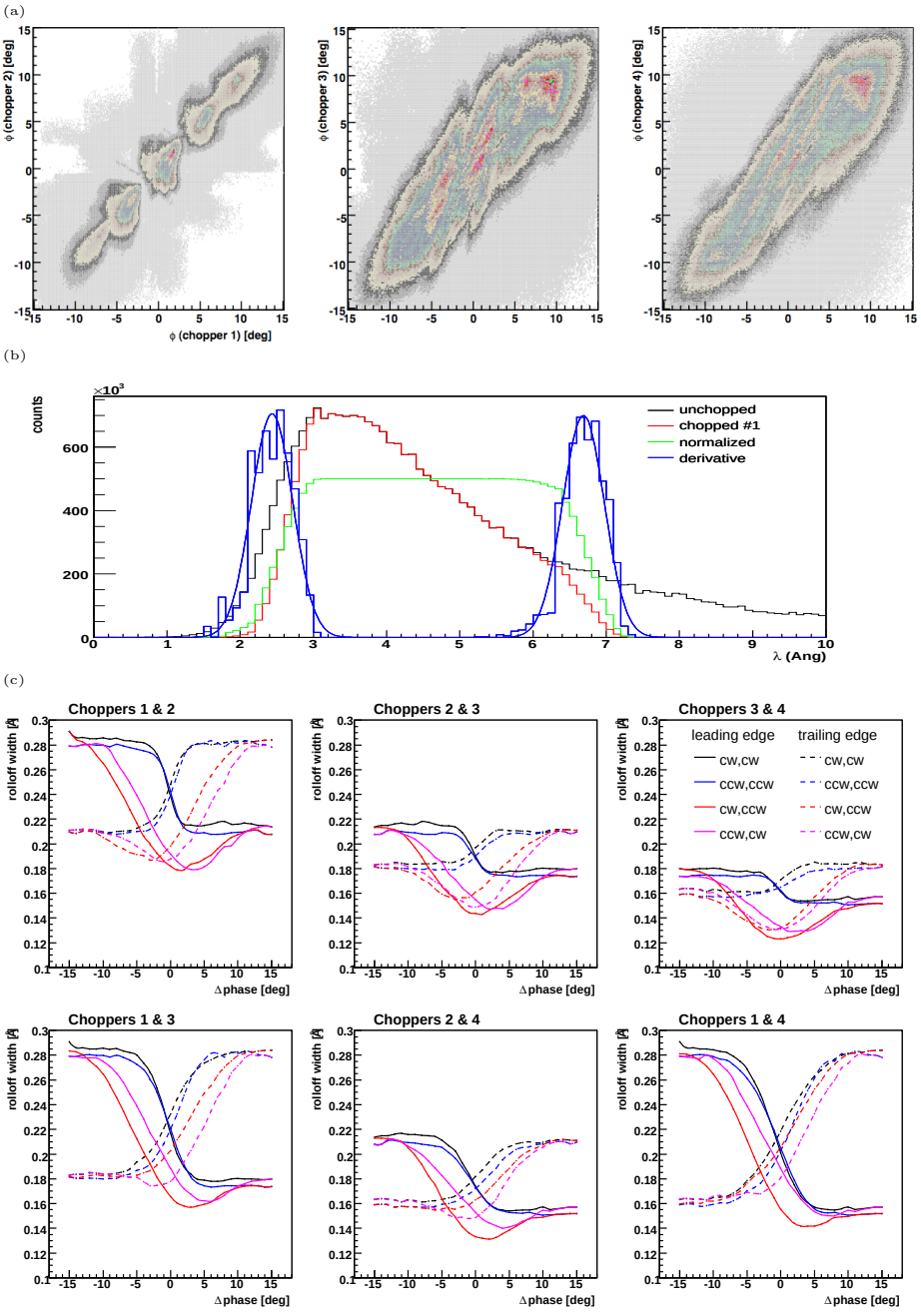


Figure 4.10: Correlations between co- and counter-rotating choppers. (a) Correlation between phase of neutrons between pairs of choppers. (b) Method of calculation of chopper roll-off width in opening and closing times. (c) Chopper roll-off times for pairs of choppers as a function of phase difference between two choppers for all combinations of rotation direction.

4.2.2 ^{3}He spin filter

The transmission of neutrons through polarized ^{3}He gas[23] is highly spin-dependent:

$$T^{\pm} = e^{-nl\sigma(1\mp P_3)}, \tag{4.8}$$

where nl is the ^{3}He areal density (thickness), $\pm P_3$ the ^{3}He polarization in the direction of the neutron spin, and $\sigma \propto 1/v$ the cross section of unpolarized ^{3}He. The transmission of an unpolarized neutron beam through the spin filter is

$$T = e^{-nlk\lambda}\cosh(P_3 nlk\lambda), \tag{4.9}$$

resulting in neutron polarization

$$P = \tanh(P_3 nlk\lambda) = \sqrt{1-(T/T_0)^2}, \tag{4.10}$$

where $k = \sigma_0 v_0 m_n/h = 0.07855/\mathrm{Amg{\cdot}cm{\cdot}\AA}$. The cross section is $\sigma_0 = 5327\,\mathrm{b}$ at the thermal velocity $v_0 = 2200\,\mathrm{m/s}$, and the Amagat density is $\mathrm{Amg} = N_A/V_0$ in terms of Avagadro's number N_A and the standard molar volume V_0. We used the values $nl = 4\,\mathrm{Amg{\cdot}cm}$ and $P_3 = 0.60$ for this study.

4.2.3 Spin flipper cavity

In the moving frame of the RFSF magnetic field the spin precesses at a constant frequency about the perpendicular spin-flipping B-field proportional to the RF amplitude A during the time Δt the neutron is in the cavity. Thus $A\Delta t$ should be constant for each neutron. This condition can be achieved for a single pulse time window, but wrap-around neutrons will be affected by the amplitude of the next window. Hence the efficiency of the RFSF is

$$\epsilon_{\mathrm{sf}} = \cos\left(\frac{\pi\, d_{\mathrm{sf}}}{v_z[t_{\mathrm{sf}}]_{\phi_{\mathrm{sf}}}}\right), \tag{4.11}$$

where $[t_{\mathrm{sf}}]_{\phi_{\mathrm{sf}}} = t_{\mathrm{sf}} - nT_{\mathrm{pulse}}$ is the time of flight (TOF) of the neutron with respect to the current RFSF time window, subject to $\phi_{\mathrm{sf}} \le \omega[t_{\mathrm{sf}}]_{\phi_{\mathrm{sf}}} < \phi_{\mathrm{sf}}+360°$. Note that $\epsilon_{\mathrm{sf}} = -1$ corresponds to an exact spin flip. The RFSF distance $d_{\mathrm{sf}} = 15.868\,\mathrm{m}$ was tuned in the simulation for a maximal efficiency of $\epsilon_{\mathrm{sf}} = -0.999368$. The only free parameter to optimize for the RFSF is the phase ϕ_{sf}.

The raw RFSF efficiency must be averaged over the spin sequence ($\uparrow\downarrow\downarrow\uparrow\downarrow\uparrow\uparrow\downarrow$). This involves two considerations: first, in the case of spin up, the RFSF is 100% efficient because it is off. Second, the average relative spin ϵ_n of the n^{th} neighbour in the spin sequence is: $\epsilon_0 = 1$, $\epsilon_1 = -\frac{1}{2}$, $\epsilon_2 = 0$, $\epsilon_3 = \frac{1}{2}$, $\epsilon_4 = -1$, which also abates the effect of wrap-around neutrons. Thus the final efficiency is $\epsilon = \epsilon_n \cdot (1+\epsilon_{\mathrm{sf}})/2$, where n is the number of time-frames away from the tuned window.

[23] This analysis was carried out prior to consideration of a supermirror polarizer on the FnPB.

In later simulations, a strict RFSF efficiency was used to strongly penalize wrap-around neutrons, such that all untuned neutrons were assumed to have the wrong polarization state. They were assigned $\epsilon = -1$, and TOF bins with $\langle p \rangle < 0$ were set to 0 to simulate a software cut on wrap-around neutrons. Results are given for both the physical and strict FOM. Investigations were also made with stronger penalties on wrap-around neutrons, for example, $\epsilon = -10$.

4.2.4 Liquid hydrogen target

The only effect considered of the para-hydrogen target was to depolarize neutrons with higher energy than $\Delta E = 15\,\mathrm{meV}$, the energy difference between ortho- and para-hydrogen. This was implemented with a step function from 0 to 1 at ΔE.

4.3 Chopper and spin flipper optimization

Armed with the McStas ntuple and component cuts, we proceed to do a full optimization. The figure of merit (FOM) is discussed in detail in the first section, followed by results or various optimizations.

4.3.1 Statistics of the asymmetry

In optimizing the choppers, it is important to properly take into account the effect of wrongly polarized neutrons. We devote this subsection to a derivation of the figure of merit.

The weighted average of quantities x_1 and x_2 is defined as

$$\langle x_i \rangle_{w_i} \;\equiv\; x_1 \pm \delta x_1 \,\langle + \rangle\, x_2 \pm \delta x_2 \;\equiv\; \frac{w_1 x_1 + w_2 x_2}{w_1 + w_2} \pm \frac{\sqrt{w_1^2\,\delta x_1^2 + w_2^2\,\delta x_2^2}}{w_1 + w_2}. \quad (4.12)$$

The weight w_i should be proportional to the number n of measurements of equal uncertainty. For Poisson statistics $\delta\bar{x} = 1/\sqrt{n}$, so in general, $w_i \equiv \delta x_i^{-2}$. In this case, the weighted average $\vec{x} \sim x \pm \delta x$, where $\delta x^{-2} = w = w_1 + w_2$, can be represented as the vector sum

$$\vec{x} = \vec{x}_1 + \vec{x}_2 \qquad \text{where} \qquad \vec{x}_i \equiv (w_i, w_i x_i) = \frac{(1, x_i)}{\delta x_i^2} \;\sim\; x_i \pm \delta x_i. \quad (4.13)$$

The experimental asymmetry has the standard definition and uncertainty

$$A_{\mathrm{exp}} = \frac{n^+ - n^-}{n^+ + n^-}, \qquad \delta A^2_{\mathrm{exp}} = \frac{4 n^+ n^-}{(n^+ + n^-)^3} = \frac{1 - A^2}{n} \approx \frac{1}{n}. \quad (4.14)$$

Note that the weighted average of asymmetries has the simple form

$$A^1_{\mathrm{exp}} \,\langle + \rangle\, A^2_{\mathrm{exp}} = \frac{n_1 A^1_{\mathrm{exp}} + n_2 A^2_{\mathrm{exp}}}{n_1 + n_2} = \frac{n^+ - n^-}{n^+ + n^-} = A_{\mathrm{tot}}, \quad (4.15)$$

where $n^+ = n_1^+ + n_2^+$ and $n^- = n_1^- + n_2^-$.

The physics asymmetry is independent of polarization: $A_{\rm exp} = pA_{\rm phy}$. The weight $w = \delta A_{\rm phy}^{-2} = p^2 \delta A_{\rm exp}^{-2} = p^2 n$ forms the standard FOM for polarization experiments. Physics asymmetries from a known set of polarizations can be combined according to the above weighted average $\langle A^i_{\rm phy}\rangle_{w_i}$, to get the combined FOM $w = \sum_i w_i$ without dilution even for opposite polarizations, since each polarization is divided out individually.

However, if any of the individual polarizations p_i or asymmetries $A^i_{\rm exp}$ are unknown, the best one can do is to assume that $A^i_{\rm phy}$ is constant in each dataset:

$$A^1_{\rm exp} \ \langle + \rangle \ A^2_{\rm exp} \ \equiv \ \frac{n_1 A^1_{\rm exp} + n_2 A^2_{\rm exp}}{n_1 + n_2} \ = \ \frac{n_1 p_1 + n_2 p_2}{n_1 + n_2} A_{\rm phy} = p_1 \langle + \rangle p_2 \ A_{\rm phy}, \tag{4.16}$$

or $A_{\rm phy} = \langle A_{\rm exp}\rangle / \langle p \rangle$, resulting in the figure of merit

$$w = \langle p \rangle^2 n = \frac{n_1 w_1 + n_2 w_2}{n_1 + n_2} + p_1 p_2 \frac{n_1 n_2}{n_1 + n_2} = w_1 + \frac{2p_1}{p_2} w_2 + \mathcal{O}\left(\frac{n_2}{n_1}\right). \tag{4.17}$$

In this case opposite polarization degrades the FOM as expected.

The NPDG asymmetry and polarization can each be measured independently in each TOF bin; but within a single time bin, the asymmetry of wrap-around neutrons can not be separated. Thus the final FOM is a combination of the two above cases: $w = \sum_i w_i = \sum_i \langle p \rangle_i^2 n_i$, where i runs over each TOF bin. The physics asymmetry is $A_{\rm phy} = \langle A^i_{\rm phy} \rangle$, where $A^i_{\rm phy} = A^i_{\rm exp} / \langle p \rangle_i$. One must simulate $\langle p \rangle_i$ to include wrap-around neutron, and the uncertainty of this simulation is another reason to minimize wrap-around. In Fig. 4.11a, the histograms H_n (black) and H_{pn} (magenta), are used to calculate $H_{p^2 n} = H^2_{pn}/H_n$ (blue), which is integrated to get the final FOM. Individual contributions to H_{pn} from wrap-around neutrons are shown in green (positive) or red (negative).

4.3.2 Optimization procedure and results

The optimization of chopper and RFSF parameters is illustrated in Fig. 4.11b for the single parameter $\phi_{\rm sf}$ without any choppers. The maximum FOM was 4.77 in arbitrary units with negligible variation over $\phi_{\rm sf} = 206^\circ \pm 5^\circ$. For the strict RFSF efficiency ($\epsilon_{\rm sf} = \pm 1$), the maximum FOM was 3.06 at $\phi_{\rm sf} = 208^\circ$. The contributions from wrap-arround for the and naïve RFSF phases is shown in Fig. 4.13. For choppers 1 and 2 with naive opening angles, the standard FOM is 5.58.

For the standard case of two choppers, five parameters were optimized by performing sequential line optimizations on $\phi_{\rm sf}$, $\phi_1 + \phi_2$, $\eta_1 + \eta_2$, $\phi_1 - \phi_2$, $\eta_1 - \eta_2$, respectively, keeping the other values fixed, and repeating the procedure for ~ 8 iterations until the line optimizations converge. The results of optimizing

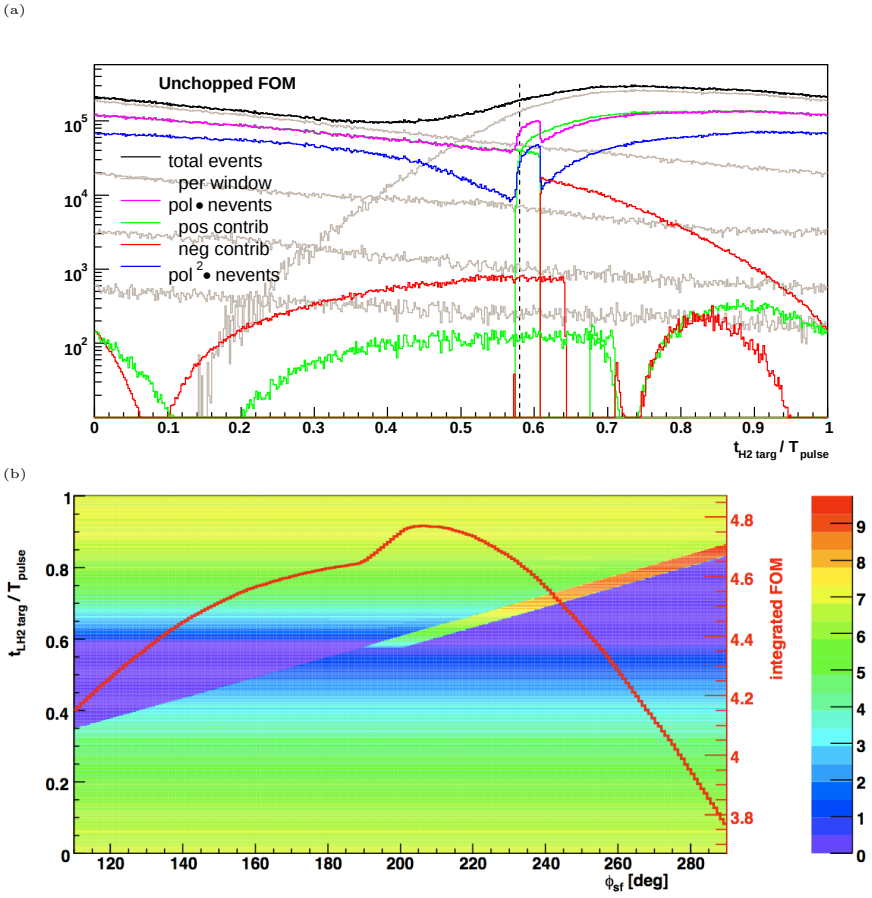


Figure 4.11: Histograms of the figure of merit. (a) Histogram of the FOM for no choppers, explained in the text. (b) The same histogram as a function of RFSF phase ϕ_{sf}. The integral of each vertical slice (total FOM) is also plotted.

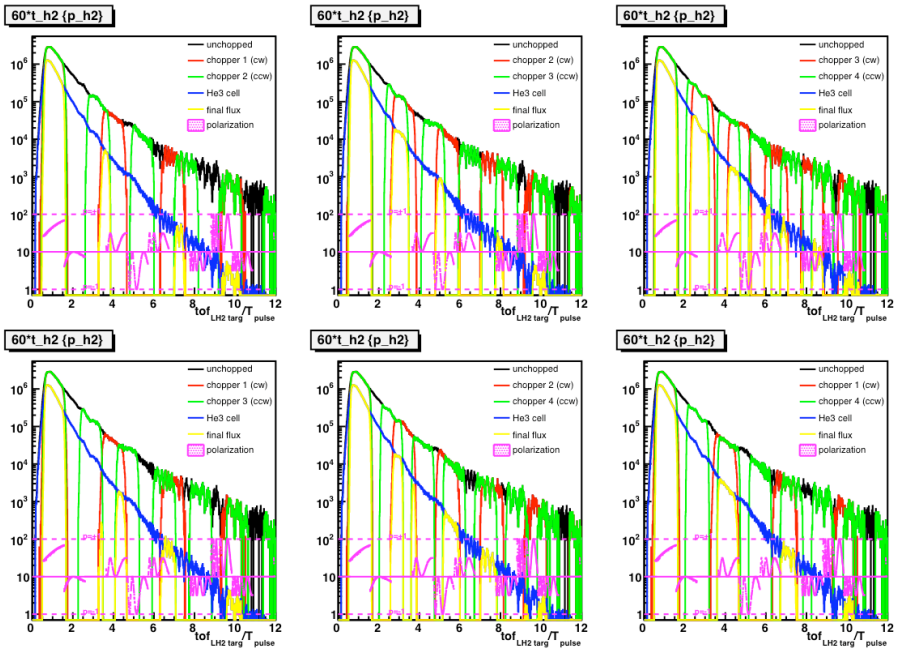


Figure 4.12: Chopped neutron spectrum and polarization, vs. wavelength, for each chopper pair.

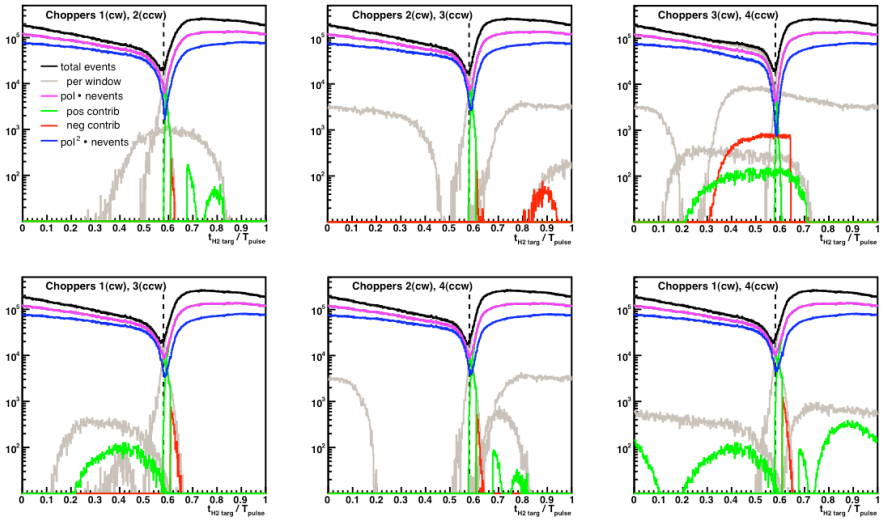


Figure 4.13: The corresponding wrapped spectrum with $\langle p \rangle n$ and $\langle p \rangle^2 n$ to calculate the FOM.

various chopper pairs and rotations are summarized in Table 4.2. The optimized phases listed are all relative to the naïve angles.

Optimizations were done for all chopper pairs, using both the standard and strict RFSF efficiency described above. For the strict optimization, the standard FOM is also reported for direct comparison. The optimizations were repeated for choppers 1 and 2, for all combinations of rotations to conclude the investigation of counter-rotating the choppers. Finally, the McStas simulation was repeated with the LH2 target centered at 18 m from the moderator exit window and the RFSF at same distance from the target. Again, the FOM reported was recomputed after the optimization using the standard configuration for direct comparison. Optimization with an even stricter penalty on wrap-around neutrons ($\epsilon = -10$) was also investigated. For the unchopped spectrum, the wrap-around neutrons dominated to make the FOM identically zero, but for two choppers, the opening angles were about 5° smaller.

4.4 Recommendations

Because of a coincidence in position of the frame-overlap window starting at 15 meV neutrons and the peak of the SNS wavelength spectrum, and the sharp drop-off in neutron flux at higher wavelengths, the figure of merit has very little dependence on which choppers were used, or their opening angles. All of the optimization occurs in the tails which are an order of magnitude lower in flux. Also, most wrap-around neutrons are almost depolarized, and some are actually polarized in the same direction as the primary window. In fact, using the naïve opening angles for choppers 1 and 2 gives only 13% better performance than using no choppers at all, and optimization of these two choppers phases yields only a 3.4% gain. Chopper pairs 1&4, 1&3, and 1&2 had the best performance, but there is only 3% difference between the best and worst pair. Similarily there is only a 1% effect from counter-rotation of the choppers.

For the same reasons, the optimized opening angles were significantly larger than the naïve estimates. Penalizing the wrap-around neutrons leads to slightly stricter optimization conditions, resulting in opening angles about 7° smaller, but only a 1% effect on the standard FOM. There is also a small effect where the experiment was placed relative to the end of the neutron guide. Placing the experiment 1.8 m farther downstream narrows the opening angles by approximately the difference in the naive angles: 12° and 16° for choppers 1 and 2, respectively, which a 6% or 10% drop in the FOM for the standard or strict optimization, respectively.

The choppers which are closer to the source have larger opening and closing times, but offer more versatility because their opening angles are much smaller. It is preferable to use the smaller opening angles, because they are more restrictive and will not pass bad neutrons in other conditions. For the standard configuration, the optimized opening angles are 143° and 183°, for choppers 1 and 2, respectively. However, one should use the optimization of the configuation farthest from the source, as it gives the smallest opening angles, which will

Table 4.2: Optimization results for conditions specified in the text. In this table C_1, C_2 show the position and direction of the first and second chopper. The η are the chopper opening angles, and the ϕ are the phases where the choppers open and the spin flipper recycles. Tabulated are the differences between the optimized η, ϕ and the naïve values given in Table 4.1. For the 18 m case, the FOM was optimized for 18 m, but then recalculated using the 16 m geometry for comparison in this table. We recommend the 18 m results.

	standard opt.					std.	strict opt.					strict	std.
C_1,C_2	$d\phi_{\mathrm{sf}}$	$d\phi_1$	$d\eta_1$	$d\phi_2$	$d\eta_2$	FOM	$d\phi_{\mathrm{sf}}$	$d\phi_1$	$d\eta_1$	$d\phi_2$	$d\eta_2$	FOM	FOM
current config.: ϕ_{sf}=200°, ϕ_0={73°,98°,117°,136°}, η_0={125°,168°,201°,234°}													
—	6°					4.77	8°					3.06	4.77
1^+	5	-1	8			5.63	7	-1	1			5.44	5.59
2^+	6	2	7			5.62	8	3	-2			5.24	5.57
3^+	9	6	6			5.55	10	9	-6			5.01	5.50
4^+	9	9	5			5.46	16	15	-10			4.66	5.39
$1^+, 2^-$	9	-3	18	-3	15	5.77	8	-3	11	-5	9	5.64	5.70
$2^+, 3^-$	10	-1	17	-3	17	5.73	12	1	8	-3	7	5.40	5.66
$3^+, 4^-$	10	3	15	-2	20	5.65	13	8	3	-3	9	5.16	5.56
$1^+, 3^-$	9	-4	20	-2	14	5.79	9	-4	12	-3	6	5.66	5.73
$2^+, 4^-$	10	-1	18	-1	17	5.76	10	0	9	-2	5	5.49	5.69
$1^+, 4^-$	10	-5	23	0	15	5.80	9	-5	15	-2	5	5.63	5.74
$1^+, 2^+$	7	-5	24	2	8	5.71	8	-3	14	2	-1	5.58	5.66
$1^-, 2^-$	7	-7	23	1	7	5.71	8	-4	13	0	-1	5.58	5.66
$1^+, 2^-$	9	-3	18	-3	15	5.77	8	-3	11	-5	9	5.64	5.70
$1^-, 2^+$	9	-6	18	-1	15	5.77	9	-5	11	-2	8	5.64	5.66
target at 18 m: ϕ_{sf}=226°, ϕ_0={73°,98°,117°,136°}, η_0={113°,152°,181°,211°}													
$1^+, 2^-$	8	-3	19	-1	15	5.40	8	-3	11	-3	6	5.18	5.20

still not pass wrap-around neutrons in the case of closer configurations. Therefore, we recommend using choppers 1 and 2 with the optimized opening angles of 132° and 167°, respectively.

Conclusion

In this dissertation we have presented a measurement of the parity-violating asymmetry A_γ in the radiative capture of polarized cold neutrons in parahydrogen. Thanks to the quantum numbers of the two-nucleon system, this geometrical effect is most sensitive to a parity mixing interaction that also mixes strong isospin; thanks to Cabibbo suppression of d-s quark mixing, weak interactions that conserve strangeness but change isospin are dominated by neutral currents. While the nucleon-nucleon neutral weak coupling may larger asymmetries in complicated nuclei, the $\vec{\mathrm{n}} + \mathrm{p} \rightarrow \mathrm{d} + \gamma$ asymmetry is a chance to measure the coupling without complications from nuclear structure.

The uncertainty on the result we report, $A_\gamma = (1.8 \pm 1.8) \times 10^{-7}$, is large compared with the theoretical prediction $A_\gamma \sim 0.5 \times 10^{-7}$. However we argue that this uncertainty is dominated by statistics, rather than systematics. We show that, with the increased neutron flux at the Spallation Neutron Source, the apparatus we describe here will measure A_γ with precision $\sim 0.1 \times 10^{-7}$.

Bibliography

The following references appear often enough to warrant abbreviations:

DDH Desplanques, Donoghue, and Holstein 1980

ENSDF the Evaluated Nuclear Structure Data File, Tuli et al. (online)

NDB the Neutron Data Booklet, Dianoux and Lander 2003

NWC the Nuclear Wallet Cards, Tuli 2005

PDG the Review of Particle Physics, Yao et al. 2006

Y Abov, P A Krupchitsky, and Yu A Oratovsky. On the existence of an internucleon potential not conserving spacial parity. *Physics Letters*, 12(1):25–26, Sep 1964. doi: 10.1016/0031-9163(64)91162-X. URL http://dx.doi.org/10.1016/0031-9163(64)91162-X. 5

E. G. Adelberger and W. C. Haxton. Parity violation in the nucleon-nucleon interaction. *Annual Review of Nuclear and Particle Science*, 35:501–558, 1985. 11

E. G Adelberger, M. M Hindi, C. D Hoyle, H. E Swanson, R. D Von Lintig, and W C Haxton. Beta decays of 18ne and 19ne and their relation to parity mixing in 18f and 19f. *Physical Review C*, 27(6):2833–2856, Jun 1983. doi: 10.1103/PhysRevC.27.2833. URL http://prola.aps.org/abstract/PRC/v27/i6/p2833_1. 11

Bas B. Van Aken, Jean-Pierre Rivera, Hans Schmid, and Manfred Fiebig. Observation of ferrotoroidic domains. *Nature*, 449(7163):702, Oct 2007. doi: doi:10.1038/nature06139. URL http://www.nature.com/nature/journal/v449/n7163/full/nature06139.html. 11

Kurt Alder, Berthold Stech, and Aage Winther. Parity nonconservation in decay. *Physical Review*, 107(3):728–736, Aug 1957. doi: 10.1103/PhysRev.107.728. URL http://prola.aps.org/abstract/PR/v107/i3/p728_1. 9

Libertad Barron-Palos, D. Bowman, C. Crawford, M. Dabagian, R. Mahurin, J. Mei, H. Nann, S. Penttila, A. Salas, and M. Snow. Determination of the ortho-para fraction in the NPDGamma LH_2 target at LANSCE. Technical Report 28, NPDGamma, 2007. URL http://sns.phys.utk.edu/npdg/technotes/. 30

G Barton. Notes on the static parity non-conserving internucleon potential. *Nuovo Cim*, 19 (3):512–527, Feb 1961. doi: 10.1007/BF02733247. URL http://www.springerlink.com/content/k406p20q21n37400/?p=f40daecefc1741898f4c70722572522c&pi=4. 7

C D Bass et al. Measurement of the parity-violating neutron spin rotation in 4he. *Journal of Research of the National Institute of Standards and Technology*, 110(3):205–208, Jun 2005. 12

A Benvenuti, D Cline, F Messing, W Ford, R Imlay, T. Y Ling, A. K Mann, D. D Reeder, C Rubbia, R Stefanski, L Sulak, and P Wanderer. Evidence for parity nonconservation in the weak neutral current. *PRL*, 37(16):1039–1042, Oct 1976. doi: 10.1103/PhysRevLett.37.1039. URL http://prola.aps.org/abstract/PRL/v37/i16/p1039_1. 6

A. R Berdoz, J Birchall, J. B Bland, J. D Bowman, J. R Campbell, G. H Coombes, C. A Davis, A. A Green, P. W Green, A. A Hamian, R Helmer, S Kadantsev, Y Kuznetsov, L Lee, C. D. P Levy, R. E Mischke, N. T Okumusoglu, S. A Page, W. D Ramsay, S. D Reitzner, T Ries, G Roy, A. M Sekulovich, J Soukup, G. M Stinson, T. J Stocki, V Sum, N. A Titov, W. T. H Van Oers, R. J Woo, S Zadorozny, and A. N Zelenski. Parity violation in proton-proton scattering at 221 mev. *Phys. Rev. C*, 68(3), Sep 2003. doi: 10.1103/PhysRevC.68.034004. URL http://link.aps.org/doi/10.1103/PhysRevC.68.034004. 12

M Bini, T. F Fazzini, G Poggi, and N Taccetti. Search for the circular polarization of the 1081-kev gamma ray in 18f. *PRL*, 55(8):795–798, Aug 1985. doi: 10.1103/PhysRevLett.55.795. URL `http://prola.aps.org/abstract/PRL/v55/i8/p795_1`. 11

M Bini, T. F Fazzini, G Poggi, and N Taccetti. Experimental limit for the circular polarization of the 1081 kev gamma ray in 18f. *Physical Review C*, 38(3):1195–1206, Sep 1988. doi: 10.1103/PhysRevC.38.1195. URL `http://prola.aps.org/abstract/PRC/v38/i3/p1195_1`. 1, 11

R. J Blin-Stoyle. Parity nonconserving internucleon potentials. *Physical Review*, 118(6):1605–1607, Jun 1960a. doi: 10.1103/PhysRev.118.1605. URL `http://prola.aps.org/abstract/PR/v118/i6/p1605_1`. 5

R. J Blin-Stoyle. Parity-nonconserving internucleon potentials. ii. effects in electromagnetic transitions. *Physical Review*, 120(1):181–189, Oct 1960b. doi: 10.1103/PhysRev.120.181. URL `http://prola.aps.org/abstract/PR/v120/i1/p181_1`. 8, 9, 10

Kimberly Boddy et al. Beam polarization correction for neutron-deuteron scattering cross section. *Bulletin of the American Physical Society*, HAW05:FR.00011, Aug 2005. URL `http://absimage.aps.org/image/MWS_HAW05-2005-020099.pdf`. 20

F Boehm and E Kankeleit. Experimental evidence for parity impurity in a nuclear gamma transition. *PRL*, 14(9):312–315, Mar 1965. doi: 10.1103/PhysRevLett.14.312. URL `http://prola.aps.org/abstract/PRL/v14/i9/p312_1`. 5

J. Byrne. *Neutrons, Nuclei, and Matter*. Institute of Physics Publishing, 1994. 8, 10, 32

J Cavaignac, B Vignon, and R Wilson. Search for parity violation in neutron-proton capture. *Physics Letters B*, 67(2):148–150, Mar 1977. doi: 10.1016/0370-2693(77)90088-0. URL `http://dx.doi.org/10.1016/0370-2693(77)90088-0`. 6, 33, 35

F E Close. Parity violation in atoms? *Nature*, 264(5586):505–506, Dec 1976. doi: 10.1038/264505a0. URL `http://www.nature.com/doifinder/10.1038/264505a0`. 6

Eugene D. Commins and Philip H. Bucksbaum. *Weak interactions of leptons and quarks*. Cambridge University Press, 1983. 5, 6

K Coulter et al. Neutron polarization with a polarized 3he spin filter. *Nuclear Instruments and Methods in Physics Research Section A: Accelerators, Spectrometers, Detectors and Associated Equipment*, 288(2-3):463–466, Mar 1990. doi: 10.1016/0168-9002(90)90139-W. URL `http://dx.doi.org/10.1016/0168-9002(90)90139-W`. 21

R Cox, C McIlwraith, and B Kurrelmeyer. Apparent evidence of polarization in a beam of -rays. *Proceedings of the National Academy of Sciences of the United States of America*, 14(7):544–549, Jul 1928. URL `http://www.jstor.org/stable/85439`. 32, 33

Attila Csótó, B. F Gibson, and G L Payne. Parity conserving asymmetry in n- pradiative capture. *Physical Review C*, 56(2):631–634, Aug 1997. doi: 10.1103/PhysRevC.56.631. URL `http://prola.aps.org/abstract/PRC/v56/i2/p631_1`. 33

Mikayel Dabaghyan. *Measurement of parity violation in thermal neutron capture on a proton*. PhD thesis, University of New Hampshire, 2007. 34, 35, 39

G Danilov. Circular polarization of quanta in absorption of neutrons by protons and isotopic structure of weak interactions. *Physics Letters*, 18(1):40–41, Aug 1965. doi: 10.1016/0031-9163(65)90024-7. URL `http://sciencedirect.com`. 8

B. Desplanques. Parity violation in nuclear systems. *European Physical Journal A*, 24, s2:171–174, 2005. doi: 10.1140/epjad/s2005-04-043-9. 1, 13

Bertrand Desplanques, John Donoghue, and Barry Holstein. Unified treatment of the parity violating nuclear force. *Annals of Physics*, 124(2):449–495, 1980. URL http://www.sciencedirect.com/science/article/B6WB1-4DDR2MH-C7/1/a4de877ebd2d13c5e4cc50666ad40bc4. 7, 77

Albert-José Dianoux and Gerry Lander, editors. *Neutron Data Booklet*. Old City Publishing, second edition, 2003. URL http://www.ill.fr/pages/menu_g/publications.html. 17, 23, 40, 77

E Earle, A McDonald, E Adelberger, K Snover, H Swanson, R von Lintig, H Mak, and C Barnes. Parity mixing in 21ne; evidence for weak neutral currents in nuclei. *Nuclear Physics A*, 396 IS -:221–229, Mar 1983. URL http://www.sciencedirect.com/science/article/B6TVB-471YNB0-R4/1/255a3d5f998778de71d96c97189f4d68. 11

K Elsener, W Grüebler, V König, P. A Schmelzbach, J Ulbricht, D Singy, Ch Forstner, W. Z Zhang, and B Vuaridel. Constraints on weak meson-nucleon coupling from parity nonconservation in 19f. *PRL*, 52(17):1476–1479, Apr 1984. doi: 10.1103/PhysRevLett.52.1476. URL http://prola.aps.org/abstract/PRL/v52/i17/p1476_1. 11

K Elsener, W Grüebler, V König, P Schmelzbach, J Ulbricht, B Vuaridel, D Singy, C Forstner, and W Zhang. Parity nonconservation in 19f nuclei. *Nuclear Physics A*, 461(3-4):579–602, Jan 1987. URL http://www.sciencedirect.com/science/article/B6TVB-4731M7T-MH/1/7dac6f720668d7b2c4863bcfbfcf9eb2. 11

Adalbert Farkas. *Orthohydrogen, Parahydrogen, and Heavy Hydrogen*. The University Press, Cambridge, 1935. 24

Allan Franklin. *Are there really neutrinos?* Perseus Books, 2001. 33

Jerome I Friedman and V. L Telegdi. Nuclear emulsion evidence for parity nonconservation in the decay chain +-+-e+. *Physical Review*, 105(5):1681–1682, Mar 1957. doi: 10.1103/PhysRev.105.1681.2. URL http://prola.aps.org/abstract/PR/v105/i5/p1681_2. 4

M Gari and J Schlitter. Neutral currents in thermal np capture. *Physics Letters B*, 59(2):118–120, Oct 1975. doi: 10.1016/0370-2693(75)90680-2. URL http://dx.doi.org/10.1016/0370-2693(75)90680-2. 8, 10

Richard L Garwin, Leon M Lederman, and Marcel Weinrich. Observations of the failure of conservation of parity and charge conjugation in meson decays: the magnetic moment of the free muon. *Physical Review*, 105(4):1415–1417, Feb 1957. doi: 10.1103/PhysRev.105.1415. URL http://prola.aps.org/abstract/PR/v105/i4/p1415_1. 4

M. Gericke et al. Parity violation in neutron-proton capture: the NPDGamma experiment. to be published, 2009. 35

M. T Gericke, J. D Bowman, and M. B Johnson. Mott-schwinger scattering of polarized low energy neutrons up to thermal energies. *Phys. Rev. C*, 78(4), Oct 2008. doi: 10.1103/PhysRevC.78.044003. URL http://link.aps.org/doi/10.1103/PhysRevC.78.044003. 33

M. T. Gericke et al. Commissioning of the NPDGamma detector array: Counting statistics in current mode operation and parity violation in the capture of cold neutrons on B_4C and ^{27}Al. *Journal of Research of the National Institute of Standards and Technology*, 110:215–219, 2005. 3, 30, 39

M. T. Gericke et al. Upper bounds on parity violating gamma-ray asymmetries in compound nuclei from polarized cold neutron capture. *Physical Review C*, 74:65503, 2006. 39

Michael Gericke. *The NPDGamma experiment: the weak interaction between nucleons and parity violation in cold neutron capture*. PhD thesis, Indiana University, November 2004. URL `http://sns.phys.utk.edu/svn/npdg/trunk/papers/thesis/mgericke/`. 10, 34, 35, 36, 39

Robert Golub, David J. Richardson, and Steve K. Lamoreaux. *Ultra-Cold Neutrons*. Adam Hilger, 1991. 16

L Grodzins. The history of double scattering of electrons and evidence for the polarization of beta rays. *Proceedings of the National Academy of Sciences of the United States of America*, 45(3):399–405, Mar 1959. URL `http://www.jstor.org/stable/89980`. 33

W. Haeberli and Barry R. Holstein. Parity violation and the nucleon-nucleon system. In W. C. Haxton and E. M. Henley, editors, *Symmetries in Nuclear Physics*. World Scientific, 1995. URL `http://arxiv.org/abs/nucl-th/9510062`. 11

F Hasert et al. Search for elastic muon-neutrino electron scattering. *Physics Letters B*, 46 (1):121–124, Sep 1973a. doi: 10.1016/0370-2693(73)90494-2. URL `http://dx.doi.org/10.1016/0370-2693(73)90494-2`. 5

F Hasert et al. Observation of neutrino-like interactions without muon or electron in the gargamelle neutrino experiment. *Physics Letters B*, 46(1):138–140, Sep 1973b. doi: 10.1016/0370-2693(73)90499-1. URL `http://dx.doi.org/10.1016/0370-2693(73)90499-1`. 5

F J Hasert et al. Observation of neutrino-like interactions without muon or electron in the gargamelle neutrino experiment. *Nuclear Physics B*, 73(1):1–22, 1974. URL `http://dx.doi.org/10.1016/0550-3213(74)90038-8`. 5

W. C Haxton. Atomic parity violation and the nuclear anapole moment. *Science*, 275(5307): 1753–0, Mar 1997. doi: 10.1126/science.275.5307.1753. URL `http://www.sciencemag.org/cgi/content/summary/275/5307/1753`. 12

W. C Haxton, C.-P Liu, and M J Ramsey-Musolf. Anapole moment and other constraints on the strangeness conserving hadronic weak interaction. *PRL*, 86(23):5247–5250, Jun 2001. doi: 10.1103/PhysRevLett.86.5247. URL `http://prola.aps.org/abstract/PRL/v86/i23/p5247_1`. 12

B. R Holstein. Overview of hadronic parity violation. *Eur. Phys. J. A*, 32(4):505–511, Jun 2007. doi: 10.1140/epja/i2006-10430-0. URL `http://www.springerlink.com/index/448726413M50733R.pdf`. 13

Barry Holstein. Hadronic parity violation: an overview. *Nuclear Physics A*, 737 IS -:85–92, Jun 2004. URL `http://www.sciencedirect.com/science/article/B6TVB-4CWRXF1-G/1/a5621759fc750d2ee306c9fae2107873`. need Elsevier references from #4,15. 13

Glenn F. Knoll. *Radiation Detection and Measurement*. Wiley, 3rd edition, 2000. ISBN 0471073385. 30

V Knyazkov, E Kolomenskii, V Lobashov, V Nazarenko, A Pirozhkov, A Shablii, E Shulgina, Y Sobolev, and A Yegorov. A new experimental study of the circular polarization of np capture -rays. *Nuclear Physics A*, 417(2):209–230, Apr 1984. doi: 10.1016/0375-9474(84)90505-0. URL `http://dx.doi.org/10.1016/0375-9474(84)90505-0`. 6

L Landau. On the conservation laws for weak interactions. *Nuclear Physics*, 3(1):127–131, Mar 1957. doi: 10.1016/0029-5582(57)90061-5. URL `http://dx.doi.org/10.1016/0029-5582(57)90061-5`. 5

Bernhard Lauss. First measurement of the guide coil field and the magnetic environment in the new npdgamma cave at lansce. Technical Report 20, NPDGamma, 2004. URL `http://sns.phys.utk.edu/npdg/technotes/bfield_measurements.pdf`. 20

T. D Lee and C N Yang. Question of parity conservation in weak interactions. *Physical Review*, 104(1):254–258, Oct 1956. doi: 10.1103/PhysRev.104.254. URL `http://link.aps.org/abstract/PR/v104/p254`. 4

C.-P Liu. Parity-violating observables of two-nucleon systems in effective field theory. *Phys. Rev. C*, 75(6), Jun 2007. doi: 10.1103/PhysRevC.75.065501. URL `http://link.aps.org/doi/10.1103/PhysRevC.75.065501`. 13

V Lobashov, V A Nazarenko, L F Saenko, L M Smotritsky, and G I Kharkevitch. Parity non-conservation in the gamma decay of 181ta. *Physics Letters B*, 25(2):104–106, Aug 1967. doi: 10.1016/0370-2693(67)90191-8. URL `http://dx.doi.org/10.1016/0370-2693(67)90191-8`. 5, 10

V Lobashov et al. Parity non-conservation in radiative thermal neutron capture by protons. *Nuclear Physics A*, 197(1):241–258, Dec 1972. doi: 10.1016/0375-9474(72)90759-2. URL `http://dx.doi.org/10.1016/0375-9474(72)90759-2`. 6

F. Mezei. Novel polarized neutron devices: supermirror and spin component amplifier. *Communications on Physics*, 1976. 17

F. Curtis Michel. Parity nonconservation in nuclei. *Physical Review*, 133(2B):B329–B349, Jan 1964. doi: 10.1103/PhysRev.133.B329. URL `http://prola.aps.org/abstract/PR/v133/i2B/pB329_1`. 5, 8

G Mitchell, C Blessinger, J Bowman, T Chupp, K Coulter, M Gericke, G Jones, M Leuschner, H Nann, S Page, S Penttilä, T Smith, W Snow, and W Wilburn. A measurement of parity-violating gamma-ray asymmetries in polarized cold neutron capture on 35cl, 113cd, and 139la. *Nuclear Instruments and Methods in Physics Research Section A: Accelerators, Spectrometers, Detectors and Associated Equipment*, 521(2-3):468–479, Apr 2004. URL `http://www.sciencedirect.com/science/article/B6TJM-4B7199W-1B/1/92b21e71fddcbee75019b8eecc0aa7a0`. 5

N Mott. The scattering of fast electrons by atomic nuclei. *Proceedings of the Royal Society of London. Series AContaining Papers of a Mathematical and Physical Character*, 124 (794):425–442, Jun 1929. URL `http://www.jstor.org/stable/95377`. 32

N Mott. The polarisation of electrons by double scattering. *Proceedings of the Royal Society of London. Series AContaining Papers of a Mathematical and Physical Character*, 135 (827):429–458, Mar 1932. URL `http://www.jstor.org/stable/95868`. 32

Jeffrey S. Nico and W. Michael Snow. Fundamental neutron physics. *Annual Review of Nuclear and Particle Science*, 55:27–69, 2005. 1

S. A Page, H. C Evans, G. T Ewan, S. P Kwan, J. R Leslie, J. D Macarthur, W Mclatchie, P Skensved, S. S Wang, H. B Mak, C. A Barnes, T. K Alexander, and E. T. H Clifford. Weak pion-nucleon coupling strength: New constraint from parity mixing in 18f. *Physical Review C*, 35(3):1119–1131, Mar 1987. doi: 10.1103/PhysRevC.35.1119. URL `http://prola.aps.org/abstract/PRC/v35/i3/p1119_1`. 11

William H. Press, Brian P. Flannery, Saul A. Teukolsky, and William T. Vetterling. *Numerical Recipes in C: the art of scientific computing*. Cambridge University Press, second edition, 1992. URL `http://nr.com`. 43

E. M Purcell and N. F Ramsey. On the possibility of electric dipole moments for elementary particles and nuclei. *Physical Review*, 78(6):807–807, Jun 1950. doi: 10.1103/PhysRev.78.807. URL `http://link.aps.org/abstract/PR/v78/p807`. 4

Karin M. Rabe. Solid-state physicsresponse with a twist. *Nature*, 449(7163):674, Oct 2007. doi: doi:10.1038/449674a. URL `http://www.nature.com/nature/journal/v449/n7163/full/449674a.html`. 11

Michael J Ramsey-Musolf and Shelley A Page. Hadronic parity violation: a new view through the looking glass. *Annual Review of Nuclear and Particle Science*, 56:1–52, 2006. URL `http://arjournals.annualreviews.org/doi/pdf/10.1146/annurev.nucl.54.070103.181255`. 13

Alfred G Redfield. Nuclear spin-lattice relaxation time in copper and aluminum. *Physical Review*, 101(1):67–68, Jan 1956. doi: 10.1103/PhysRev.101.67. URL `http://prola.aps.org/abstract/PR/v101/i1/p67_1`. 34

A Salam and J Ward. Electromagnetic and weak interactions. *Physics Letters*, 13(2):168–171, Nov 1964. doi: 10.1016/0031-9163(64)90711-5. URL `http://dx.doi.org/10.1016/0031-9163(64)90711-5`. 6

Julian Schwinger. Polarization of neutrons by resonance scattering in helium. *Physcial Review*, 69:681, Feb 1946. 32

Julian Schwinger. On the polarization of fast neutrons. *Physical Review*, 73(4):407–409, Feb 1948. doi: 10.1103/PhysRev.73.407. URL `http://link.aps.org/doi/10.1103/PhysRev.73.407`. 32

P.-N Seo, J D Bowman, M Gericke, R C Gillis, G L Greene, M B Leuschner, J Long, R Mahurin, G S Mitchell, S I Pentilla, G Peralta, E I Sharapov, and W S Wilburn. New pulsed cold neutron beam line for fundamental nuclear physics at LANSCE. *Journal of Research of the National Institute of Standards and Technology*, 110(3):145–148, 2005. URL `http://nvl.nist.gov/pub/nistpubs/jres/110/3/j110-3seo.pdf`. 18

M Sharma, E Babcock, K. H Andersen, L Barron-Palos, M Becker, S Boag, W. C Chen, T. E Chupp, A Danagoulian, T. R Gentile, A Klein, S Penttila, A Petoukhov, T Soldner, E. R Tardiff, T. G Walker, and W. S Wilburn. Neutron beam effects on spin exchange polarized he-3. *Phys. Rev. Lett.*, 101:083002, Feb 2008. doi: 10.1103/PhysRevLett.101.083002. URL `http://arxiv.org/abs/0802.3169v1`. 21, 53

K. A Snover, R von Lintig, E. G Adelberger, H. E Swanson, T. A Trainor, and C. A Barnes. Upper limit on parity mixing in 21ne. *PRL*, 41(3):145–148, Jul 1978. doi: 10.1103/PhysRevLett.41.145. URL `http://prola.aps.org/abstract/PRL/v41/i3/p145_1`. 11

W. M. Snow et al. Measurement of the parity violating asymmetry A_γ in $\vec{\mathrm{n}} + \mathrm{p} \rightarrow \mathrm{d} + \gamma$. *Nuclear Instruments and Methods A*, 440:729–735, 2000. doi: doi:10.1016/S0168-9002(99)01071-2. 3

Neil Tanner. Parity in nuclear reactions. *Physical Review*, 107:1203, 1957. URL `http://prola.aps.org/pdf/PR/v107/i4/p1203_1`. 4, 5

Jagdish Tuli et al. Evaluated nuclear structure data file. URL `http://www.nndc.bnl.gov/ensdf/`. 20, 40, 77

Jagdish K. Tuli. *Nuclear Wallet Cards*. National Nuclear Data Center, seventh edition, April 2005. 40, 77

V. F. Turchin. Scattering of slow neutrons on layered media. *Physics of Atomic Nuclei*, 60 (12):1946–1958, 1997. 17

P. A Vetter, D. M Meekhof, P. K Majumder, S. K Lamoreaux, and E. N Fortson. Precise test of electroweak theory from a new measurement of parity nonconservation in atomic thallium. *PRL*, 74(14):2658–2661, Apr 1995. doi: 10.1103/PhysRevLett.74.2658. URL `http://prola.aps.org/abstract/PRL/v74/i14/p2658_1`. 12

E Warming. Parity non-conservation in the capture of polarized thermal neutrons. *Physics Letters B*, 29(9):564–566, Aug 1969. doi: 10.1016/0370-2693(69)90297-4. URL `http://dx.doi.org/10.1016/0370-2693(69)90297-4`. 5

Steven Weinberg. A model of leptons. *PRL*, 19(21):1264–1266, Nov 1967. doi: 10.1103/PhysRevLett.19.1264. URL `http://prola.aps.org/abstract/PRL/v19/i21/p1264_1`. 5

W. S. Wilburn. Analysis of the arithmetic and geometric mean methods of calculating asymmetries. Message to `npdg@lanl.gov`, April 6 2007. 41

D. H Wilkinson. Parity conservation in strong interactions: Introduction and the reaction he4(d,)li6. *Physical Review*, 109(5):1603–1609, Mar 1958a. doi: 10.1103/PhysRev.109.1603. URL `http://prola.aps.org/abstract/PR/v109/i5/p1603_1`. 5

D. H Wilkinson. Parity conservation in strong interactions: Reactions b11(p, p)b11*2.14and f19(p,)o16*7.12. *Physical Review*, 109(5):1610–1613, Mar 1958b. doi: 10.1103/PhysRev.109.1610. URL `http://prola.aps.org/abstract/PR/v109/i5/p1610_1`. 5

D. H Wilkinson. Parity conservation in strong interactions: Reaction li7(p, p)li7*0.477. *Physical Review*, 109(5):1614–1619, Mar 1958c. doi: 10.1103/PhysRev.109.1614. URL `http://prola.aps.org/abstract/PR/v109/i5/p1614_1`. 5

C Wood, S Bennett, D Cho, B Masterson, J Roberts, C Tanner, and C Wieman. Measurement of parity nonconservation and an anapole moment in cesium. *Science*, 275(5307):1759, Mar 1997. doi: 10.1126/science.275.5307.1759. URL `http://www.sciencemag.org/cgi/content/full/275/5307/1759`. 1, 11

C. S Wu, E Ambler, R W Hayward, D D Hoppes, and R P Hudson. Experimental test of parity conservation in beta decay. *Physical Review*, 105(4):1413–1415, Feb 1957. doi: 10.1103/PhysRev.105.1413. URL `http://link.aps.org/abstract/PR/v105/p1413`. 4

W.-M. Yao et al. Review of particle physics. *Journal of Physics G*, 33:1, 2006. URL `http://pdg.lbl.gov`. 1, 6, 77

V. W Yuan, C. D Bowman, J. D Bowman, J. E Bush, P. P. J Delheij, C. M Frankle, C. R Gould, D. G Haase, J. N Knudson, G. E Mitchell, S Penttilä, H Postma, N. R Roberson, S. J Seestrom, J. J Szymanski, and X Zhu. Parity nonconservation in polarized-neutron transmission through 139la. *Physical Review C*, 44(5):2187–2194, Nov 1991. doi: 10.1103/PhysRevC.44.2187. URL `http://prola.aps.org/abstract/PRC/v44/i5/p2187_1`. 1

Shi-Lin Zhu, C M Maekawa, B R Holstein, M J Ramsey-Musolf, and U van Kolck. Nuclear parity violation in effective field theory. *Nuclear Physics A*, 748:435–498, 2005. URL `http://www.npl.uiuc.edu/exp/mucapture/MuCap_Related/mu+p/pions/pv.pdf`. 13

Rob Mahurin grew up in Beckley, West Virginia, and moved to Franklin, Tennessee in 1995. He earned a bachelor's degree in physics, with minors in astronomy and mathematics, from the University of Tennessee in 2001. He is a very serious person and never, ever, does anything silly.